Effects of Surface Roughness on Electrical Contact, RF Heating and Field Enhancement

by

Peng Zhang

A dissertation submitted in partial fulfillment
of the requirements for the degree of
Doctor of Philosophy
(Nuclear Engineering and Radiological Sciences)
in The University of Michigan
2012

Doctoral Committee:

Professor Yue Ying Lau, Chair
Professor Ronald M. Gilgenbach
Professor Mark J. Kushner
Professor Brian E. Gilchrist
Associate Professor John E. Foster

Acknowledgment

First of all, I must thank my advisor, Professor Y. Y. Lau. During the four years of my graduate study in Ann Arbor, Professor Lau never fails to provide his encouragement, guidance, and support, whenever I needed help. With his mentorship, I learned a great deal, not only in academic skills, but also in life.

I would also like to thank Professor Ronald Gilgenbach, for his encouragement and support on the course of my research and study. I am especially grateful to Professor Gilgenbach for allowing me working in his lab on interesting experiments. I would like to thank Professor Mark Kushner for his support of the fellowship from the Michigan Institute for Plasma Science and Engineering, and for serving on my thesis committee and sparing his valuable time to discuss technical details with me. I wish to thank Professor John Foster for being an excellent instructor on NERS471, which was the first plasma course I have ever taken. I would also wish to thank Professor Foster and Professor Brian Gilchrist for setting aside their valuable time to serve on my thesis committee. I also wish to thank Dr. Roland Timsit. From his excellent papers, and in person, I learnt a lot about electric contacts.

I wish to thank the senior graduate students, Dr. Brad Hoff, Dr. Wilkin Tang, Dr.

David French, Dr. Matt Gomez, and Dr. Jacob Zier, who had provided many insights and advices to my work. I would like to thank my fellow students, Matt Franzi for working together on the window breakdown experiment, and for his patience on explaining to me how equipment works; Ian Rittersdorf and David Simon for working together on solving bizarre equations. I also enjoyed happy hours with them, and with other students: Sonal Patel, Adam Steiner, Geoff Greening, and Matt Weis. I also would like to thank Ian Rittersdorf and Matt Franzi, and other plasma students: Aimee Hubble, Ben Yee, Eric Gillman, Paul Cummings, for preparing the qualifying exam together.

I would especially like to thank my wife, Jiaojiao. With her endless love and support, I greatly enjoyed my graduate school life for the past four years. I also wish to thank my other family members who have been supporting me throughout my life, especially my parents, my uncle and aunt.

This work was supported by Air Force Office of Scientific Research Grant on Cathode and Breakdown MURI04 Grant No FA9550-04-1-0369, by AFOSR Grant on the Basic Physics of Distributed Plasma Discharges, by AFOSR Award FA9550-09-1-0662, L-3 Communications Electron Device Division, and Northrop Grumman Corporation. The Michigan Institute for Plasma Science and Engineering Fellowship, and the University of Michigan Rackham Predoctoral Fellowship are also acknowledged.

Table of Contents

Acknowledgment ..... **ii**

List of Figures ..... **vii**

List of Appendices ..... **xiv**

Abstract…… ..... **xv**

CHAPTER 1 INTRODUCTION **1**

1.1 Motivation and Background 1

1.2 Prior Works 6

1.2.1 Bulk Contact Resistance *6*

1.2.2 Thin Film Contact *9*

1.2.3 RF Heating and Field Enhancement due to Surface Roughness *11*

1.3 Organization of this thesis 14

CHAPTER 2 BULK CONTACT RESISTANCE **16**

2.1 Introduction 16

2.2 Interface Resistance with Dissimilar Materials 21

2.2.1 Cylindrical semi-infinite channel *21*

2.2.2 Cartesian semi-infinite channel *25*

2.3 Total Resistance of Composite Channel 28

2.4 Concluding Remarks 34

CHAPTER 3 THIN FILM CONTACT RESISTANCE **37**

3.1 Introduction 37

3.2 Cartesian Thin Film Contact with Dissimilar Materials 42

3.3 Cylindrical Thin Film Contact with Dissimilar Materials 53

3.4 Thin film spreading resistance as $h \rightarrow 0$ [30] 64

3.4.1 Cartesian thin film a-spot 66

3.4.2 Cylindrical thin film a-spot 69

3.5 Generalizations 74

3.5.1 Extension to a-spot of arbitrary shape [30] 74

3.5.2 Extension to AC case 76

3.5.3 Transfer Lengths and Comparison with Experiment Method 78

3.6 Concluding remarks 81

CHAPTER 4 SURFACE ROUGHNESS INDUCED ENHANCED RF ABSORPTION AND FIELD ENHANCEMENTS 83

4.1 Introduction 83

4.2 The model 86

4.3 RF power absorption 90

4.4 RF field enhancements 99

4.4.1 RF Electric Field Enhancement 99

4.4.2 RF magnetic field enhancement 103

4.5 Concluding remarks 108

CHAPTER 5 CONCLUSION AND SUGGESTED FUTURE WORK 111

5.1 On Bulk Contact Resistance 111

5.2 On Thin Film Contact Resistance 113

5.3 On RF Heating and Field Enhancement 115

Appendix A The contact resistance of a constricted cylindrical channel 118

Appendix B The contact resistance of a constricted Cartesian channel 122

Appendix C The contact resistance of Cartesian thin film 126

Appendix D Conformal mapping for Cartesian thin film contact with uniform resistivity…..……..……..131

Appendix E The contact resistance of thin film to rod geometry 135

References…..... ……139

List of Figures

Fig. 1.1. Typical surface finish tolerances in manufacturing [1] 2

Fig. 1.2 True points of contact occur only at the asperities of the contacting surface, leading to high contact resistance. 3

Fig. 1.3 Holm's *a*-spot model of a circular constriction between two contacting members.. 6

Fig. 1.4 (a) Rosenfeld and Timsit's extension [15] of Holm's *a*-spot to an electrically-conducting cylinder of finite radius *b*, and (b) the normalized contact resistance as a function of *b*/*a*. 8

Fig. 1.5 (a) A rectangular current channel with connecting bridge of a finite axial length in the direction of current flow, a cylindrical current channel with a connecting bridge in the form of a (b) cylinder, and (c) funnel, in the direction of current flow. [23].....8

Fig. 1.6 (a) The current flow lines between two bulk marterials meeting at a contact spot as assumed in traditional contact theory. (b) The current flow lines between two thin films meeting at a contact spot. [21].....10

Fig. 1.7 (a) Schematic comparison of the region of spreading resistance in a solid conductor with the corresponding region in a thin film conductor. (b) Normalized thin film spreading resistance as a function of the ratio of constriction radius to thin film thickness *a*/*h*. [20] 10

Fig. 1.8 Comparison of different models on increase in surface resistivity due to surface roughness: Morgan 1949[81], Groiss et al. 1996 [84] and HFSS [85], and Microwave Engineers Handbook [86]. 13

Fig. 2.1 A schematic of a single asperity, joining two current channels of different materials. 17

Fig. 2.2 Holm's model of a straight cylinder current channel of radius b (>>a) joint by a zero thickness circular hole of radius a (a-spot). 18

Fig. 2.3 Two current channels, II and III, are made in contact through the bridge region, I, in either Cartesian or cylindrical geometries. Holm's a-spot corresponds to the cylindrical geometry with $h = 0$, $a << b$, $a << c$. Current flows from left to right. 18

Fig. 2.4 Semi-infinite current channel with dissimilar materials, Region I and II, in either Cartesian or cylindrical geometries. Current flows from left to right. 19

Fig. 2.5 Comparison of $\bar{R}_c(b/a, \rho_1/\rho_2)$ according to the exact theory (symbols) and to the simple scaling law (Eq. (2.2), solid lines) for semi-infinite cylindrical current channels, I and II. (a) $\bar{R}_c$ as a function of aspect ratio b/a. (b) $\bar{R}_c$ as a function of resistivity ratio ρ_1/ρ_2. The dashed lines in (b) respresent the cylindrical a-spot theory of Timsit ($\bar{R}_{c0}(b/a)\big|_{Timsit}$, Eq. (2.3)). 24

Fig. 2.6 Comparison of $\bar{R}_c(b/a, \rho_1/\rho_2)$ according to the exact theory (symbols) and to the simple scaling law (Eq. (2.5), solid lines) for semi-infinite Cartesian current channels, I and II. (a) $\bar{R}_c$ as a function of aspect ratio b/a. (b) $\bar{R}_c$ as a function of resistivity ratio ρ_1/ρ_2. The dashed lines in (b) respresent the Cartesian a-spot theory ($\bar{R}_{c0}(b/a)\big|_{LTZ}$, Eq. (2.6)).....26

Fig. 2.7 Comparison of the exact theory [Fig. 7 of Ref. 23] and the analytical formula, $\bar{R}_{c0}(x)\big|_{LTZ}$, Eq. (2.6), for the normalized contact resistance of the Cartesian a-spot ($h = 0$). The less accurate formula $\bar{R}_c \cong 4\ln(\frac{2}{\pi}\frac{b}{a})$, [Eq. 2 of Ref. 23] is also plotted. 28

Fig. 2.8 Sample calculations of the total resistance R of a cylindrical channel according to MAXWELL 3D simulation (symbols) and the scaling law (solid lines).....32

Fig. 2.9 Experimental validation of the scaling law for contact resistance, Eq. (2.7), for the special case of uniform resistivity by Gomez *et al*. [24]. (a) Experimental setup. All channels had diameter $2b$=15.9 ±0.1 mm, and length L= 40.8 ±0.2 mm, $2a$ = 4(or 8) ±0.1mm, h varied from 1.5 to 9.1 ±0.2mm. (b) Measured contact resistance in good agreement with theoretical results.....33

Fig. 3.1 Thin film structures in either Cartesian or cylindrical geometries. Terminals *E* and *F* are held at a constant voltage (V_0) relative to terminal *GH*, which is grounded. The z-axis is the axis of rotation for the cylindrical geometry. The resistivity ratio ρ_1/ρ_2 in Regions I and II is arbitrary. 39

Fig. 3.2 Two cases of Cartesian thin film contact represented by Fig. 3.1: (a) thin film sheet resistor, and (b) heatsink geometry.....40

Fig. 3.3 Cylindrical case of thin film contact represented by Fig. 3.1.....40

Fig. 3.4 $\bar{R}_c$ for the Cartesian structure in Fig. 3.1 and Fig. 3.2, is plotted as a function of (a) L_2/a, and (b) L_2/h, for a/h = 0.1 and 8.0, and ρ_1/ρ_2 = 10, 1.0, and 0.1 (top to bottom).....43

Fig. 3.5 $\bar{R}_c$ as a function of a/h, for the Cartesian structure in Fig. 3.1 and Fig. 3.2. The solid line represents the exact calculations [Eq. (C8)], where each curve consists of many combinations of b/a and b/h, with either $L_2 >> a$ *or* $L_2 >> h$. The dashed lines respresent the limiting cases of $\rho_1/\rho_2 \to \infty$ [Eqs. (3.2)] and $\rho_1/\rho_2 \to 0$ [Eq. (3.3)], where asymptotes for a/h >> 1 are, respectively, $\bar{R}_c \simeq (2\pi/3)a/h$, and $\bar{R}_c \simeq 4\ell n2 = 2.77$. 44

Fig. 3.6 $\bar{R}_c$ as a function of a/h, for the special case of ρ_1/ρ_2 = 1 of the Cartesian structure in Fig. 3.1 and Fig. 3.2. The solid line represents the conformal mapping results [Eq. (3.4)], the dashed lines respresent the asymptotes [Eq. (3.5)], and the symbols represents the exact Fourier series representation calculation [cf. Eq. (C8)]. 47

Fig. 3.7 $\bar{R}_c$ for Cartesian thin film structures in Fig. 3.1 and Fig. 3.2, as a function of (a) aspect ratio a/h, and (b) resistivity ratio ρ_1/ρ_2; symbols for the exact theory, solid lines for the scaling law Eq. (3.6). 49

Fig. 3.8 Field lines in the right half of Region II of the Cartesian geometry in Fig. 3.1 for $\rho_1/\rho_2 = 1$ with (a) $a/h = 0.1$, (b) zoom in view of (a) for $0 \leqslant y/a \leqslant 3$, (c) $a/h = 1$, and (d) $a/h = 10$. The results from series expansion method [Eq. (C1)] (solid lines) are compared to those from conformal mapping (dashed lines).....50

Fig. 3.9 Field lines in the right half of Region II of the Cartesian geometry in Fig. 3.1 for $a/h = 1$ with (a) $\rho_1/\rho_2 = 0.1$, (b) $\rho_1/\rho_2 = 1$, and (c) $\rho_1/\rho_2 = 10$. For $\rho_1/\rho_2 = 1$, the results from series expansion method [Eq. (C1)] (solid lines) are compared to those from conformal mapping (dashed lines).....51

Fig. 3.10 $\bar{R}_c$ for the cylindrical structure in Fig. 3.1 and Fig. 3.3, is plotted as a function of (a) L_2/a, and (b) L_2/h, for $a/h = 0.1$ and 10.0, and $\rho_1/\rho_2 = 10$, 1.0, and 0.1 (top to bottom).....55

Fig. 3.11 $\bar{R}_c$ in semi-log plot (a) and linear plot (b) as a function of a/h, for the cylindrical structure in Fig. 3.1 and Fig. 3.3. The solid lines represent the exact calculations [Eq. (E8)], where each curve consists of many combinations of b/a and b/h, with either $L_2 >> a$ *or* $L_2 >> h$. The dashed lines respresent the limiting cases of $\rho_1/\rho_2 \to \infty$ [Eq. (3.10)] and $\rho_1/\rho_2 \to 0$ [Eq. (3.11), which is valid only for $a/h < 0.5$ [20]]. For a/h >> 1, $\bar{R}_c \simeq (1/2\pi)\, a/h$ as $\rho_1/\rho_2 \to \infty$, and $\bar{R}_c \simeq (4\ell n2)/\pi^2 = 0.28$ as $\rho_1/\rho_2 \to 0$ 56

Fig. 3.12 $\bar{R}_c$ as a function of a/h, for the cylindrical structure in Fig. 3.1 with $\rho_1 = \rho_2 = \rho$. The theoretical result (line) [Eq. (3.12)] is compared to MAXWELL 3D simulation (symbols). In the simulation, we set $\rho = 0.001\Omega$m, $L_1 = 10$mm, a ranging from 0.01 to 4mm with fixed $b = 10h = 5$mm, and h ranging from 0.1 to 20mm with fixed $b = 10a = 10$mm, and a terminal voltage $V_0 = 10$V was applied. 59

Fig. 3.13 $\bar{R}_c$ for cylindrical thin film structures in Fig. 3.1 and Fig. 3.3, as a function of (a) aspect ratio a/h, and (b) resistivity ratio ρ_1/ρ_2; symbols for the exact theory, solid lines for the scaling law Eq. (3.13). 61

Fig. 3.14 Field lines in the right half of Region II of the cylindrical geometry in Fig. 3.1 for $\rho_1/\rho_2 = 1$ with (a) $a/h = 0.1$, (b) zoom in view of (a) for $0 \leqslant r/a \leqslant 3$, (c) $a/h = 1$, and (d) $a/h = 10$. 63

Fig. 3.15 Field lines in the right half of Region II of the cylindrical geometry in Fig. 3.1 for $a/h = 1$ with (a) $\rho_1/\rho_2 = 0.1$, (b) $\rho_1/\rho_2 = 1$, and (c) $\rho_1/\rho_2 = 10$.....64

Fig. 3.16 Cylindrical (or Cartesian) electrical contact between two thin films of the same material. The z-axis is the axis of rotation for the cylindrical geometry. 65

Fig. 3.17 Cylindrical or Cartesian geometries for (a) electrode applied directly on thin film, and (b) region of zero resistivity in contact with thin film. The z-axis is the axis of rotation for the cylindrical geometry. For both (a) and (b), the boundary conditions, the potential profile, and therefore the spreading resistance in the thin film are equivalent to that in Fig. 3.16.....66

Fig. 3.18 The normalized thin film spreading resistance as a function of a/h, for the Cartesian structure in Fig. 3.16 and Fig. 3.17. The solid line is for the conformal maping calculations [Eq. (3.17)]. The dashed line, which overlaps with the solid line, is for the series expansion caluclations [cf., Eq. (C8) of Appendix C]. The symbols are for the MAXWELL 2D simulation. Two sets of simulation were performed. The first set (circles) was fixed at a = 2cm, and varying h from 2cm to 0.1cm; the second set (crosses) was fixed at h = 0.1cm, and varying a from 3cm to 7cm.....67

Fig. 3.19 The field lines in the right half of the Cartesian thin film in Fig. 3.16 and Fig. 3.17, calculated for the case of $a/h = 10.1$ and $\rho_1 = 0.01\rho$ [cf. Fig. 3.17(b)]. The crowding of the field lines near the constriction corner could lead to significant local ohmic heating there. 68

Fig. 3.20 The normalized thin film spreading resistance as a function of a/h, for the cylindrical structure in Fig. 3.16 and Fig. 3.17. The solid line is for Eq. (3.20), synthesized from the results of series expansion calculations [cf., Eq. (E8)], the dashed line for Tismit's calculations [cf., Eq. (18) of Ref. 20], the symbols for

the MAXWELL 2D simulation. Three sets of simulation were performed. The first set was fixed at a = 2cm (circles), and varying h from 2cm to 0.1cm; the second set was fixed at h = 0.1cm (crosses), and varying a from 3cm to 7cm; the third set was fixed at a = 0.01cm (diamonds), and varying h from 0.025cm to 0.00015cm.....71

Fig. 3.21 The field lines in the right half of the cylindrical thin film in Fig. 3.16 and Fig. 3.17, calculated for the case of a/h = 10.1 and $\rho_1 = 0.01\rho$ [cf. Fig. 3.17(b)] 72

Fig. 3.22 *a*-spot of an arbitrary shape. Note the current flow lines in the bottom figure are identical to Fig. 3.21 and Fig. 3.19 locally. 75

Fig. 3.23 (a) High-frequency AC current in a bulk solid with constriction of size *a* where the current flow is limited to the skin depth δ [20,99], and (b) The DC thin film contact [30] analyzed in this section (Fig. 3.16). 76

Fig. 3.24 The DC thin film model ($h \rightarrow 0$) studied in this thesis may be considered as the limiting case for the high frequency AC bulk contact resistance [20, 99]....77

Fig. 3.25 Comparison of the DC thin film model studied in this thesis with the AC bulk contact resistance [20]. As $a/\delta \rightarrow \infty$, we expect the curve would converge to a final value of 0.28, as predicted by our DC thin film model (Fig. 3.20). 78

Fig. 3.26 A transfer length method test structure and a plot of total resistance as a function of contact spacing, *d*. [Fig. 3.22 of Ref. 91].....80

Fig. 4.1 A small hemispherical bump on a conducting surface whose local RF electric field is E_0 and local RF magnetic field H_0 in the absence of the bump. 84

Fig. 4.2 Decomposition of the local electromagnetic field (E_0, H_0) into (a) the TE mode (E_0, 0), and (b) the TM mode (0, H_0). 87

Fig. 4.3 Transformation of the "protrusion on surface" problem into a spherical eigenmode problem for (a) the TE_{110} mode and (b) the TM_{110} mode. The mode index (110) refers to variations in r, θ, and φ. Note that, by symmetry, the mode patterns in (a) or (b) are unchanged with or without a perfect conductor inserted in the horizontal mid-plane. 88

Fig. 4.4 The asymptotes for (a) α_E and (b) α_H as a function of δ/a for $\mu_1/\mu_2 = 1$, $\varepsilon_{1r}/\varepsilon_2 = 1$ and various values of λ/a. These asymptotes yield approximate maximum values

of $\alpha_E = 3$ and $\alpha_H = 1.0$. Note that the scaling law for α_H is independent of λ/a. 95

Fig. 4.5 The electric field enhancement factor on the hemispherical protrusion at the apex (β_{EA}, solid curve) and at the base (β_{EC}, dotted curve) as a function of δ/a, setting $\mu_1/\mu_2 = 1$, $\varepsilon_{1r}/\varepsilon_2 = 1$, and $\lambda/a = 100$ 101

Fig. 4.6 Maxwell 3D results of (a) electric field distribution around the hemispherical bump, (b) magnitude of electric field along a horizontal line 0.5 cm (=bump radius) above the flat surface (dashed line), which agrees extremely well with the analytical calculation (solid line). E_0 is the electric field far away from the bump. 102

Fig. 4.7 The magnetic field enhancement factor on the hemispherical protrusion at the apex point A (β_{MA}, solid curve) and at the base point C (β_{MC}, dotted curve) as a function of δ/a, setting $\mu_1/\mu_2 = 1$, $\varepsilon_{1r}/\varepsilon_2 = 1$ and $\lambda/a = 100$. 104

Fig. 4.8 Maxwell 3D results. (a) Magnetic field distribution around the hemispherical bump in the plane parallel and perpendicular to the applied field. Plot of the magnitude of magnetic field (dashed lines) along Line 1 (b), and along Line 2 (c), both are horizontal lines 1.0 cm (=one bump radius) above the flat surface. Also shown are the analytical calculations (solid lines). H_0 is the magnetic field far away from the bump. 107

List of Appendices

Appendix A The contact resistance of a constricted cylindrical channel 118

Appendix B The contact resistance of a constricted Cartesian channel 122

Appendix C The contact resistance of Cartesian thin film 126

Appendix D Conformal mapping for Cartesian thin film contact with uniform resistivity…..……..…..……131

Appendix E The contact resistance of thin film to rod geometry 135

Abstract

Surfaces are never perfectly flat. Because of the surface roughness on a microscopic scale, true contact between two conductors occurs only at the asperities (small protrusions) of the contacting surfaces, leading to contact resistance, an important issue to high power microwave sources, pulsed power systems, tribology, thin film devices, integrated circuits, and interconnects, etc. Another profound effect of surface roughness is the excessive local field enhancement that triggers RF breakdown, and the rapid loss of superconductivity in a superconducting cavity. This thesis models various effects of surface roughness, including electrical contact resistance for both bulk and thin film contacts. Scaling laws are constructed for a large range of resistivity ratios and aspect ratios. Also presented is roughness-induced enhanced RF heating, and the enhanced RF electric and magnetic fields.

Presented first is the bulk contact resistance with dissimilar materials. For decades, the basic model for contact resistance remains that of Holm's *a*-spot, where current flows through a circular constriction of small radius *a* and zero thickness at the bulk interface. We vastly extend Holm's theory to higher dimensions, including dissimilar materials. Both Cartesian and cylindrical channels are analyzed. A scaling law for the contact

resistance has been constructed for arbitrary aspect ratios and resistivity ratios. This scaling law has been validated in various tests, simulations, and experiments.

This thesis next presents the thin film contact resistance with dissimilar materials. Simple, analytical scaling laws have been developed, for both cylindrical and Cartesian geometries. We have identified the optimal condition for minimization of the thin film contact resistance. The current crowding effect, which may induce excessive ohmic heating, is also studied. Extension to general *a*-spot geometry is made. This work may offer useful insights for the design and fabrication of thin film devices and components.

Presented also is roughness-induced enhanced RF heating, and the enhanced RF electric and magnetic fields. We analytically compute the power absorption due to a hemispherical protrusion with arbitrary permittivity ε, permeability μ and conductivity σ, on a flat surface. The local electric and magnetic field enhancements on the protrusion are calculated analytically. Scaling laws are derived.

CHAPTER 1

INTRODUCTION

Surfaces are never perfectly flat. On a presumably pristine surface, roughness arises from the manufacturing process intrinsically, even if only at the atomic level. In molding, surface finish of the die determines the surface finish of the workpiece. In machining, the interaction of the cutting edges and the microstructure of the material being cut contribute to the final surface roughness. Different manufacturing processes introduce different degrees of surface roughness [1], as summarized in Fig. 1.1. Other factors, such as impurities attached to the surface (e.g., dirt particles), and grain boundaries, may also contribute to the overall surface roughness. Correct function of the fabricated component often is critically dependent on its degree of roughness.

1.1 Motivation and Background

This thesis theoretically studies the effect of surface roughness. The main focus is on surface roughness induced electrical contact resistance, RF heating, and field enhancement. This study was motivated by the recognition of its importance in the ongoing studies at the University of Michigan's Plasma, Pulsed Power, and Microwave

Laboratory, including Z-pinch [2-4], high power microwave generation [5], triple point junctions [6-8], field emitters [6,9], and heating phenomenology [10,11].

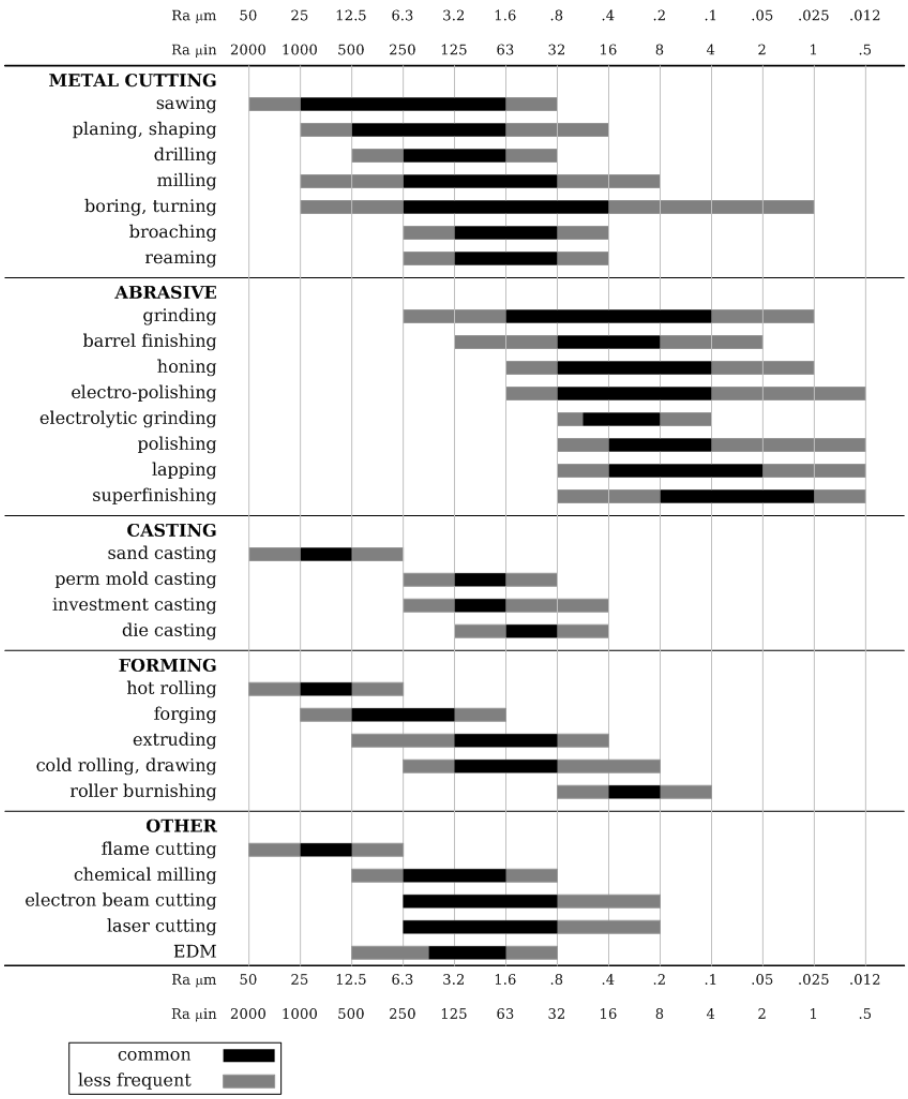

Fig. 1.1. Typical surface finish tolerances in manufacturing [1]

When two materials make contact with one another, the surface roughness causes only a fraction of the area between the materials to actually connect. Current flows only

through the true contact areas. This gives rise to contact resistance [12-30] (Fig. 1.2). In the wire Z-pinch, the electrical contacts at the cathode and the anode of the wires affect the current delivered to the wire load [2, 3, 31-34]. This in turn affects the Z-pinch plasma dynamics and has a significant influence on the X-ray yield for the Z-machine at the Sandia National Laboratories [35]. At University of Michigan, the contact resistance effects in a Z-pinch were mitigated by soft metal gaskets [2].

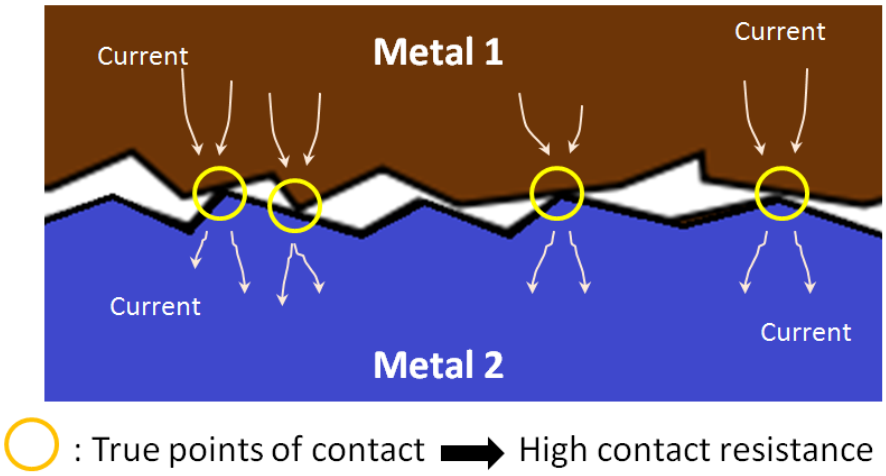

Fig. 1.2 True points of contact occur only at the asperities of the contacting surface, leading to high contact resistance.

Besides Z-pinch, surface roughness induced contact resistance has a significant impact on the electrical characteristics of thin film devices, such as thin film transistors [16, 36, 37]. The theoretical analysis to be developed in this thesis for bulk contacts provides a natural extension to thin film contacts, which have become increasingly important in the performance limit of integrated circuits [38-40]. Recently, dramatic

advances have fueled speculation that carbon nanotubes (CNTs) will be useful for downsizing circuit dimensions; however, their superior ballistic current carrying capability is greatly compromised by the unavoidable large contact resistances [41]. For CNT based cathodes [41-43] and interconnects [44-46], carbon-metal interfaces must be optimized to achieve low contact resistances required by the International Technology Roadmap for Semiconductors [47]. Contact resistance is also critical to micro-electromechanical system relays and microconnector systems, where thin metal films of a few microns are typically used to form electrical contacts [21, 22]. It is important that low contact resistance be achieved so as to reduce Joule heating and thereby achieve more reliable performance under high current, as the heat generated during switching cycles is the most significant factor leading to failure [48-50]. On the largest scales, faulty electrical contact has caused the recent failure of the Large Hadron Collider, and similarly threatens the International Thermonuclear Experimental Reactor [51, 52].

Another profound effect of surface roughness is the enhanced RF power absorption and excessive local field enhancement both in the RF electric field and in the RF magnetic field. These effects severely limit the performance of RF cavities or slow wave structures [53-65], for example, in communication systems [54-56], particle accelerators [57-59, 65-69], material characterization at microwave frequencies [70,71], etc. Surface roughness may cause enhanced power absorption in these devices [62-65, 72, 73]. It may lead to excessive local electric field enhancement that triggers RF breakdown [56, 74-76].

In a superconducting cavity, surface roughness may also cause local magnetic field enhancement that leads to abrupt quenching, [53, 57, 58] i.e., rapid loss of superconductivity. Surface finish is one of the most important current issues of the Niobium (Nb) superconducting radio frequency (SRF) cavities used in particle accelerators [77]. Hence, creating ultra-smooth, polished surfaces to retain superconductivity in the presence of large RF magnetic fields remains the current challenge in superconducting cavity fabrication [53, 66, 67].

In high speed interconnects and microelectronic packaging based on organic materials, the surface of the metal conductors (typically copper) is artificially roughened to enhance the interfacial adhesion between the dielectric and the conductive medium, subject to rigid industry specifications [78, 79]. However, such roughness of the surface can cause significant effects on conductor loss at microwave frequencies due to the skin effect. Experiments [80] demonstrated the decrease of effective conductivity of different copper foils by as much as 50%-70% in the multigigahertz region due to surface roughness. Accurate estimation of power loss due to surface roughness is instrumental for packaging and board substrate technology development, i.e., for making the tradeoff between thermomechanical reliability (adhesion), electrical performance (loss), and cost [78-80]. Surface finish is also known to be an issue for excessive power absorption in the development of gyrotrons, the millimeter wave source widely used in magnetic confinement fusion experiments.

1.2 Prior Works

1.2.1 Bulk Contact Resistance

For decades, the fundamental model of electrical contact has been that of Holm's *a*-spot [12], which is a circular constriction of radius *a* between two contacting surfaces, as shown in Fig. 1.3. Current is allowed to flow only through the constriction spot (*a*-spot) from one conducting member to the other. The resistance due to this constriction is defined as contact resistance, or constriction resistance, R_c, which is found to be [12]

$$R_c = \frac{\rho}{2a}, \tag{1.1}$$

where ρ is electrical resistivity of the contact members and *a* is the contact spot radius.

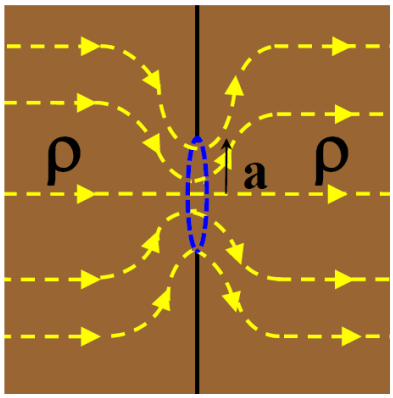

Fig. 1.3 Holm's *a*-spot model of a circular constriction between two contacting members.

Implicit in the theory of Holm [12] are three assumptions:

(A) The *a*-spot has a zero thickness, i.e., zero axial length in the direction of current flow;

(B) The current channel is made of the same material, e. g., the effects of contaminants

have been ignored; and

(C) The contact members are bulk conductors, whose dimensions transverse to the current flow are infinite.

Many subsequent models have been developed based on Holm's *a*-spot theory, adopting these three assumptions. Because of Holm's seminal contributions, IEEE has a dedicated conference on electrical contacts named after Holm, and the *a*-spot is used as the conference logo. Some results of this thesis were presented at the Holm conference [26].

In 1966, Greenwood [14] developed a statistical model to study the contact resistance of a cluster of *a*-spots, aiming to characterize the true contact between nominally flat surfaces, which is known to occur at a number of contact asperities (i.e. a number of clusters of micro-contacts), instead of a single *a*-spot. While Greenwood's model is extensively used, it has adopted the three assumptions of Holm's model listed in the preceeding paragraph. Holm's *a*-spot theory has also been extended to other shapes, including elliptical [12], square [19], and ring shapes [19], etc. Again the three basic assumptions of Holm's *a*-spot are always used.

In the 1980s, Rosenfeld and Timsit [15] considered the contact resistance in a constricted cylinder of uniform material, with finite radius *b* and constriction radius *a*, shown in Fig. 1.4(a), and extended Holm's *a*-spot theory to include the effects of finite bulk radius [15], thereby relaxing assumption (C) stated above. The contact resistance of such an *a*-spot with contact members of finite radius is expressed as

$$R_c = \frac{\rho}{2a} \times \bar{R}_c , \tag{1.2}$$

where the normalized contact resistance $\bar{R}_c$ is plotted in Fig. 1.4(b). Holm's *a*-spot value in Eq. (1.1) is recovered from Eq. (1.2) as $b/a >> 1$.

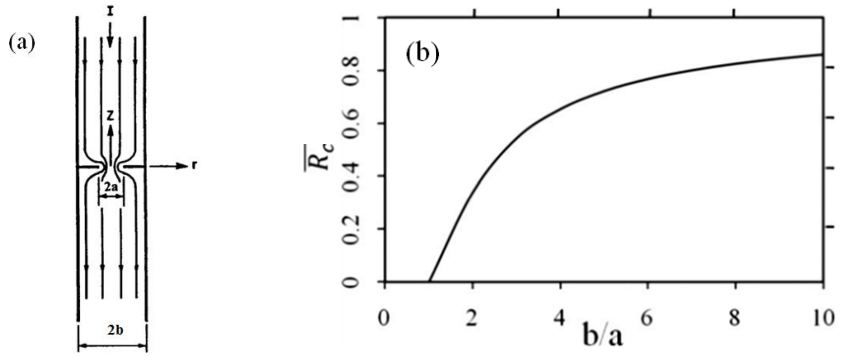

Fig. 1.4 (a) Rosenfeld and Timsit's extension [15] of Holm's *a*-spot to an electrically-conducting cylinder of finite radius *b*, and (b) the normalized contact resistance as a function of *b*/*a*.

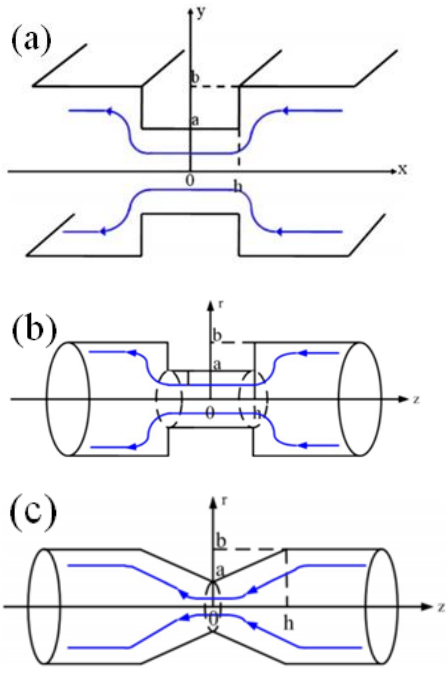

Fig. 1.5 A rectangular current channel with connecting bridge of a finite axial length in the direction of current flow (a), a cylindrical current channel with a connecting bridge in the form of a cylinder (b), and of a funnel (c). [23]

More recently, Lau and Tang [23] extended the Holm-Rosenfeld-Timsit theory to include a connecting bridge of finite axial length (*h*) connecting two metal blocks, as shown in Fig. 1.5, thus relaxing Holm's zero-thickness assumption (i.e. the assumption (A)) and the infinite transverse dimension assumption (i.e. the assumption (C)). Both Cartesian and cylindrical geometries of different connecting bridge types are treated, shown in Fig. 1.5. While the theory in Ref. [23] was validated in recent experiments [24], it is restricted to the special case where the current channels and their connecting bridges are made of the same material, and where the current channels are of equal geometrical dimensions. Thus, the model of Ref. [23] gives no hint on the important effects of contaminants at the electrical contact.

This thesis [25, 26] extends Holm-Rosenfeld-Timsit-Lau-Tang's theory to include the effects of dissimilar materials, thereby simultaneously relaxing assumptions (A), (B), and (C) mentioned in this sub-section.

1.2.2 Thin Film Contact

The bulk contact models discussed in Section 1.2.1 are inapplicable to the thin film contact, where one or more of the contact members are in the form of thin film and not semi-infinite. This is because in a thin film contact, shown in Fig. 1.6, the spreading resistance arises from the sharp bending of current flow lines in the immediate vicinity of the constriction edges, with subsequent spreading into the thin film over a distance of one constriction radius or less [20-22]. Beyond this distance, the current flow lines are

parallel to the film boundaries and any additional contribution of spreading resistance to overall resistance becomes insignificant [20].

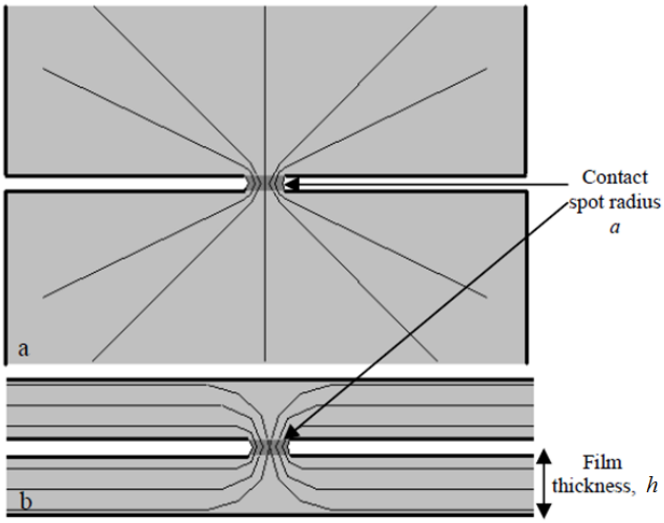

Fig. 1.6 (a) The current flow lines between two bulk marterials meeting at a contact spot as assumed in traditional contact theory. (b) The current flow lines between two thin films meeting at a contact spot. [21]

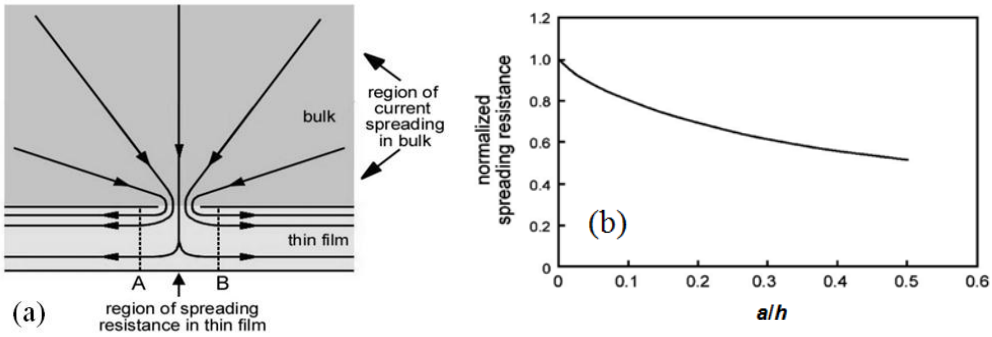

Fig. 1.7 (a) Schematic comparison of the region of spreading resistance in a solid conductor with the corresponding region in a thin film conductor. (b) Normalized thin film spreading resistance as a function of the ratio of constriction radius *a* to thin film thickness *h*. [20]

Hall [16, 17] investigated the two-dimensional (2D) thin film resistance for various patterns in Cartesian geometry, using conformal mapping. Denhoff [27] studied the spreading resistance of a round thin film contact by solving Laplace equation using analytic, numerical, and finite element methods. The spreading resistance of three-dimensional (3D) thin film disks is also analyzed by Norberg *et al*. [22], and by Timsit [20]. These prior works assume either a constant and uniform electrical resistivity in all regions, or an equipotential at the constriction interfaces. In particular, Timsit [20] analytically calculated the spreading resistance of a circular thin conducting film of thickness *h* connected to a bulk solid via an *a*-spot constriction of radius *a*, as shown in Fig. 1.7(a), but with the assumption that the current density distribution through the *a*-spot of this film is the same as the known current density distribution through the *a*-spot in a semi-infinite bulk solid [12, 15]. The normalized thin film contact resistance $\bar{R}_c = R_c/(\rho/4a)$ is plotted in Fig. 1.7(b). Timsit's theory is valid only for a/h < 0.5 [20], as shown in Fig. 1.7(b).

This thesis [26, 28-30] provides extensive generalization of Hall's models on 2D Cartesian thin-film contacts, and Timsit's models on 3D cylindrical thin-film contacts, with inclusion of effects of dissimilar materials.

1.2.3 RF Heating and Field Enhancement due to Surface Roughness

An early work to investigate the roughness surface loss can be dated back to 1940's when Morgan [81] first studied the increased resistive power loss for a periodic 2D

ridged structure. Morgan [81] used the finite-difference method to solve a quasi-static eddy-current problem for a 2D periodic rough surface. The results were then fitted as an empirical formula Eq. (1.3), which has since been the guideline model for qualifying surface-roughness-induced power loss in practice [81-83],

$$\alpha_{Morgan} = \frac{P_r}{P_s} = 1 + \frac{2}{\pi}\tan^{-1}\left[1.4\left(\frac{h}{\delta}\right)^2\right]. \tag{1.3}$$

Here, P_r and P_s are the power loss of a rough surface conductor and of its smooth surface counterpart, respectively, h is the RMS (root-mean-square) value of surface roughness, $\delta = \sqrt{2/\sigma\omega\mu}$ is the skin depth, σ is the conductivity, ω is the wave frequency and μ is the free space permeability.

In 1996, Groiss *et al.* [84] described a similar factor α_{Groiss} for correcting conductor loss for the surface roughness and skin depth, using the same symbols as in Eq. (1.3),

$$\alpha_{Groiss} = \frac{P_r}{P_s} = 1 + \exp\left[-\left(\frac{\delta}{2h}\right)^{1.6}\right], \tag{1.4}$$

which was obtained by the finite-element method (FEM). Equation (1.4) is used directly in the commercial FEM software High Frequency Structure Simulator (HFSS) [85], for capturing the conductor loss with surface roughness.

Despite the extensive usage of Eqs. (1.3) and (1.4), they are only empirical fittings to numerical calculations on a restricted model. Thus, their regime of their validity is unclear. Figure 1.8 plots the increase in surface resistivity due to surface roughness obtained from Eqs. (1.3) and (1.4). Also superimposed in Fig. 1.8 is the experimental

curve from the Microwave Engineers Handbook [86]. The discrepancies among the models are apparent.

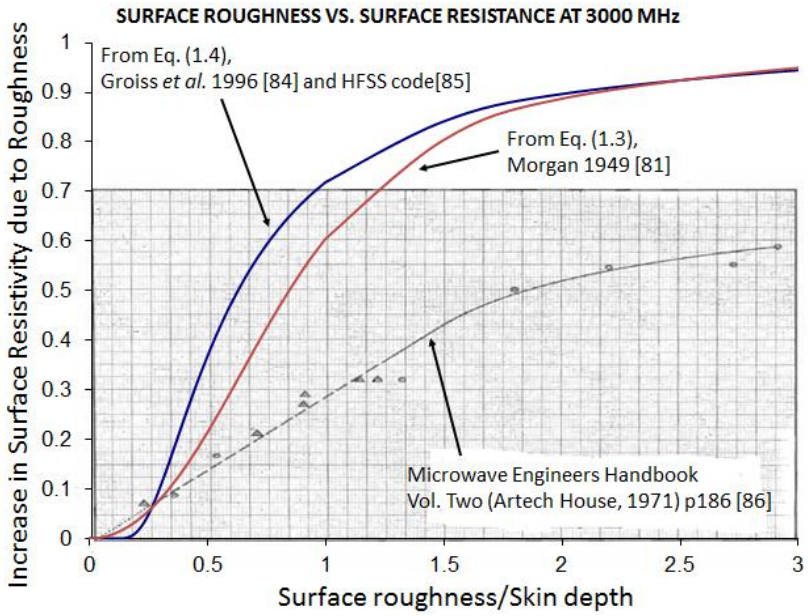

Fig. 1.8 Comparison of different models on increase in surface resistivity due to surface roughness: Morgan 1949[81], Groiss et al. 1996 [84] and HFSS [85], and Microwave Engineers Handbook [86].

Several authors have recently studied periodic [87, 88], as well as random [78] 2D roughness profiles using different methods. Holloway and Kuester [87] calculated the power loss associated with 2D periodic conducting and superconducting rough interfaces using a generalized impedance boundary condition. However, the fine details of the field near the surface are not resolved [87]. Matsushima and Nakata [88] utilized the equivalent source method to numerically study periodic rectangular, triangular, and semielliptical grooves both transverse and parallel to current flow. In Gu *et al*., [78], the effects of random 2D surface roughness are analyzed by using two methods: the analytic

small perturbation method and the numerical method of moments. There are also studies on modeling the surface roughness with randomly distributed bosses on surface [89, 90]. However, there is still lack of accurate model to evaluate both power absorption and electric and magnetic field enhancements due to surface roughness, where the roughness assumes arbitrary values of permittivity ε, permeability μ, and electrical conductivity σ.

This thesis [11] derives simple scalings on the power loss and electric and magnetic field enhancements on a surface roughness that is represented by a hemispherical protrusion. The hemispherical protrusion may assume arbitrary values of ε, μ, and σ.

1.3 Organization of this thesis

Chapter 2 presents the model for contact resistance of bulk contacts with dissimilar materials. In this chapter, Holm's classical a-spot theory [12] is vastly extended to higher dimensions, including dissimilar materials in the main current channels and in the connecting bridge joining them. Both Cartesian and cylindrical channels have been analyzed. A scaling law for the contact resistance has been constructed for arbitrary values of the dimensions of the channels and bridges, and for arbitrary electrical resistivity in each section. We shall present validation of the scaling laws in various tests and simulations, and experiments.

Chapter 3 presents the models for thin film contact resistance with dissimilar materials. Simple, analytical scaling laws have been developed, for both cylindrical and

Cartesian geometries. The crowding of field lines (or current flow lines) near the constriction corner is investigated, which could lead to significant ohmic heating there. We also identified the optimal condition under which the thin film contact resistance may be minimized. Extension to arbitrary geometries of *a*-spot and to AC response of the electrical contacts is attempted. The transfer length estimated from the model is also compared with that of the "transmission line model" and the related experimental method that has been extensively used in the characterization of semiconductor devices [91].

Chapter 4 covers roughness-induced enhanced RF heating, and the enhanced RF electric and magnetic fields. We analytically compute the power absorption due to a small hemispherical protrusion on a resonant cavity's surface. The local electric and magnetic field enhancement factors on the protrusion are also calculated analytically. This protrusion may represent a foreign object since its permittivity ε, permeability μ and conductivity σ may take on arbitrary values. Scaling laws are derived.

The conclusion and suggestions for future work are given in Chapter 5. The major results are stated in the main text. The derivations are given in the Appendices.

CHAPTER 2

BULK CONTACT RESISTANCE

2.1 Introduction

Because of the surface roughness on a microscopic scale, true contact between two pieces of conductors occurs only at the asperities (small protrusions) of two contacting surfaces. Current flows only through these asperities, which occupy a small fraction of the area of the nominal contacting surfaces. This gives rise to contact resistance [12, 13, 15, 23]. Shown in Fig. 2.1 is a schematic drawing of a single asperity. It is clear that contact resistance is highly random, depending on the surface roughness, on the applied pressure, on the hardness of the materials, and perhaps most importantly, on the residing oxides and contaminants at the contact [12, 13, 40]. We shall model the single asperity (Fig. 2.1) by the idealized model in Fig. 2.3 below.

For decades, the fundamental model of electrical contact has been that of Holm's *a*-spot [12], which consists of two semi-infinite cylinders of radius *b* placed together. Current can flow through them only via a "bridge" in the form of a circular disk of radius $a << b$, as shown in Fig. 2.2. While there are statistical treatments [14, 18] and extensions

of the *a*-spot theory to other disk shapes [15], Holm's zero-thickness assumption ($h = 0$) is almost always used [12]. Most recently, an attempt has been made to relax Holm's zero-thickness assumption to include a connecting bridge of finite axial length (h) connecting two metal blocks [3, 23]. While the theory in Ref. [23] was validated in recent experiments [24], it is restricted to the special case where the current channels and their connecting bridges are made of the *same* material, and where the current channels are of equal geometrical dimensions (Fig. 1.5). Thus, the model of Ref. [23] gives no hint on the important effects of contaminants at the electrical contact (Fig. 2.1).

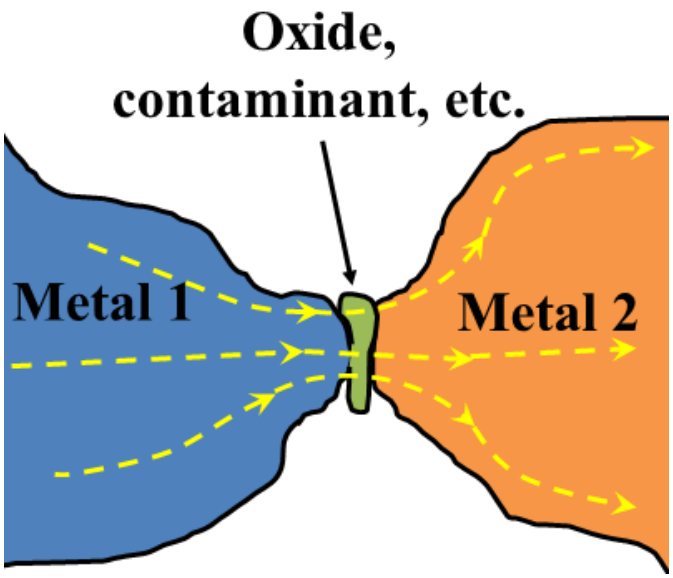

Fig. 2.1 A schematic of a single asperity, joining two current channels of different materials.

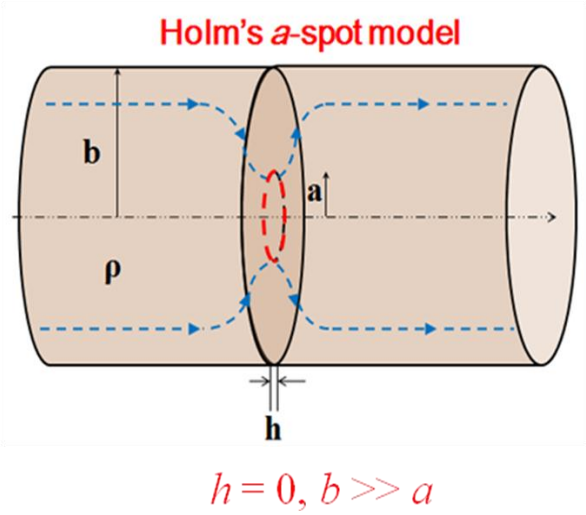

Fig. 2.2 Holm's model of a straight cylinder current channel of radius *b* (>>*a*) joint by a zero thickness circular hole of radius *a* (a-spot).

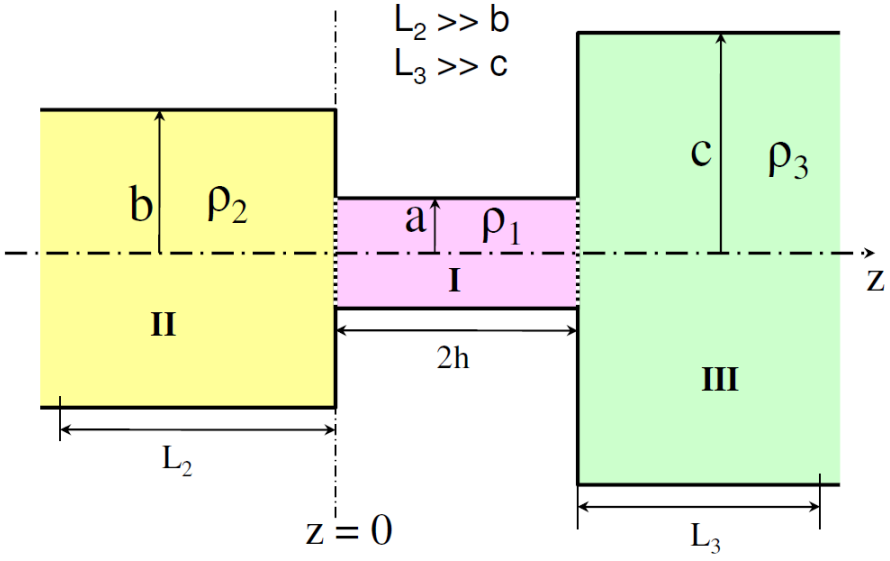

Fig. 2.3 Two current channels, II and III, are made in contact through the bridge region, I, in either Cartesian or cylindrical geometries. Holm's *a*-spot corresponds to the cylindrical geometry with *h* = 0, *a* << *b*, *a* << *c*. Current flows from left to right.

In this chapter, we substantially generalize Holm's classical *a*-spot theory to higher dimensions, including vastly different materials at the joints [25, 26]. In so doing,

we also greatly extend Ref. [23] by allowing the contact region to have an arbitrary electrical resistivity, as would be expected if there were oxides or contaminants in the contact region (Fig. 2.1). Figure 2.3 shows the geometry of such a generalized *a*-spot, Region I, which has a finite axial length 2*h*, joining two conducting current channels (II, III). This figure shows a Cartesian (cylindrical) current channel with half channel width (radius) of *a*, *b* and *c* ($a \le b$, $a \le c$), and electrical resistivity ρ_1, ρ_2 and ρ_3. It is assumed that the axial extents of channels II and III are so long that the current flow in these channels is uniform far from the contact region, I. In this chapter, we construct the scaling laws for the total electrical resistance in Regions II, I, and III, including the interfaces of these regions for arbitrary values of *a*, *b*, *c*, *h*, ρ_1, ρ_2 and ρ_3 [cf. Eqs. (2.7) and (2.8)].

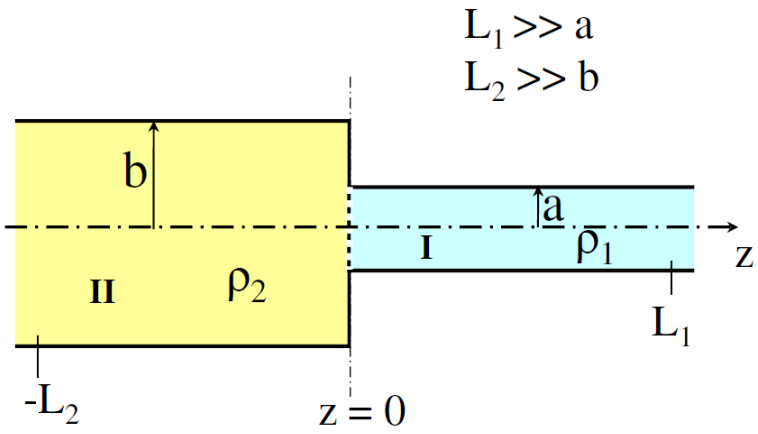

Fig. 2.4 Semi-infinite current channel with dissimilar materials, Region I and II, in either Cartesian or cylindrical geometries. Current flows from left to right.

We shall first consider the special case $h >> a$ for the contact region, I, so that the

electrostatic fringe field at one interface (at $z = 0$) has an exponentially small influence on the other interface (at $z = 2h$), and vice versa. The contact resistance at the interface between Regions II and I, for instance, is then the same as if Regions II and I were semi-infinite in the axial (z) direction (Fig. 2.4). The current flow in the semi-infinite geometry shown in Fig. 2.4 may be formulated exactly for both Cartesian and cylindrical channels. From this exact formulation, we obtain the interface resistance between Regions I and II for arbitrary values of a, b, ρ_1, and ρ_2. The vast amount of data thus collected allows us to synthesize a simple scaling law for the interface resistance. This groundwork for the interface resistance then led to our proposed scaling laws for the total electrical resistance in Regions II, I, and III, for the geometry shown in Fig. 2.3, for general values of a, b, c, h, ρ_1, ρ_2 and ρ_3. We should remark that we have not provided an exact formulation for the general geometry shown in Fig. 2.3. The validity of the scaling laws for Fig. 2.4 is then established by our demonstration that these scaling laws are indeed an excellent approximation in several known limiting cases. They are also spot-checked against the numerical code, MAXWELL 3D [85]. From these scaling laws, we conclude that, in general, the bulk resistance in the generalized a-spot region I (Fig. 2.3) dominates over the resistance at the interfaces between Regions I and II, and between Regions I and III. The small intrinsic error in the scaling laws is also assessed.

Only the major results will be presented in the main text. Their derivations are given in Appendices A and B.

2.2 Interface Resistance with Dissimilar Materials

The interface resistance between Regions I and II of Fig. 2.3, say, may be accurately evaluated when the axial extent of each region is much greater than the respective transverse dimension. It may be formulated exactly when the axial extent is semi-infinite (Fig. 2.4). This section presents the results of this exact formulation, together with a comparison with the proposed scaling laws, for both cylindrical and Cartesian geometry. In Fig. 2.4, we designate $z = 0$ as the axial location of the interface, the axial length of Region I is L_1 (>> a) and the axial length of Region II is L_2 (>> b). Other parameters are defined in Fig. 2.4.

2.2.1 Cylindrical semi-infinite channel

For the semi-infinite cylindrical current channel (Fig. 2.4), we solve the Laplace's equation for Region I and Region II, and match the boundary conditions at the interface, $z = 0$. The details of the calculations are given in Appendix A. The total resistance R from $z = -L_2$ to $z = L_1$ is found to be,

$$R = \underbrace{\frac{\rho_2 L_2}{\pi b^2}}_{\text{Bulk}} + \underbrace{\frac{\rho_2}{4a}\overline{R}_c\left(\frac{b}{a}, \frac{\rho_1}{\rho_2}\right)}_{\text{Interface}} + \underbrace{\frac{\rho_1 L_1}{\pi a^2}}_{\text{Bulk}}. \tag{2.1}$$

In Eq. (2.1), the first and third term represents the bulk resistance in Regions II and I, respectively. The second term represents the interface resistance between Regions I and II, R_c, which is also the contact resistance for Fig. 2.4 (if Regions I and II are regarded as

two current channels). If we express this interface resistance as $R_c = (\rho_2 / 4a)\overline{R}_c$ for the cylindrical channel, we find that $\overline{R}_c$ depends only on the aspect ratio *b*/*a* and the resistivity ratio ρ_1/ρ_2, as explicitly displayed in Eq. (2.1). The *exact* expression for $\overline{R}_c$ is derived in Appendix A [cf. Eq. (A7)]. In Eq. (A7), the coefficient B_n is solved numerically in terms of ρ_1/ρ_2 and *b*/*a*, from the infinite matrix method [cf. Eq. (A4)]. The infinite matrix Eq. (A4), is solved directly by MATLAB, with increasing number of terms included until convergence is realized. As an independent check, we solve Eq. (A4) by the explicit iterative method for $\rho_1/\rho_2 > 1$ [cf. Eq. (A10)]. The two methods yield identical numerical values of B_n. These numerical values of B_n then give $\overline{R}_c$ from Eq. (A7).

The exact theory of $\overline{R}_c$ [cf. Eq. (A7)] is plotted as a function of *b*/*a* and ρ_1/ρ_2 in Fig. 2.5. It is clear from Fig. 2.5(a) that $\overline{R}_c$ increases as *b*/*a* increases, for a given ρ_1/ρ_2. It is a bit surprising, however, that for a very broad range of ρ_1/ρ_2 from 10^{-2} to 10^2, $\overline{R}_c$ varies only by a difference of $\Delta \cong 0.08076$ for a given aspect ratio *b*/*a*, as is evident in Fig. 2.5(b). In the limit $b/a \to \infty$, this maximum variation is proven to be $\Delta = 32/3\pi^2 - 1 = 0.08076$ [cf. Eq. (A14)].

Based on the exact theory and its data over the huge parameter space shown in Fig. 2.5, we propose a simple *analytical* scaling law of $\overline{R}_c$, the normalized interface resistance, for the cylindrical semi-infinite current channel with dissimilar materials (Fig. 2.4),

$$\overline{R}_c\left(\frac{b}{a}, \frac{\rho_1}{\rho_2}\right) \cong \overline{R}_{c0}\left(\frac{b}{a}\right)\Big|_{Timsit} + \frac{\Delta}{2} \times \left(\frac{2\rho_1}{\rho_1 + \rho_2}\right) \times g\left(\frac{b}{a}\right), \textbf{ (Cylindrical)} \qquad (2.2)$$

$$\overline{R}_{c0}\left(b/a\right)\Big|_{Timsit} = 1 - 1.41581(a/b) + 0.06322(a/b)^2 + 0.15261(a/b)^3 + 0.19998(a/b)^4,$$
$$g(b/a) = 1 - 0.3243(a/b)^2 - 0.6124(a/b)^4 - 1.3594(a/b)^6 + 1.2961(a/b)^8$$

(2.3)

where $\Delta = 32/3\pi^2 - 1 = 0.08076$, and $\overline{R}_{c0}\left(x\right)\Big|_{Timsit}$ is the normalized contact resistance of the *a*-spot derived by Rosenfeld and Timsit [15] for the special case: $h = 0$, $b = c$, and $\rho_2 = \rho_3$. Both $g(x)$ and $\overline{R}_{c0}\left(x\right)\Big|_{Timsit}$ are monotonically increasing functions of $x = b/a$ with $g(1) = 0$, $g(\infty) = 1$, $\overline{R}_{c0}\left(1\right)\Big|_{Timsit} = 0$, $\overline{R}_{c0}\left(\infty\right)\Big|_{Timsit} = 1$, and therefore Eq. (2.2) yields $\overline{R}_c\left(1, \rho_1/\rho_2\right) = 0$, as expected of the interface resistance from Fig. 2.4 in the limit $b/a = 1$. The scaling law of contact resistance, Eq. (2.2), is shown by the solid curves in Fig. 2.5, which compare extremely well with the exact theory, Eq. (A7), shown by the symbols, essentially for the entire range of $0 < \rho_1/\rho_2 < \infty$ and $b/a \geq 1$ for the cylindrical channel (Fig. 2.4).

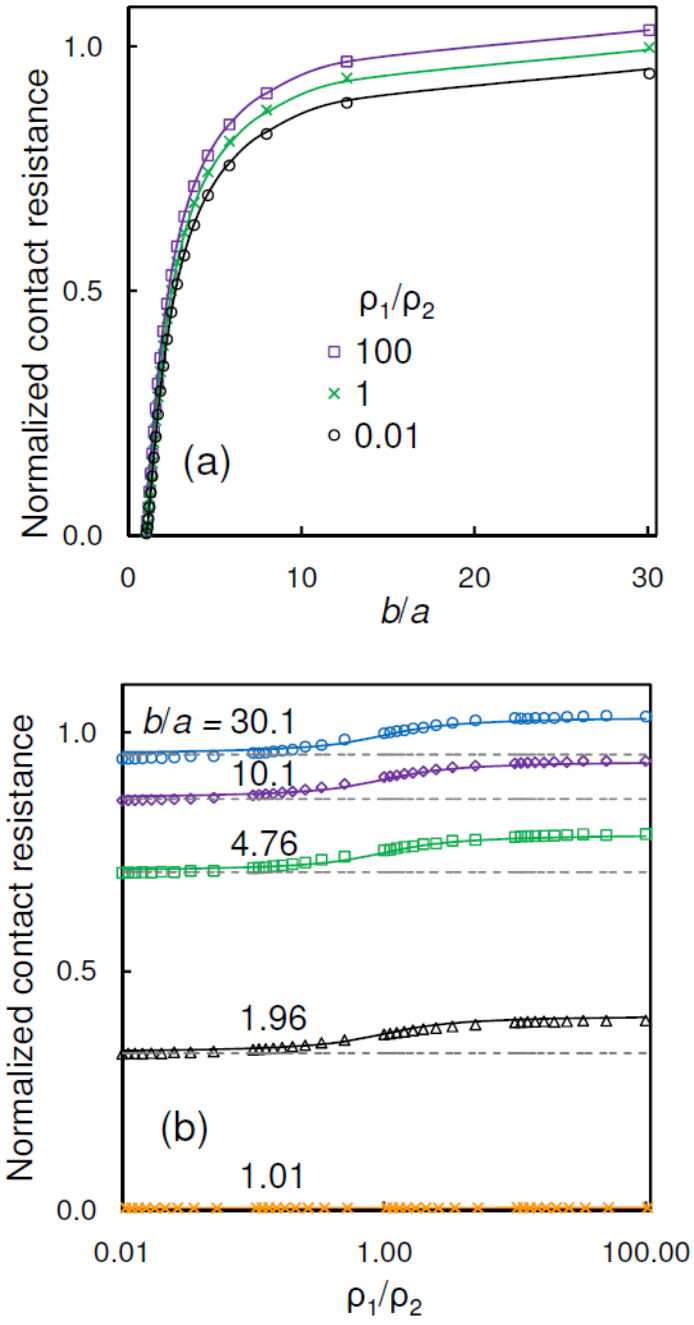

Fig. 2.5 Comparison of $\bar{R}_c(b/a, \rho_1/\rho_2)$ according to the exact theory (symbols) and to the simple scaling law (Eq. (2.2), solid lines) for semi-infinite cylindrical current channels, I and II. (a) $\bar{R}_c$ as a function of aspect ratio *b*/*a*. (b) $\bar{R}_c$ as a function of resistivity ratio ρ_1/ρ_2. The dashed lines in (b) respresent the cylindrical *a*-spot theory of Timsit ($\bar{R}_{c0}(b/a)\big|_{Timsit}$, Eq. (2.3)).

2.2.2 Cartesian semi-infinite channel

Similarly, for the semi-infinite Cartesian current channel (Fig. 2.4), we solve the Laplace's equation for Region I and Region II, and match the boundary conditions at the interface, $z = 0$. The details of the calculations are given in Appendix B. The total resistance R from $z = -L_2$ to $z = L_1$ is found to be,

$$R = \underbrace{\frac{\rho_2 L_2}{2b \times W}}_{\text{Bulk}} + \underbrace{\frac{\rho_2}{4\pi W}\overline{R}_c\left(\frac{b}{a}, \frac{\rho_1}{\rho_2}\right)}_{\text{Interface}} + \underbrace{\frac{\rho_1 L_1}{2a \times W}}_{\text{Bulk}}, \tag{2.4}$$

where W denotes the channel width in the third, ignorable dimension that is perpendicular to the paper, and the rest of the symbols have been defined in Fig. 2.4. In Eq. (2.4), the first and third term represents the bulk resistance in Regions II and I, respectively. The second term represents the interface resistance between Regions I and II, R_c, which is also the contact resistance for Fig. 2.4 (if Regions I and II are regarded as two current channels). If we express this interface resistance as $R_c = (\rho_2 / 4\pi W)\overline{R}_c$ for the Cartesian channel, we find that $\overline{R}_c$ depends only on the aspect ratio b/a and the resistivity ratio ρ_1/ρ_2 (similar to the cylindrical case) as explicitly displayed in Eq. (2.4). The *exact* expression for $\overline{R}_c$ is derived in Appendix B [cf. Eq. (B7)]. In Eq. (B7), the coefficient B_n is solved numerically in terms of ρ_1/ρ_2 and b/a, from the infinite matrix method [cf. Eq. (B4)], and, as an independent check, from the explicit iterative method for $\rho_1/\rho_2 > 1$ [cf. Eq. (B10)]. The two methods yield identical numerical values of B_n. These numerical values of B_n then give $\overline{R}_c$ from Eq. (B7).

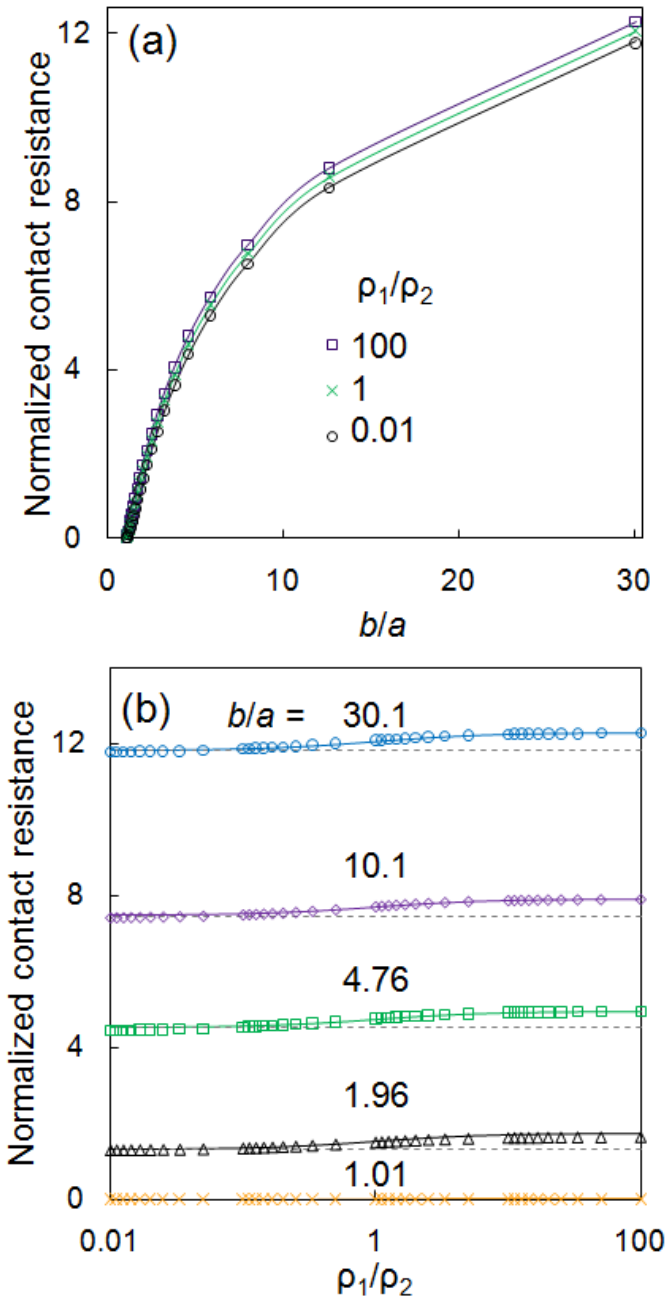

Fig. 2.6 Comparison of $\bar{R}_c(b/a, \rho_1/\rho_2)$ according to the exact theory (symbols) and to the simple scaling law (Eq. (2.5), solid lines) for semi-infinite Cartesian current channels, I and II. (a) $\bar{R}_c$ as a function of aspect ratio *b*/*a*. (b) $\bar{R}_c$ as a function of resistivity ratio ρ_1/ρ_2. The dashed lines in (b) respresent the Cartesian *a*-spot theory ($\bar{R}_{c0}(b/a)\big|_{LTZ}$, Eq. (2.6)).

The exact theory of $\overline{R}_c$ [cf. Eq. (B7)] is plotted as a function of *b/a* and ρ_1/ρ_2, as shown in Fig. 2.6. It is clear from Fig. 2.6(a) that $\overline{R}_c$ increases as *b*/*a* increases, for a given ρ_1/ρ_2. In fact, $\overline{R}_c$ diverges logarithmically as *b/a* >> 1, as shown in Eq. (2.6) and Fig. 2.7 below. Again, similar to the cylindrical case, it is found that for a very broad range of ρ_1/ρ_2 from 10^{-2} to 10^2, $\overline{R}_c$ varies at the most by a difference of 0.4548 for a given aspect ratio *b*/*a* of the Cartesian channel, as is evident in Fig. 2.6(b). The constant 0.4548 is derived in the limit $b/a \to \infty$ in Appendix B.

Based on the exact theory and its data over the huge parameter space shown in Fig. 2.6, we propose a simple *analytical* scaling law of $\overline{R}_c$, the normalized interface resistance, for the Cartesian semi-infinite current channel with dissimilar materials (Fig. 2.4),

$$\overline{R}_c\left(\frac{b}{a},\frac{\rho_1}{\rho_2}\right) \cong \overline{R}_{c0}\left(\frac{b}{a}\right)\Big|_{LTZ} + 0.2274\times\left(\frac{2\rho_1}{\rho_1+\rho_2}\right)\times g\left(\frac{b}{a}\right), \textbf{ (Cartesian)} \qquad (2.5)$$

$$\begin{aligned}
&\overline{R}_{c0}\left(b/a\right)\Big|_{LTZ} = 4\ln(2b/\pi a) + 4\ln(\pi/2)\times f(b/a),\\
&f(b/a) = 0 - 0.03250(a/b) + 1.06568(a/b)^2 - 0.24829(a/b)^3 + 0.21511(a/b)^4, \qquad (2.6)\\
&g(b/a) = 1 - 1.2281(a/b)^2 + 0.1223(a/b)^4 - 0.2711(a/b)^6 + 0.3769(a/b)^8
\end{aligned}$$

where $\overline{R}_{c0}\left(x\right)\Big|_{LTZ}$ is the normalized contact resistance of the Cartesian "*a*-spot" derived by Lau, Tang, and Zhang [23] for the special case: *h* = 0, *b* = *c*, and $\rho_2 = \rho_3$ [Fig. 2.7]. Note that the analytical formula, Eq. 2.6, is virtually identical to the exact theory of Ref [23], as shown in Fig. 2.7. It is the Timsit analog for the Cartesian channel [cf. Eq. (2.3)].

In Eq. (2.6), $f(1) = 1$, $f(\infty) = 0$, $g(1) = 0$, $g(\infty) = 1$, $\overline{R}_{c0}\left(1\right)\Big|_{LTZ} = 0$, and

$d\left[\bar{R}_{c0}(x)\big|_{LTZ}\right]/dx = 0$ when $x = b/a = 1$. Note further that, from Eq. (2.5), the normalized interface resistance $\bar{R}_c(1, \rho_1/\rho_2) = 0,$ as expected of Fig. 2.4 in the limit $b/a = 1$. The scaling law of contact resistance, Eq. (2.5), is shown by the solid curves in Fig. 2.6, which compare extremely well with the exact theory, Eq. (B7), shown by the symbols, essentially for the entire range of $0 < \rho_1/\rho_2 < \infty$ and $b/a \geq 1$ for the Cartesian channel.

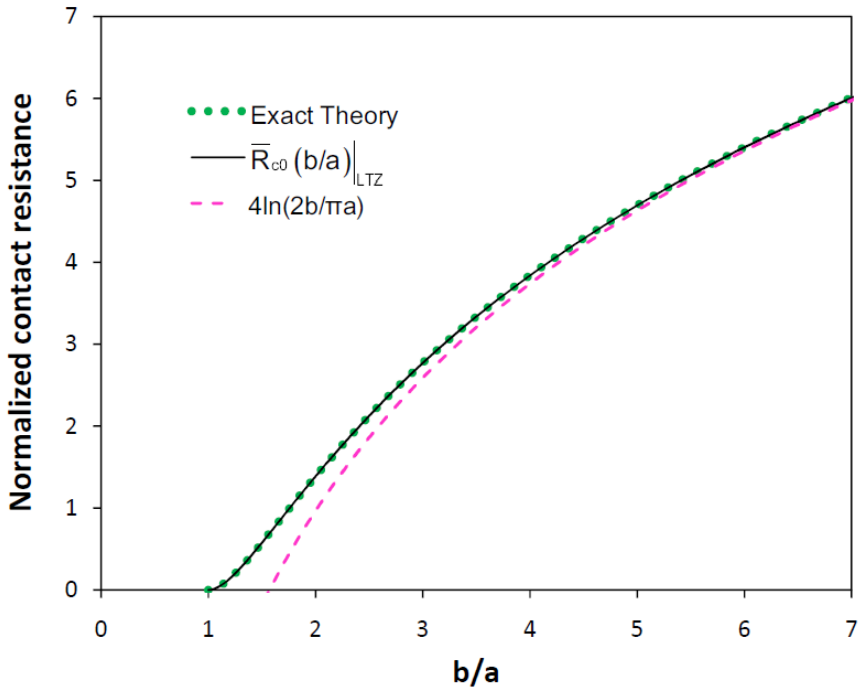

Fig. 2.7 Comparison of the exact theory [Fig. 7 of Ref. 23] and the analytical formula, $\bar{R}_{c0}(x)\big|_{LTZ}$, Eq. (2.6), for the normalized contact resistance of the Cartesian a-spot (*h* = 0).

The less accurate formula $\bar{R}_c \cong 4\ln(\frac{2}{\pi}\frac{b}{a})$, [Eq. 2 of Ref. 23] is also plotted.

2.3 Total Resistance of Composite Channel

The interface resistance established for the semi-infinite channel in Section 2.2

prompted us to postulate a scaling law for the total resistance in a complex channel that is modeled in Fig. 2.3. We decompose the total resistance into bulk resistance and interface resistance. For the time being, we pretend that the scaling laws for the interface resistance given in Section 2.2 are also applicable when the contact region, I, has an arbitrary axial length, 2*h* (Fig. 2.3). We shall then verify that such an assumption introduces an error of at most 10 percent in the contact resistance in the worst case, $h = 0$, by comparing with known results in such a limit. (Recall that the $h = 0$ limit is simply the *a*-spot for the symmetric case $b = c$, and $\rho_2 = \rho_3$).

Thus, in terms of the parameters defined in Fig. 2.3, for the cylindrical channel, we propose that the scaling law for the total electrical resistance in Regions II, I, and III, including the interfaces of these regions is of the form,

$$R = \underbrace{\frac{\rho_2 L_2}{\pi b^2}}_{\text{Bulk}} + \underbrace{\frac{\rho_2}{4a}\overline{R}_c\left(\frac{b}{a},\frac{\rho_1}{\rho_2}\right)}_{\text{Interface}} + \underbrace{\frac{\rho_1 \times 2h}{\pi a^2}}_{\text{Bulk}} + \underbrace{\frac{\rho_3}{4a}\overline{R}_c\left(\frac{c}{a},\frac{\rho_1}{\rho_3}\right)}_{\text{Interface}} + \underbrace{\frac{\rho_3 L_3}{\pi c^2}}_{\text{Bulk}}, \qquad \textbf{(Cylindrical)} \qquad (2.7)$$

where $\overline{R}_c$ is given by Eq. (2.2). Similarly, for the Cartesian channel, the proposed scaling law for the total electrical resistance in Regions II, I, and III, including the interfaces of these regions reads,

$$R = \underbrace{\frac{\rho_2 L_2}{2b \times W}}_{\text{Bulk}} + \underbrace{\frac{\rho_2}{4\pi W}\overline{R}_c\left(\frac{b}{a},\frac{\rho_1}{\rho_2}\right)}_{\text{Interface}} + \underbrace{\frac{\rho_1 \times 2h}{2a \times W}}_{\text{Bulk}} + \underbrace{\frac{\rho_3}{4\pi W}\overline{R}_c\left(\frac{c}{a},\frac{\rho_1}{\rho_3}\right)}_{\text{Interface}} + \underbrace{\frac{\rho_3 L_3}{2c \times W}}_{\text{Bulk}}, \qquad \textbf{(Cartesian)} \qquad (2.8)$$

where $\overline{R}_c$ is given by Eq. (2.5), and *W* denotes the channel width in the third, ignorable dimension that is perpendicular to the paper.

In both Eqs. (2.7) and (2.8), the first, third, and fifth term represent, respectively, the bulk resistance in Regions II, I, and III. The second and fourth term represent the interface resistance, respectively, at the left interface between Regions I and II, and at the right interface between Regions I and III. If one considers Region I as the electrical contact between current channel II and current channel III, then the second, third and fourth terms combine to give the contact resistance between these two current channels.

We shall now compare the scaling laws, Eqs. (2.7) and (2.8), with the results in various limits, with sample calculations using a numerical code, and experimental validation.

Case A. $h >> a$

When the axial length ($2h$) of the contact Region, I (Fig. 2.3), much exceeds its transverse dimension, a, the electrostatic fringe field at one interface has an exponentially small influence on the other interface [cf. Eq. (A1) and Eq. (B1) of the Appendices A and B, respectively]. Thus, the contact resistance at the left interface between Regions II and I, for instance, is then the same as if Regions II and I were semi-infinite in the axial direction (Fig. 2.4), which has been discussed in great detail in Section II above. Similar comments apply to the contact resistance at the right interface between Regions I and III. Equations (2.7) and (2.8) are then clearly valid as the five terms represent the five components of the total resistance (bulk and interface), all in series from left to right in Fig. 2.3.

Case B. $h \rightarrow 0$

In the opposite limit of Case A, the axial length $2h$ in Region I is much smaller than a, with $h = 0$ being the limiting case. In the latter limit, the third term in the RHS of Eqs. (2.7) and (2.8) vanishes identically, and the contact resistance is then given by the sum of the second and fourth terms, which we compare with known results in several special cases. This is the most stringent test because the interface resistance, represented by the second and the fourth terms, is derived under the assumption of $h >> a$, whereas in this subsection, $h = 0$!

For the cylindrical (Cartesian) channel, the $h = 0$ limit becomes the a-spot analyzed by Holm [12], Rosenfeld and Timsit [15], and Lau, Tang, and Zhang [23, 25], for the symmetrical case $\rho_2 = \rho_3$ and $b = c$. The scaling laws for the contact resistance, Eqs. (2.7) and (2.8), indeed become identical to these a-spot theories for $\rho_1/\rho_2 \rightarrow 0$, as shown in Eqs. (2.2) and (2.5), and also in Fig. 2.5 (b) and Fig. 2.6 (b). The reason is that in this symmetrical case ($\rho_2 = \rho_3$, $b = c$, $h \rightarrow 0$), the current flow is perpendicular to the contact area, at the location of the a-spot, by symmetry of the geometry. Thus the entire a-spot is an equipotential surface, the same as if Region I is made of perfectly conducting material ($\rho_1 \rightarrow 0$). In the opposite limit $\rho_1/\rho_2 \rightarrow \infty$, the contact resistance according to the scaling law differs from the a-spot theory by at most 7.4% (8.2%) for a cylindrical (Cartesian) channel from the data presented in Fig. 2.5 and Fig. 2.6.

In yet another limit, $h \rightarrow 0$, $b/a \rightarrow \infty$, $c/a \rightarrow \infty$, but $\rho_2 \neq \rho_3$, our scaling law, Eqs. (2.7) and (2.8) for the cylindrical channel, gives a value of contact resistance that

differs by at most 8% from Holm's established value of $(\rho_2 + \rho_3)/4a$ for this limiting case [12].

Thus, conservatively, we categorically state that our scaling law for the interface resistance commits an error of at most 10% for all values of h, $0 \le h < \infty$, and for all values of ρ_1/ρ_2, $0 \le \rho_1/\rho_2 < \infty$.

Case C. Comparison of 3D Maxwell code to scaling law

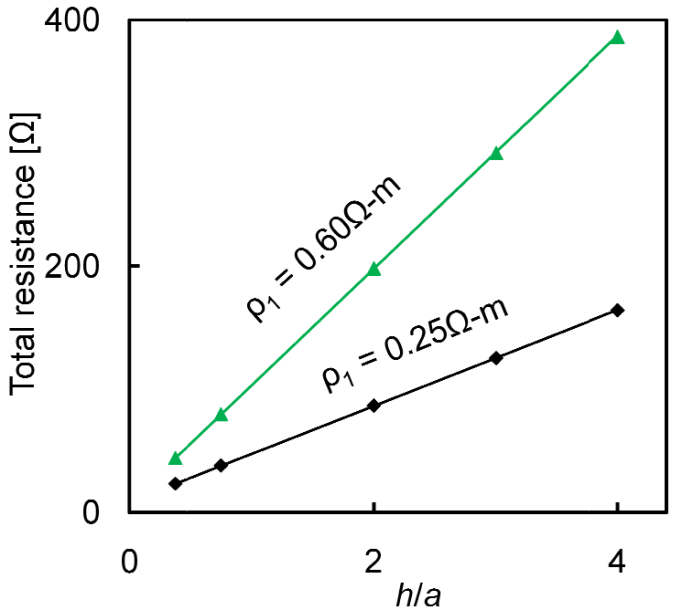

Fig. 2.8 Sample calculations of the total resistance *R* of a cylindrical channel according to MAXWELL 3D simulation (symbols) and the scaling law (solid lines).

A sample comparison of the scaling law, Eq. (2.7), against the MAXWELL 3D [85] simulation of a cylindrical channel is shown in Fig. 2.8. Excellent agreement is noted. In this example, we set ρ_1 = 0.25 (and 0.60) Ωm, ρ_2 = 0.038 Ωm, ρ_3 = 0.001 Ωm, a = 4 mm, b = 8 mm, c =10 mm, the lengths of conductor II and III were equal, 2h ranging

from 1.5 to 16 mm, the total axial length of the current channel simulated was fixed at 80 mm, and an excitation voltage of 10V was applied.

Case D. Experimental validation with $\rho_1 = \rho_2 = \rho_3$ [24]

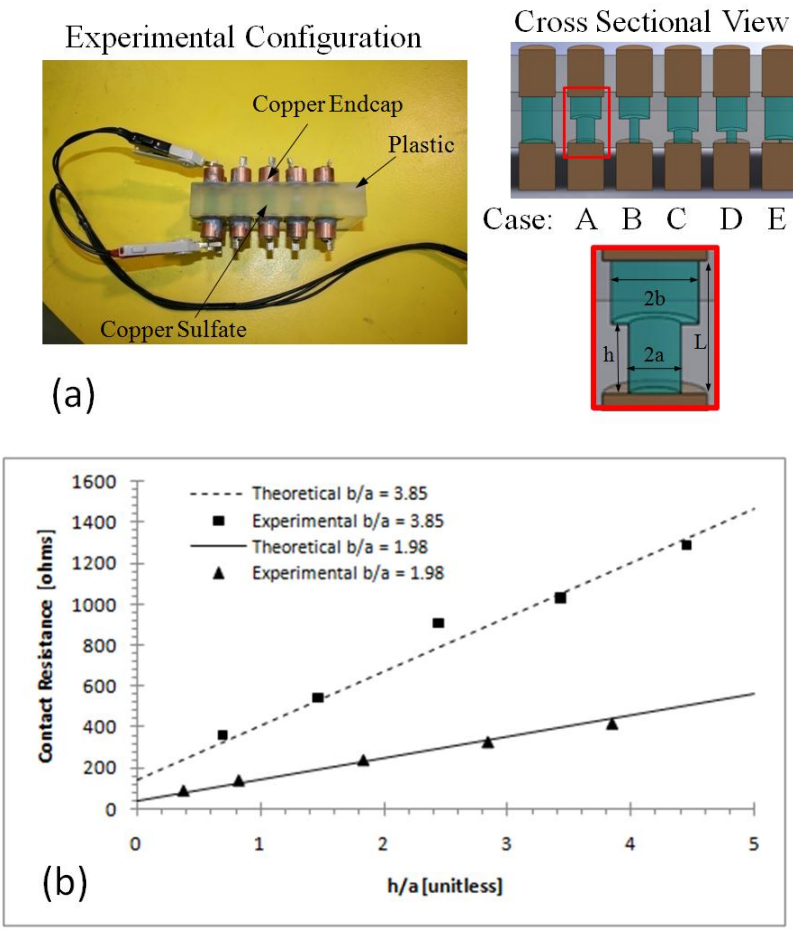

Fig. 2.9 Experimental validation of the scaling law for contact resistance, Eq. (2.7), for the special case of uniform resistivity by Gomez *et al*. [24]. (a) Experimental setup. All channels had diameter 2*b*=15.9±0.1 mm, and length *L*= 40.8±0.2 mm, 2*a* = 4(or 8)±0.1mm, *h* varied from 1.5 to 9.1±0.2mm. (b) Measured contact resistance in good agreement with theoretical results.

In this case, all channels are made of the same material. The experimental validation was performed previously [24]. It is included here for completeness because

$\rho_1 = \rho_2 = \rho_3$ is a special case of the general theory presented in this thesis. The limiting case $b = c$ was also analyzed in great detail in Lau and Tang [23], and was subjected to an experimental test by Gomez *et al.* at University of Michigan [24]. Due to its nature that contact resistance is highly random, it is very difficult to test the theory via experiments using solid conductor. Instead, Gomez *et al* designed an experiment to mimic the theoretical contact resistance geometry (Fig. 2.3 and Fig. 2.4), by machining holes of varying diameter in a piece of plastic and filling it with copper sulfate solution, as shown in Fig. 2.9 (a). The resistance of such copper sulfate channels was measured. The experimental results of Gomez *et al*. [24] were in good agreement with the theory, as shown in Fig. 2.9 (b).

In summary, the scaling laws given in the present chapter, aimed at vastly different values of ρ_1, ρ_2 and ρ_3, introduces a small error that is represented by the last term in Eqs. (2.2) and (2.5). This small error, which is less than 10% in the worst case, is already included in Fig. 2.5 and Fig. 2.6, and is the price we pay for the explicit scaling law that is applicable over a huge variation in materials properties and in channel geometries, as demonstrated in these figures.

2.4 Concluding Remarks

We model a single asperity (Fig. 2.1) by Fig. 2.3. Having performed several checks on the validity of the scaling laws for the contact resistance joining two current channels,

II and III (Fig. 2.3), we may now draw some general conclusions regarding the bulk contact resistance of a single asperity that is comprised of the second, third and fourth terms in the RHS of the scaling laws, Eqs. (2.7) and (2.8). The third term represents the bulk resistance of the electrical contact, Region I, and the second and fourth term represents the interface resistance at $z = 0$ and at $z = 2h$ (Fig. 2.3).

(a) If the electrical contact (Region I) is highly resistive ($\rho_1 >> \rho_2$, $\rho_1 >> \rho_3$), then the bulk resistance (the third term on the RHS of Eqs. 2.7 and 2.8) dominates over the interface resistance (the second and fourth term on the RHS of Eqs. 2.7 and 2.8) once the contact region's axial length ($2h$) exceeds a few times $(\rho_2/\rho_1)a$ and $(\rho_3/\rho_1)a$.

(b) Once the geometry (a,b,c,h) is specified, the interface resistance depends mainly on the electrical resistivity of the main channel (ρ_2, ρ_3); it is insensitive to the resistivity of the contact region (ρ_1). To see this, examine the second term in Eq. (2.7), or in Eq. (2.8), for instance. This term shows that the interface resistance is linearly proportional to the current channel resistivity, ρ_2, but is quite insensitive to the ratio ρ_1/ρ_2, as shown in Fig. 2.5(b) and Fig. 2.6(b).

(c) The exact formulation for the interface resistance in Fig. 2.3 is quite difficult to obtain for general values of a, b, c, h, ρ_1, ρ_2 and ρ_3. The interface resistance is not easy to extract from a numerical code either, especially when there is a large contrast between ρ_1 and ρ_2, or between ρ_1 and ρ_3, or between any of the geometric dimensions h, a, b, c, L_2, and L_3. Likewise, experimental verification for the

interface resistance is not easy to achieve either, if there is a large contrast in any of the above-mentioned parameters. Despite some small intrinsic errors, of order 10 percent or less, the simple scaling laws established in this paper then offer some new insight that is hitherto unavailable in the existing literature.

(d) The composite contact resistance in a realistic contact (Fig. 2.1) may be attempted with the model shown in Fig. 2.3, for which we solved almost exactly with accurate scaling law for the contact resistance. Figure 2.3 may be considered as a prototype for Fig. 2.1 for an individual asperity in a statistical theory.

CHAPTER 3

THIN FILM CONTACT RESISTANCE

3.1 Introduction

Thin film contact is a very important issue in many areas, such as integrated circuits [38-40], thin film devices [16, 17, 37], carbon nanotube and carbon nanofiber based cathodes [41-43] and interconnects [41, 44-46], field emitters [9, 41, 43], and thin film-to-bulk contacts [20-22], etc. Even in the simplest form, film resistor remains the most fundamental component of various types of circuits [16, 17]. Recently, it becomes increasingly important in the miniaturization of electronic devices such as micro-electromechanical system (MEMS) relays and microconnector systems, where thin metal films of a few microns are typically used to form electrical contacts [21, 22]. In high energy density physics, the electrical contacts between the electrode plates and in Z-pinch wire arrays are crucial for high current delivery [2-4]. The methodology we used to treat bulk contacts with dissimilar materials in Chapter 2 is naturally extended in this chapter to treat thin film contacts with dissimilar materials, an important problem seemingly rarely analyzed with field theory in the open literature of the semiconductor

community.

While Holm's classical *a*-spot theory [12] has been extended to include the effects of finite bulk radius [15], of finite thickness of contact "bridge" [23, 24], and of dissimilar materials and contaminants [25], as discussed in Chapter 2, these prior works are inapplicable to the thin film geometry that is studied in this Chapter (Fig. 3.1 - Fig. 3.3). This is particularly the case when the current is mostly confined to the immediate vicinity of the constriction and flows parallel to the thin film boundary.

Figure 3.1 shows both Cartesian and cylindrical geometries of the thin film. The current flows inside the base thin film with width (thickness) h and electrical resistivity ρ_2, converging towards the center of the joint region, and feeds into the top channel with half-width (radius) a and electrical resistivity ρ_1, in Cartesian (cylindrical) geometry. This configuration is representative to various applications. The Cartesian case may represent a thin film sheet resistor (Fig. 3.2(a)) [16, 17], where the third dimension, which is perpendicular to the plane of the paper, is small. It may also represent a heatsink geometry (Fig. 3.2(b)), where this third dimension is large. The cylindrical case (Fig. 3.3) may represent a carbon nanotube [41-46] or a field emitter [41, 43] setting on a substrate; or it may represent a z-pinch wire connected to a plate electrode [2-4].

The two-dimensional (2D) thin film resistance has been investigated for various patterns in Cartesian geometry [16, 17]. The spreading resistance of three-dimensional (3D) thin film disks is also analyzed [20-22, 27]. These prior works assume a constant and uniform electrical resistivity in all regions. In particular, Timsit [20] analytically

calculated the spreading resistance of a circular thin conducting film of thickness h connected to a bulk solid via an a-spot constriction of radius a, but with the assumption that the current density distribution through the a-spot of this film is the same as the known current density distribution through the a-spot in a semi-infinite bulk solid [15, 20]. Timsit stated that his model is reliable only for $0 < a/h \leq 0.5$ [20]. Here, we are able to confirm Timsit's results for $0 < a/h \leq 0.5$, and at the same time to extend his results for a/h up to ten [29] [cf. the lowest solid curve in Fig. 3.11(a, b)].

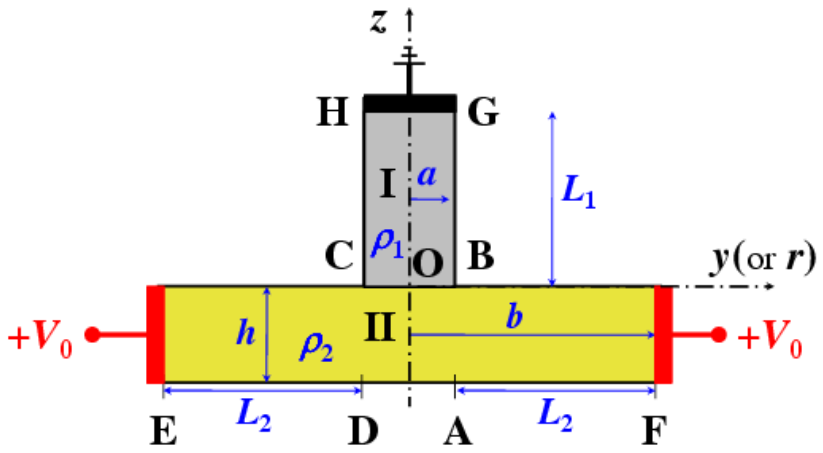

Fig. 3.1 Thin film structures in either Cartesian or cylindrical geometries. Terminals *E* and *F* are held at a constant voltage (V_0) relative to terminal *GH*, which is grounded. The z-axis is the axis of rotation for the cylindrical geometry. The resistivity ratio ρ_1/ρ_2 in Regions I and II is arbitrary.

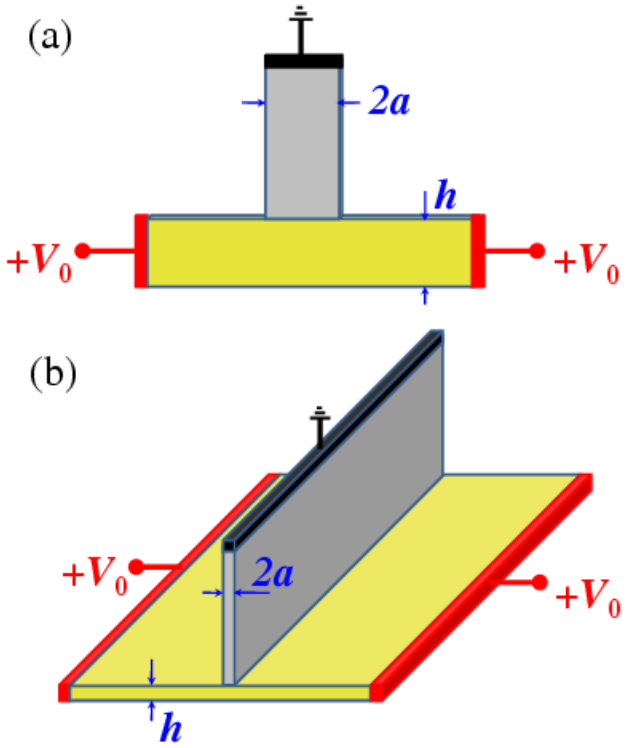

Fig. 3.2 Two cases of Cartesian thin film contact represented by Fig. 3.1: (a) thin film sheet resistor, and (b) heatsink geometry*.

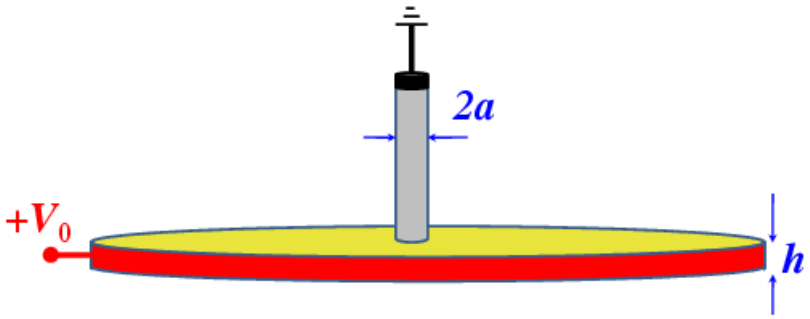

Fig. 3.3 Cylindrical case of thin film contact represented by Fig. 3.1.

We analyze the model shown in Fig. 3.1. We assume that the axial extent of the top channel (i.e. L_1 in Fig. 3.1) is so long that the current flow in this region is uniform

* Typical heat sink structures can be found at http://en.wikipedia.org/wiki/Heat_sink

far from the contact region. Our analytic formulation (given in detail in the Appendices C and E) assume a finite length L_2 in the base region (Fig. 3.1). Thus, we study the dependence of the contact or constriction resistance on the geometries and resistivities shown in Fig. 3.1, for arbitrary values of a, b, h, ρ_1, and ρ_2 (Fig. 3.4, Fig. 3.5, Fig. 3.10, Fig. 3.11). The potential profiles are formulated exactly, from which the interface contact resistances are derived. Simple, accurate scaling laws for the thin film contact resistance are synthesized (Fig. 3.7 and Fig. 3.13). The patterns of current flow are also displayed, where the crowding of the current flow lines in the contact region suggests intense local heating there. The conditions to minimize the contact resistance are identified in various limits. Validation of our theory against known results is indicated.

In the limit of $h \to 0$, the normalized thin film spreading resistance is found to converge to some finite constant values, for both Cartesian and cylindrical geometries. An interpretation of these limits is given. We conjecture that the same finite limits of normalized thin film spreading resistance would apply to the a-spot between bulk solids in the high frequency AC case where the skin depth $\delta \to 0$, if the thickness of the equivalent thin film is identified as the skin depth at the relevant frequency, i.e., $h = \delta$. Extension to general a-spot geometry is given in Section 3.5.

Section 3.2 considers Cartesian geometry. Section 3.3 considers cylindrical geometry. Section 3.4 considers the thin film limit ($h \to 0$). The insight obtained led to the proposed generalization to an arbitrary a-spot geometry and to the high frequency limits, which are treated in Section 3.5. Section 3.6 summarizes this chapter.

Similar to Chapter 2, only the major results will be presented in the main text. Their derivations are given in the appendices.

3.2 Cartesian Thin Film Contact with Dissimilar Materials

Let us first consider the 2D Cartesian "T"-shape thin film pattern (Fig. 3.1 and Fig. 3.2). The pattern is symmetrical about the vertical center axis. Current flows from the two terminals *E*, *F* to the top terminal *GH* (Fig. 3.1). We solve the Laplace's equation for Region I and Region II, and match the boundary conditions at the interface BC, $z = 0$. The details of the calculations are given in the Appendix C. The total resistance, *R*, from *EF* to *GH* is found to be,

$$R = \frac{\rho_2 L_2}{2h \times W} + \frac{\rho_2}{4\pi W} \overline{R}_c \left(\frac{a}{b}, \frac{a}{h}, \frac{\rho_1}{\rho_2} \right) + \frac{\rho_1 L_1}{2a \times W}, \tag{3.1}$$

where *W* denotes the channel width in the third, ignorable dimension that is perpendicular to the paper, and the rest of the symbols have been defined in Fig. 3.1. In Eq. (3.1), the first term represents the bulk resistance of the thin film base, from *A* to *F*, and from *D* to *E*, where $L_2 = b - a$. The third term represents the bulk resistance of the top region from *B* to *G*. The second term represents the remaining constriction (or contact) resistance, R_c, for the region *ABCD*. If we express the constriction (contact) resistance as $R_c = (\rho_2 / 4\pi W)\overline{R}_c$ for the Cartesian case, we find that $\overline{R}_c$ depends on the aspect ratios *a*/*h* and *a*/*b*, and on the resistivity ratio ρ_1/ρ_2, as explicitly shown in Eq. (3.1). The *exact* expression for $\overline{R}_c$ is derived in Appendix C [cf. Eq. (C8)]. In Eq. (C8), the coefficient

B_n is solved numerically in terms of ρ_1/ρ_2, a/h, and a/b [cf. Eq. (C6)]. The infinite matrix, Eq. (C6), is solved directly by MATLAB, with increasing number of terms included until convergence is realized. These numerical values of B_n then give $\overline{R}_c$ from Eq. (C8).

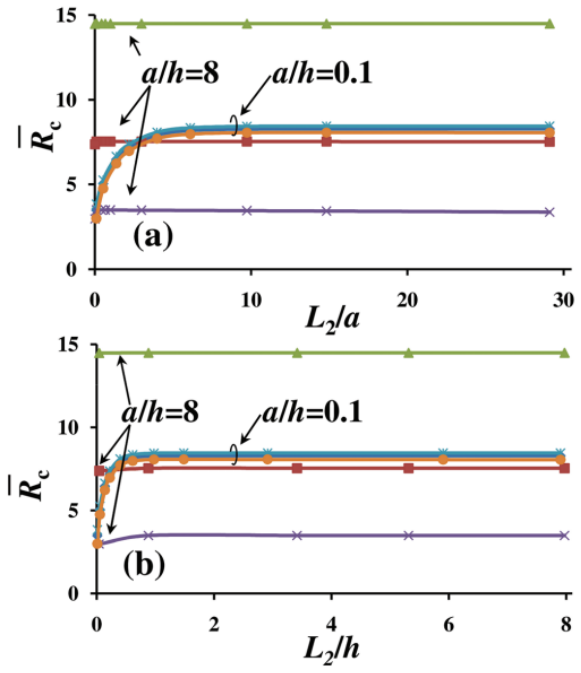

Fig. 3.4 $\overline{R}_c$ for the Cartesian structure in Fig. 3.1 and Fig. 3.2, is plotted as a function of (a) L_2/a, and (b) L_2/h, for a/h = 0.1 and 8.0, and ρ_1/ρ_2 = 10, 1.0, and 0.1 (top to bottom).

The exact theory of $\overline{R}_c$ [cf. Eq. (C8)] is plotted in Fig. 3.4(a) as a function of L_2/a, for various ρ_1/ρ_2 and a/h. To explicitly examine the dependence on the geometrical parameters, $\overline{R}_c$ in Fig. 3.4(a) is replotted as a function of L_2/h in Fig. 3.4(b). It is seen from Fig. 3.4 that $\overline{R}_c$ becomes almost a constant if either $L_2/a >> 1$ or $L_2/h >> 1$, in which case $\overline{R}_c$ is determined only by the value of a/h and ρ_1/ρ_2, independent of b. Many other similar calculations (not shown) lead to the same conclusion. This is due to the fact

that if $L_2 >> a$, the electrostatic fringe field at the corner B (Fig. 3.1) is restricted to a distance of at most a few a's, making the flow field at the terminal F insensitive to b. Likewise, if $L_2 >> h$, the electrostatic fringe field at the corner B is restricted to a distance of at most a few h's, making the flow field at the terminal F also insensitive to b.

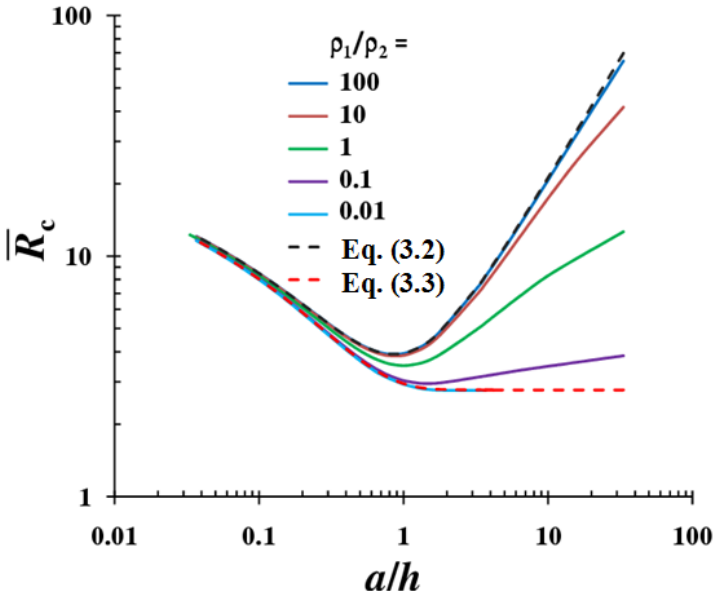

Fig. 3.5 $\overline{R}_c$ as a function of *a*/*h*, for the Cartesian structure in Fig. 3.1 and Fig. 3.2. The solid line represents the exact calculations [Eq. (C8)], where each curve consists of many combinations of *b*/*a* and *b*/*h*, with either $L_2 >> a$ or $L_2 >> h$. The dashed lines respresent the limiting cases of $\rho_1/\rho_2 \to \infty$ [Eqs. (3.2)] and $\rho_1/\rho_2 \to 0$ [Eq. (3.3)], whose asymptotes for a/h >> 1 are, respectively, $\overline{R}_c \simeq (2\pi/3)a/h$, and $\overline{R}_c \simeq 4\ell n2 = 2.77$.

In Fig. 3.5, the exact theory of $\overline{R}_c$ [cf. Eq. (C8)] is plotted as a function of *a*/*h*, for various ρ_1/ρ_2. Each solid curve in Fig. 3.5 consists of many combinations of *b*/*a* and *b*/*h*, with either $L_2 >> a$ or $L_2 >> h$. Again, $\overline{R}_c$ is independent of *b*, provided either

$L_2 >> a$ or $L_2 >> h$. For a given a/h, $\overline{R}_c$ increases as ρ_1/ρ_2 increases. It is clear that there exists a minimum value of $\overline{R}_c$ in the region of a/h near unity, for a given ρ_1/ρ_2. This a/h value for minimum $\overline{R}_c$ decreases slightly as ρ_1/ρ_2 increases. In the regime $a/h < 1$, the range of variation $\overline{R}_c(\rho_1/\rho_2)$ for a given a/h is insignificant (Fig. 3.5); however, in the regime of $a/h > 1$, $\overline{R}_c(\rho_1/\rho_2)$ for a given a/h may change by an order of magnitude or more.

In the limit of $\rho_1/\rho_2 \to \infty$, $\overline{R}_c$ is simplified as (cf. Eq. (C10) in Appendix C),

$$\overline{R}_c\Big|_{\rho_1/\rho_2\to\infty} = 4\sum_{n=1}^{\infty} \frac{\coth\left((n-1/2)\pi h/b\right)}{n-1/2} \frac{\sin^2\left((n-1/2)\pi a/b\right)}{\left((n-1/2)\pi a/b\right)^2} - 2\pi(b-a)/h, \qquad (3.2)$$

which is also plotted in Fig. 3.5. Note that the exact theory for $\rho_1/\rho_2 = 100$ overlaps with Eq. (3.2). In the limit of $\rho_1/\rho_2 \to \infty$, the minimum $\overline{R}_c \cong 3.9$ occurs at $a/h = 0.85$, as shown in Fig. 3.5. We prove in Appendix C that, as $a/h \to \infty$, Eq. (3.2) yields $\overline{R}_c\Big|_{\rho_1/\rho_2\to\infty} = (2\pi/3)a/h$, as shown in the top curve in Fig. 3.5, independent of b/a (>1).

In the opposite limit, $\rho_1/\rho_2 \to 0$, the region *BCHG* (Fig. 3.1) acts as a perfectly conducting material with respect to the base region *BCEF*. Thus, the whole constriction interface *BC* is an equipotential surface, as if $L_1 = 0$ and the external electrode is applied directly to the interface *BC* for the Cartesian geometry. This special case is analyzed by Hall (cf. Fig. 2 and Eq. (12) of Hall's 1967 paper [16]), and from which $\overline{R}_c$ in the limit of $\rho_1/\rho_2 \to 0$ is given as,

$$\overline{R}_c\Big|_{\rho_1/\rho_2\to 0} = 2\pi\frac{a}{h} - 4\ln\left[\sinh\left(\frac{\pi}{2}\frac{a}{h}\right)\right], \qquad (3.3)$$

which is also plotted in Fig. 3.5. Note that the exact theory for $\rho_1/\rho_2 = 0.01$ overlaps with

Eq. (3.3). This agreement may be considered as one validation of the analytic theory presented in Appendix C. In the limit of $\rho_1/\rho_2 \to 0$, Eq. (3.3) shows that $\overline{R}_c$ converges to a constant minimum value of 4ln2 = 2.77 as $a/h \to \infty$, as shown in Fig. 3.5 for $a/h \geq 2$.

Thus, the scaling law for $a/h >> 1$ in the two limits $\rho_1/\rho_2 \to \infty$ and $\rho_1/\rho_2 \to 0$ reads,

$$\overline{R}_c \simeq \begin{cases} \dfrac{2\pi}{3}\left(\dfrac{a}{h}\right), & \rho_1/\rho_2 \to \infty; \\ 4\ell n2 = 2.77, & \rho_1/\rho_2 \to 0. \end{cases} \tag{3.3a}$$

These limits are apparent in Fig. 3.5 for $a/h >> 1$.

For the special case of $\rho_1/\rho_2 = 1$, the *exact* expression for $\overline{R}_c$ can be simply derived from conformal mapping (see Appendix D for details, and Eq. (D8)) [16, 17, 23, 28, 92],

$$\overline{R}_c\left(\frac{a}{h}\right)\Big|_{\rho_1/\rho_2=1} = 4\ln\left[\frac{1}{4}\left(\frac{a}{h}+\frac{h}{a}\right)\right] + 4\left(\frac{h}{a}\right)\tan^{-1}\left(\frac{a}{h}\right) + 4\left(\frac{a}{h}\right)\tan^{-1}\left(\frac{h}{a}\right), \tag{3.4}$$

which is plotted in Fig. 3.6. For $a/h >1$, $\overline{R}_c$ increases as a/h increases. For $a/h <1$, $\overline{R}_c$ increases as a/h decreases. This behavior is easily understood since the current flow paths will be lengthened whenever the aspect ratio of a/h deviates from 1. Thus, the constriction (contact) resistance is minimized when $a = h$, at which $\overline{R}_c = 2\pi - 4\ln 2 = 3.5106$. Taylor expansion of Eq. (3.4) yields the asymptotic expressions

$$\overline{R}_c\big|_{\rho_1/\rho_2=1} \cong \begin{cases} -4\ln(a/h) - 8\ln 2 + 4, & a/h << 1; \\ 4\ln(a/h) - 8\ln 2 + 4, & a/h >> 1, \end{cases} \tag{3.5}$$

which is also shown in Fig. 3.6.

Included in Fig. 3.6 is the exact calculation of $\bar{R}_c$ for the special case of ρ_1/ρ_2 = 1 from the series expansion method [cf. Eq. (C8)]. Excellent agreement between the series expansion method and conformal mapping is noted [28]. This validation added confidence on the Fourier series expansion method as applied to the cylindrical geometry, reported in Section 3.3 below, which cannot be treated with conformal mapping.

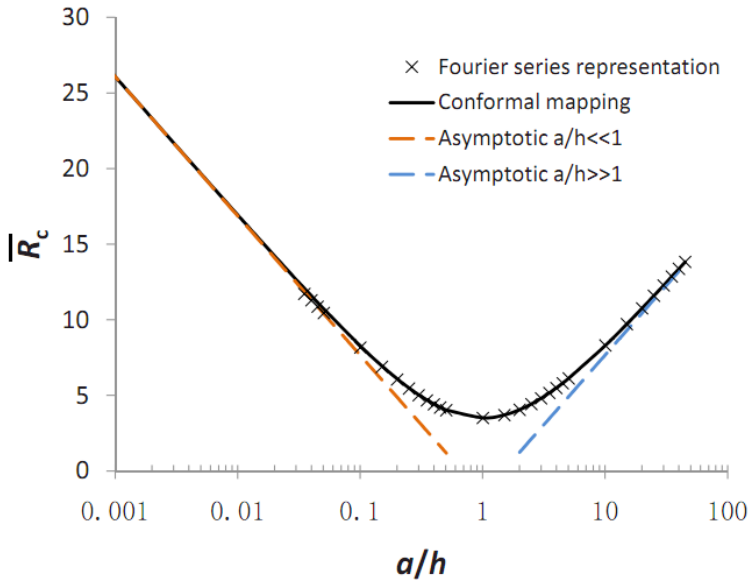

Fig. 3.6 $\bar{R}_c$ as a function of *a*/*h*, for the special case of ρ_1/ρ_2 = 1 of the Cartesian structure in Fig. 3.1 and Fig. 3.2. The solid line represents the conformal mapping results [Eq. (3.4)], the dashed lines respresent the asymptotes [Eq. (3.5)], and the symbols represents the exact Fourier series representation calculation [cf. Eq. (C8)].

As another validation, consider the special case ρ_1/ρ_2 = 1 and L_2 = 0 (Fig. 3.1). This case has an exact solution using conformal mapping, given by Eq. (3.3) but interchanging *a* and *h*. The exact values of $\bar{R}_c$ for *a*/*h* = 0.1 and *a*/*h* = 8 obtained from conformal mapping are, respectively, 2.77259 and 7.27116. In comparison, our numerical values

from series expansion method are, respectively, 2.7722 and 7.2692, as shown in the data for $L_2 = 0$ in Fig. 3.4(a) or Fig. 3.4(b).

The vast amount of data collected from the exact calculations allows us to synthesize a simple scaling law for the normalized contact resistance $\overline{R}_c$ in Eq. (3.1) and Fig. 3.5 as, (for $L_2 >> a$ or $L_2 >> h$),

$$\overline{R}_c\left(\frac{a}{h},\frac{\rho_1}{\rho_2}\right) \cong \overline{R}_{c0}\left(\frac{a}{h}\right) + \frac{\Delta\left(\frac{a}{h}\right)}{2} \times \frac{2\rho_1}{\rho_1 + \beta\left(\frac{a}{h}\right)\rho_2}, \tag{3.6}$$

$$\overline{R}_{c0}\left(a/h\right) = \overline{R}_c\left(a/h\right)\Big|_{\rho_1/\rho_2 \to 0} = 2\pi a/h - 4\ln\left[\sinh\left(\pi a/2h\right)\right], \tag{3.7}$$

$$\Delta\left(a/h\right) = \begin{cases} 0.5346\left(a/h\right)^2 + 0.0127\left(a/h\right) + 0.4548, & 0.03 \le a/h \le 1; \\ 0.0147x^6 - 0.0355x^5 + 0.1479x^4 + 0.4193x^3 + 1.1163x^2 + 0.9970x + 1, & \\ \qquad x = \ln(a/h), 1 < a/h \le 30, & \end{cases}$$

$$\beta\left(a/h\right) = -0.0003\left(a/h\right)^2 + 0.1649\left(a/h\right) + 0.6727, \ 0.03 \le a/h \le 30. \tag{3.8}$$

This scaling law of Cartesian thin film contact resistance, Eq. (3.6), is shown in Fig. 3.7, which compares extremely well with the exact theory, for the range of $0 < \rho_1/\rho_2 < \infty$ and $0.03 \le a/h \le 30$. (We have not found the scaling law for $a/h > 30$ for general values of ρ_1/ρ_2, except in the limits $\rho_1/\rho_2 \to 0$ and $\rho_1/\rho_2 \to \infty$, that is stated in the caption of Fig. 3.5, and displayed in Eq. (3.3a).)

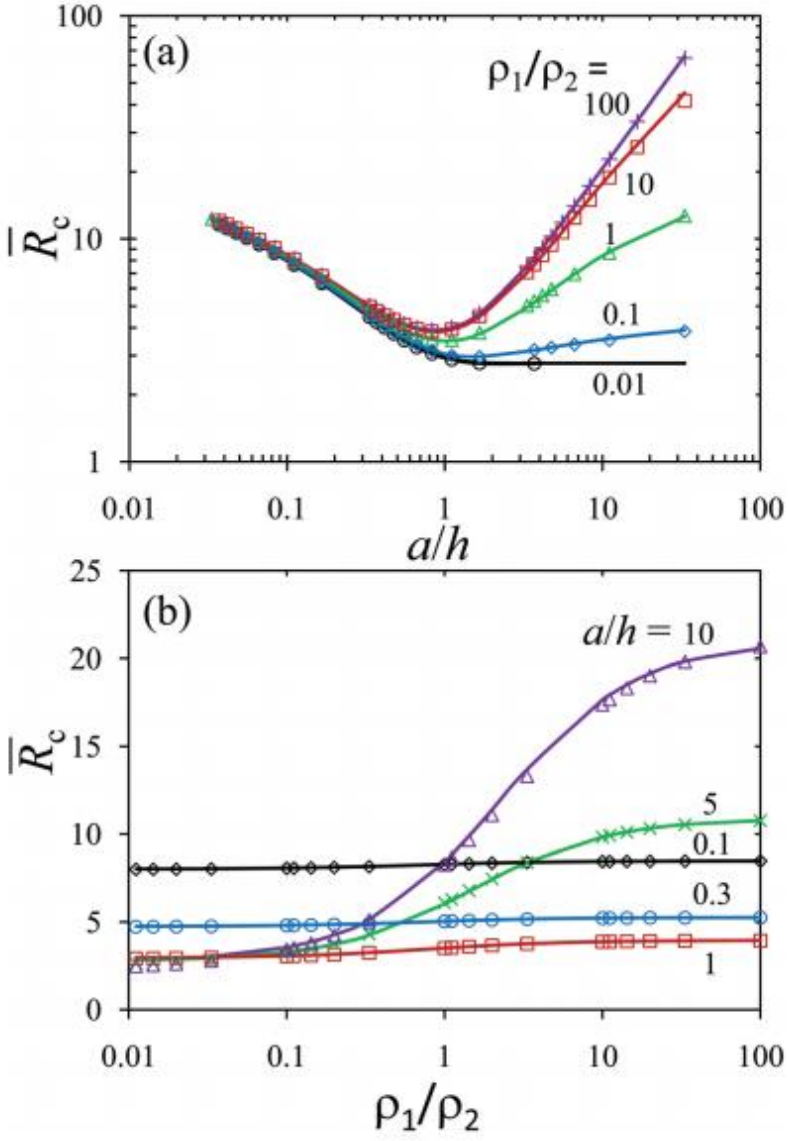

Fig. 3.7 $\overline{R}_c$ for Cartesian thin film structures in Fig. 3.1 and Fig. 3.2, as a function of (a) aspect ratio *a*/*h*, and (b) resistivity ratio ρ_1/ρ_2; symbols for the exact theory, solid lines for the scaling law Eq. (3.6).

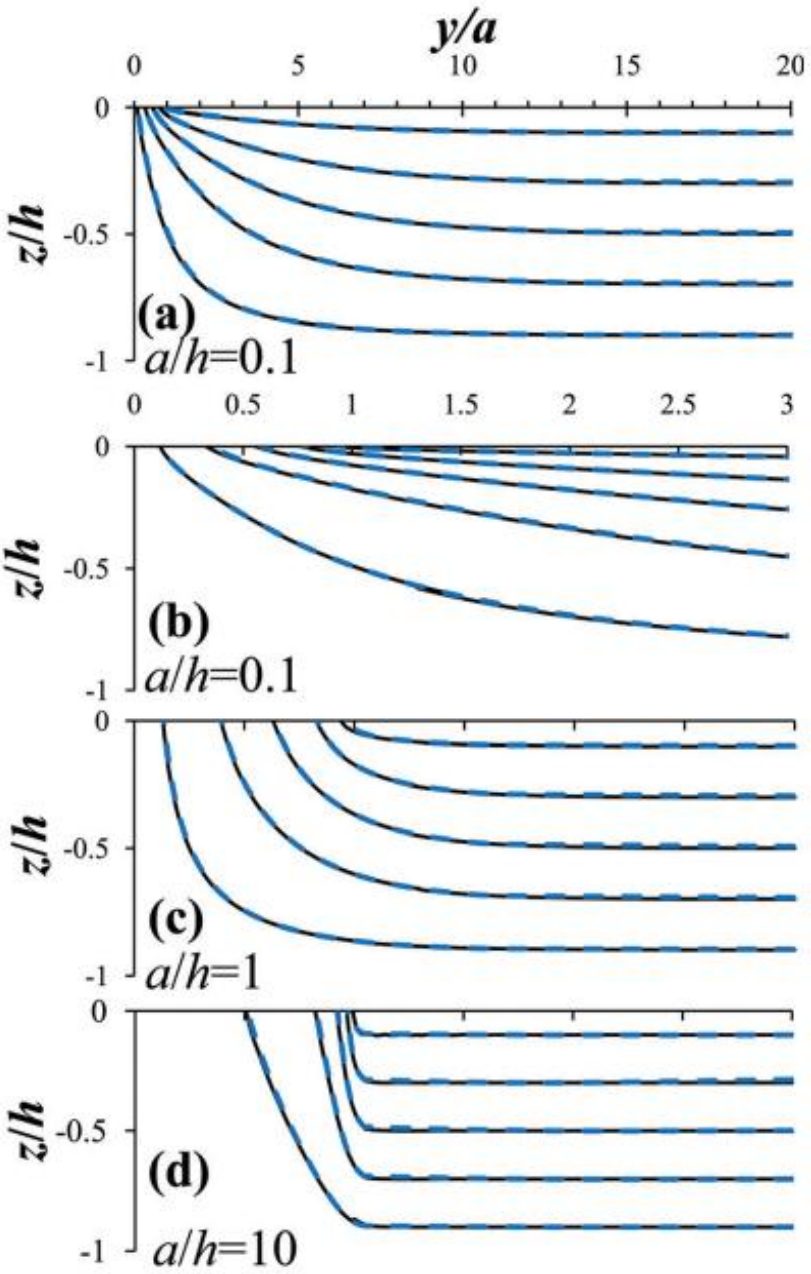

Fig. 3.8 Electric field lines in the right half of Region II of the Cartesian geometry in Fig. 3.1 for $\rho_1/\rho_2 = 1$ with (a) $a/h = 0.1$, (b) zoom in view of (a) for $0 \le y/a \le 3$, (c) $a/h = 1$, and (d) $a/h = 10$. The results from series expansion method [Eq. (C1)] (solid lines) are compared to those from conformal mapping (dashed lines).

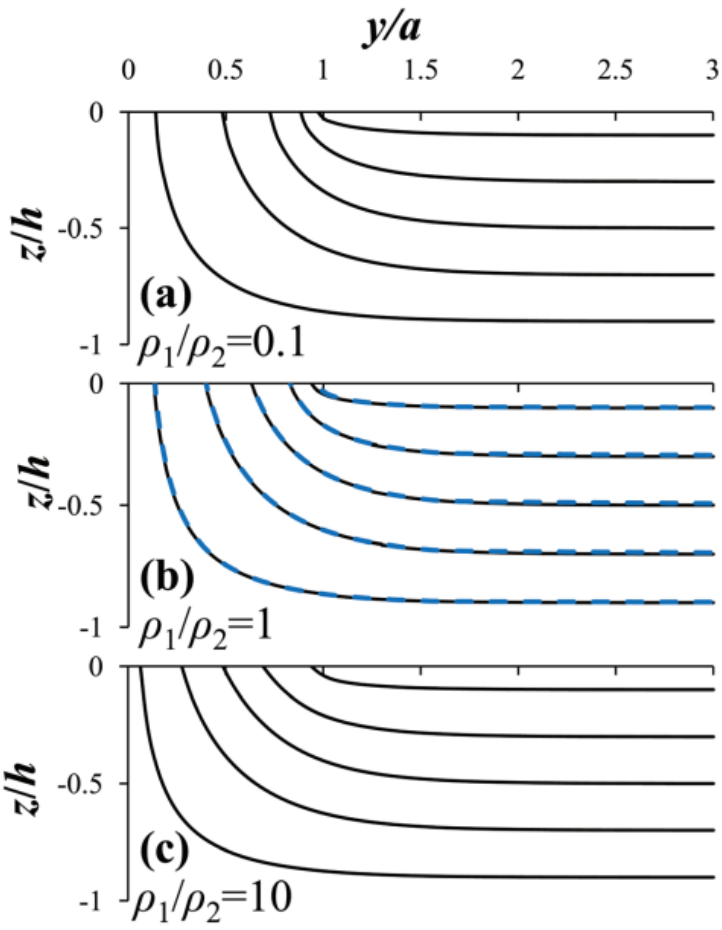

Fig. 3.9 Electric field lines in the right half of Region II of the Cartesian geometry in Fig. 3.1 for a/h = 1 with (a) ρ_1/ρ_2 = 0.1, (b) ρ_1/ρ_2 = 1, and (c) ρ_1/ρ_2 = 10. For ρ_1/ρ_2 = 1, the results from series expansion method [Eq. (C1)] (solid lines) are compared to those from conformal mapping (dashed lines).

The field line equation, $y = y(z)$ for $z < 0$, may be numerically integrated from the first order ordinary differential equation $dy/dz = E_y/E_z = (\partial\Phi_-/\partial y)/(\partial\Phi_-/\partial z)$ where Φ_- is given by Eq. (C1). Figure 3.8 shows the field lines in the right half of Region II (Fig. 3.1) for the special case of ρ_1/ρ_2 = 1, with various aspect ratios a/h. It is clear that the field lines are most uniformly distributed over the conduction region when a/h = 1,

which is consistent with the minimum normalized contact resistance $\overline{R}_c$ at $a/h = 1$ for $\rho_1/\rho_2 = 1$ (Fig. 3.6). The field lines are *horizontally* crowded around the corner of the constriction when $a/h << 1$ [Fig. 3.8 (b)], since in this limit most of the potential variations in the thin film (Region II in Fig. 3.1) are restricted to a distance of a few a's. The field lines become *vertically* crowded around the corner of the constriction when $a/h >> 1$ [Fig. 3.8 (d)], since in this limit most of the potential variations in the upper region (Region I in Fig. 3.1) are restricted to a distance of a few h's. Both limits lead to higher contact resistance in general (Fig. 3.5 and Fig. 3.6). The crowding of the field lines near the constriction corner could lead to significant ohmic heating there. In Fig. 3.9, the field lines are shown for the special case of $a/h = 1$, with various resistivity ratios ρ_1/ρ_2. As ρ_1/ρ_2 increases, Region II becomes more conductive relative to Region I, the interface between Region I and II (i.e. BC in Fig. 3.1) becomes more and more like equipotential, therefore, the field lines (and the current density) at the interface become more uniformly distributed, as shown in Fig. 3.9 (c). For $\rho_1/\rho_2 = 1$, the calculated field lines [from Eq. (C1)] are also compared to those obtained from conformal mapping [cf. Eq. (D1)], with excellent agreement for all calculations, as shown in Fig. 3.8 and Fig. 3.9 (b). This close agreement of the field lines with the exact conformal mapping formulation is another validation of the series expansion method.

3.3 Cylindrical Thin Film Contact with Dissimilar Materials

We now consider the cylindrical configuration of Fig. 3.1 using only the series expansion method, as conformal mapping can no longer be applied to this cylindrical geometry. A long cylindrical rod of radius a with resistivity ρ_1, is standing on the center of large thin-film circular disk of thickness h, and radius $b = a + L_2$ with resistivity ρ_2. Current flows inside the thin-film disk, from circular rim, E and F, to terminal GH (Fig. 3.1 and Fig. 3.3). We solve the Laplace's equation for Region I and Region II, and match the boundary conditions at the interface BC, $z = 0$. The details of the calculations are given in the Appendix E. The total resistance, R, from EF to GH is found to be,

$$R = \frac{\rho_2}{2\pi h}\ln\left(\frac{b}{a}\right) + \frac{\rho_2}{4a}\overline{R}_c\left(\frac{a}{b}, \frac{a}{h}, \frac{\rho_1}{\rho_2}\right) + \frac{\rho_1 L_1}{\pi a^2}. \tag{3.9}$$

In Eq. (3.9), the first term represents the bulk resistance of the thin film in Region II, exterior to the constriction region $ABCD$. It is simply the resistance of a disk of inner radius a, outer radius b, and thickness h [20]. The third term represents the bulk resistance of the top cylinder, $BCHG$. The second term represents the remaining constriction resistance, R_c, for the region $ABCD$. If we express the constriction (contact) resistance as $R_c = (\rho_2 / 4a)\overline{R}_c$ for the cylindrical case, we find that $\overline{R}_c$ depends on the aspect ratios a/h and a/b, and on the resistivity ratio ρ_1/ρ_2, as explicitly shown in Eq. (3.9). The *exact* expression for $\overline{R}_c$ is derived in Appendix E [cf. Eq. (E8)]. In Eq. (E8), the coefficient B_n is solved numerically in terms of ρ_1/ρ_2, a/h, and a/b [cf. Eq. (E6)]. These numerical values of B_n then give $\overline{R}_c$ from Eq. (E8).

The exact theory of $\overline{R}_c$ [Eq. (E8)] is plotted in Fig. 3.10(a) as a function of L_2/a, for various ρ_1/ρ_2 and a/h, where $L_2 = b - a$ (Fig. 3.1). To explicitly examine the dependence on the geometrical parameters, $\overline{R}_c$ in Fig. 3.10(a) is replotted as a function of L_2/h in Fig. 3.10(b). Similar to the Cartesian case, we found that $\overline{R}_c$ becomes constant if either $L_2/a >> 1$ or $L_2/h >> 1$, in which case $\overline{R}_c$ is determined only by the value of a/h and ρ_1/ρ_2, independent of b. Many other similar calculations (not shown) lead to the same conclusion. This is due to the fact that if $L_2 >> a$, the electrostatic fringe field at the corner B (Fig. 3.1) is restricted to a distance of at most a few a's, making the flow field at the terminal F insensitive to b. Likewise, if $L_2 >> h$, the electrostatic fringe field at the corner B is restricted to a distance of at most a few h's, making the flow field at the terminal F also insensitive to b.

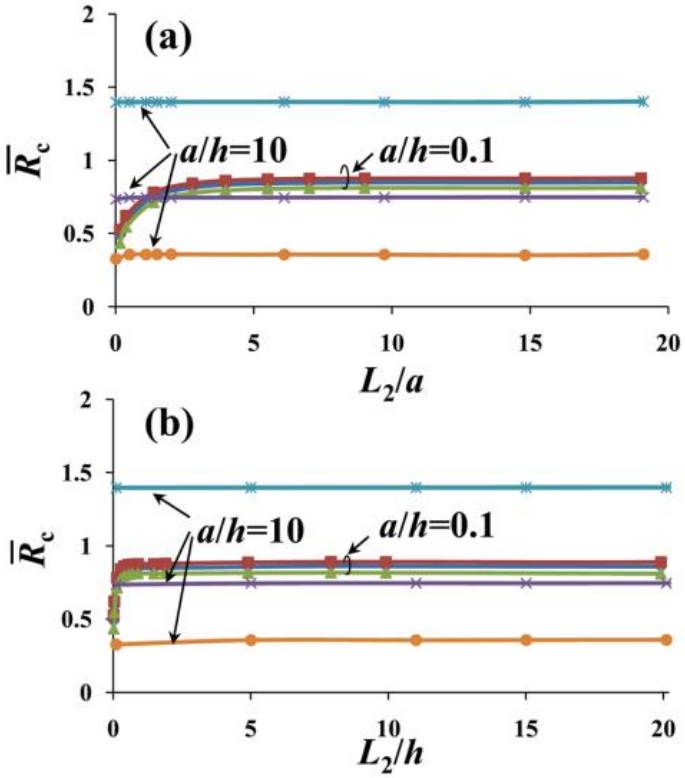

Fig. 3.10 $\overline{R}_c$ for the cylindrical structure in Fig. 3.1 and Fig. 3.3, is plotted as a function of (a) L_2/a, and (b) L_2/h, for a/h = 0.1 and 10.0, and ρ_1/ρ_2 = 10, 1.0, and 0.1 (top to bottom).

In Fig. 3.11, the exact theory of $\overline{R}_c$ [cf. Eq. (E8)] is plotted as a function of a/h, for various ρ_1/ρ_2 and a/b. Again, $\overline{R}_c$ is independent of b, provided either $L_2 >> a$ or $L_2 >> h$. For a given a/h, $\overline{R}_c$ increases as ρ_1/ρ_2 increases, similar to the Cartesian case. It is clear that there is a minimum of value of $\overline{R}_c$ in the region of a/h near 1.5, for a given ρ_1/ρ_2. The a/h value for minimum $\overline{R}_c$ decreases slightly as ρ_1/ρ_2 increases.

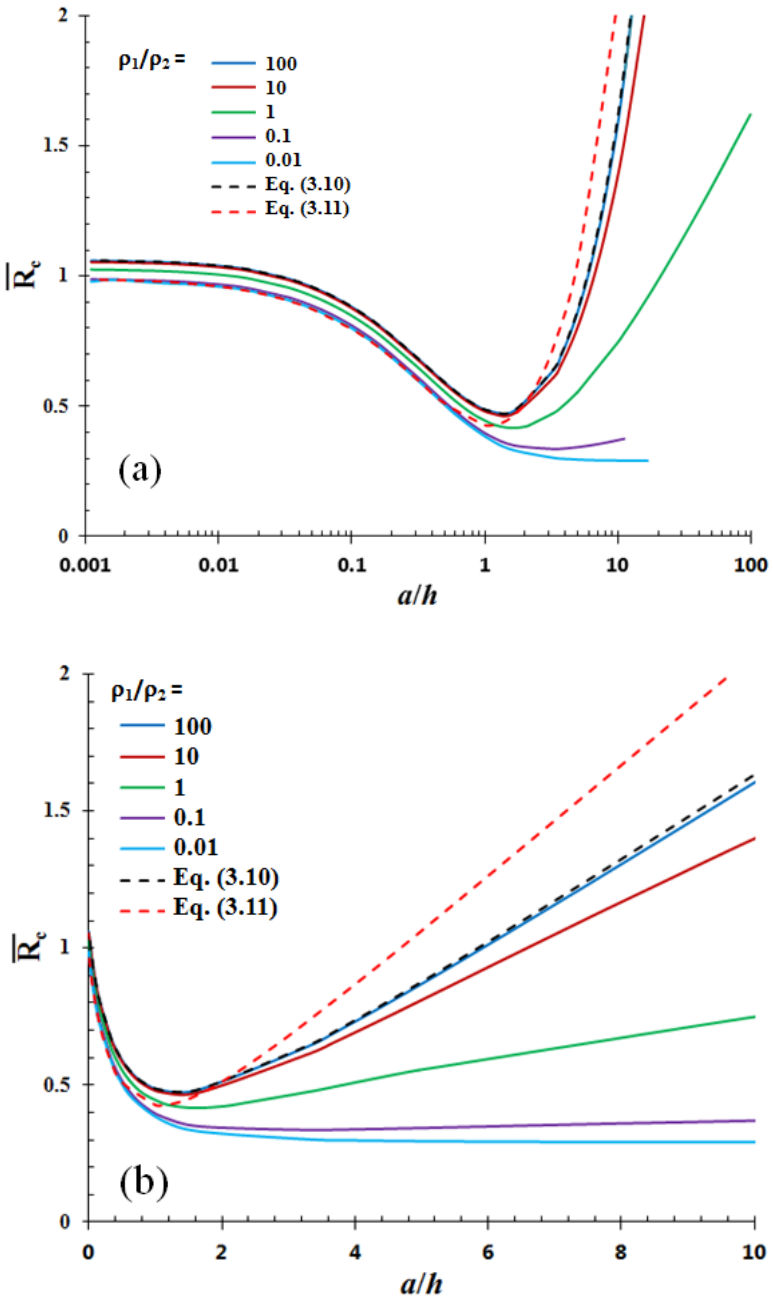

Fig. 3.11 $\bar{R}_c$ **in semi-log plot (a) and linear plot (b) as a function of *a*/*h*, for the cylindrical structure in Fig. 3.1 and Fig. 3.3. The solid lines represent the exact calculations [Eq. (E8)], where each curve consists of many combinations of *b*/*a* and *b*/*h*, with either $L_2 >> a$ or $L_2 >> h$. The dashed lines respresent the limiting cases of $\rho_1/\rho_2 \to \infty$ [Eq. (3.10)] and $\rho_1/\rho_2 \to 0$ [Eq. (3.11), which is valid only for *a*/*h* < 0.5 [20]]. For a/h >> 1,** $\bar{R}_c \simeq (1/2\pi)\, a/h$ **as** $\rho_1/\rho_2 \to \infty$**,**

and $\bar{R}_c \simeq (4\ell n 2)/\pi^2 = 0.28$ **as** $\rho_1/\rho_2 \to 0$**.**

In the regime $a/h < 1$, the variation $\overline{R}_c(\rho_1/\rho_2)$ for a given a/h is insignificant (Fig. 3.11(a)); however, in the regime of $a/h > 1$, $\overline{R}_c(\rho_1/\rho_2)$ for a given a/h changes by a factor in the single digits, up to an order of magnitude as shown in Fig. 3.11. The cylindrical case differs from the Cartesian case in one aspect, namely, as $a/h \to 0$, our numerical calculations show that $\overline{R}_c$ converges to constant values, ranging from about 1 to 1.08, essentially for $0 < \rho_1/\rho_2 < \infty$. The explanation follows. If $a/h \to 0$, both the radius and thickness of the film region are much larger than the radius a of the top cylinder, as if two semi-infinite long cylinders are joining together with radius ratio of $b/a \to \infty$. In this case, the *a*-spot theory [25] gives a value of $\overline{R}_c$ in the range of 1 to 1.08, for $0 < \rho_1/\rho_2 < \infty$ [c.f. Eq. (2.2)].

In the limit of $\rho_1/\rho_2 \to \infty$, $\overline{R}_c$ is simplified as (cf. Eq. (E10) in Appendix E),

$$\overline{R}_c\Big|_{\rho_1/\rho_2 \to \infty} = \frac{16}{\pi}\sum_{n=1}^{\infty} \frac{J_1^2(\lambda_n a/b)}{\lambda_n a/b} \frac{\coth(\lambda_n h/b)}{\lambda_n^2 J_1^2(\lambda_n)} - \frac{2a}{\pi h}\ln(b/a), \qquad (3.10)$$

which is also plotted in Fig. 3.11. Note that the exact theory for $\rho_1/\rho_2 = 100$ overlaps with Eq. (3.10). In the limit of $\rho_1/\rho_2 \to \infty$, the minimum $\overline{R}_c \cong 0.48$ occurs at $a/h = 1.3$, as shown in Fig. 3.11. In the limit of $h \to 0$, Eq. (3.10) approaches the asymptotic limit $\overline{R}_c\Big|_{\rho_1/\rho_2 \to \infty} \to \frac{1}{2\pi}(a/h)$, for all $b/a \geq 1$, as shown in Eq. (E12) and Fig. E1 of Appendix E.

In the opposite limit, $\rho_1/\rho_2 \to 0$, the region *BCHG* (Fig. 3.1) acts as a perfectly conducting material with respect to the base region *BCEF*. Thus, the whole constriction interface *BC* is an equipotential surface, as if $L_1 = 0$ and the external electrode is applied

directly to the interface *BC* for the cylindrical geometry. This special case is analyzed by Timsit (cf. Fig. 7 and Eq. (18) of Ref. [20]), whose $\overline{R}_c$ in the limit of $\rho_1/\rho_2 \to 0$ is,

$$\overline{R}_c\Big|_{\rho_1/\rho_2 \to 0} = \frac{4}{\pi}\sum_{n=1}^{\infty} \coth(\lambda_n h/b)\frac{\sin(\lambda_n a/b)}{\lambda_n^2 J_1^2(\lambda_n)} - \frac{2a}{\pi h}\ln(b/a). \qquad (3.11)$$

Timsit acknowledges that Eq. (3.11) is accurate only for the range of $0 < a/h \le 0.5$ [20], beyond which the assumption of equipotential contact that he introduces to derive Eq. (3.11) does not hold and the result is not accurate anymore. This insight of Timsit and the accuracy of his solution for $a/h < 0.5$ are evident in Fig. 3.11, where Eq. (3.11) is plotted. Note that the exact theory for $\rho_1/\rho_2 = 0.01$ overlaps with Eq. (3.11) up to $a/h = 0.5$. For $a/h > 0.5$, the exact calculation of $\overline{R}_c$ (cf. Eq. (E8)) is also difficult in the limit of $\rho_1/\rho_2 \to 0$, since the determinant of the matrix for solving the coefficient B_n in Eq. (E6) is close to zero. [This is the main reason why the scaling law given in Eq. (3.13) below is valid only for $a/h \le 10$]. Nevertheless, our calculations of $\overline{R}_c$ for $\rho_1/\rho_2 = 0.01$ shown in Fig. 3.11 are accurate up to $a/h \le 10$, from the convergence of results as sufficiently large number of terms in the infinite series of Eqs. (E6) and (E10) are employed in our numerical calculations. Thus our agreement with Timsit's calculations for $a/h < 0.5$ may be considered as a validation of our series expansion method, and we have extended Timsit's calculations [20] to $a/h = 10$ in Fig. 3.11.

For the special case of $\rho_1/\rho_2 = 1$, the minimum $\overline{R}_c \cong 0.42$ occurs at $a/h \cong 1.6$ [28]. $\overline{R}_c$ is fitted to the following formula for $\rho_1/\rho_2 = 1$ [28],

$$\bar{R}_c \cong \begin{cases} 1.0404 - 2.2328x + 5.0695x^2 - 7.5890x^3 + 6.5898x^4 - 2.9466x^5 + 0.5226x^6, & x = a/h, a/h \le 1.6; \\ 0.4571 - 0.1588y + 0.1742y^2 - 0.0253y^3 + 0.0015y^4, & y = \ln(a/h), 1.6 < a/h < 100. \end{cases}$$

(3.12)

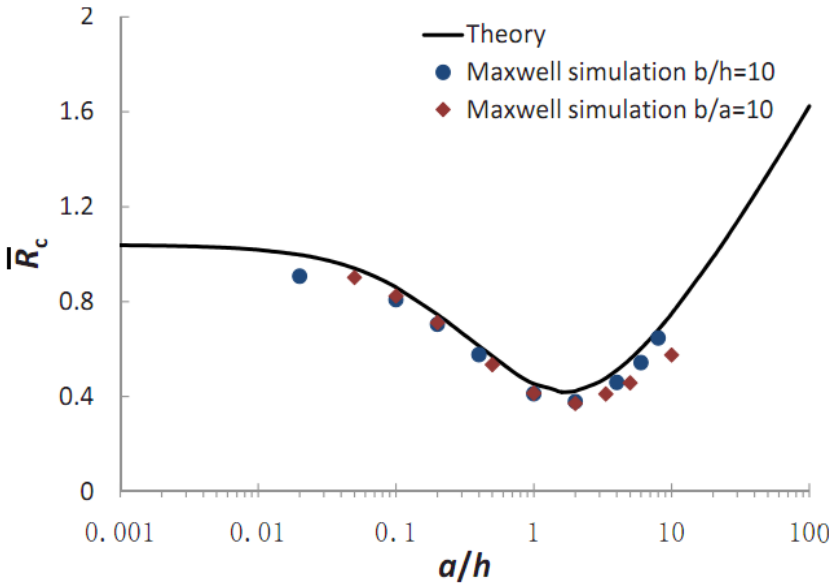

Fig. 3.12 $\bar{R}_c$ as a function of *a*/*h*, for the cylindrical structure in Fig. 3.1 with $\rho_1 = \rho_2 = \rho$. The theoretical result (line) [Eq. (3.12)] is compared to MAXWELL 3D simulation (symbols). In the simulation, we set ρ = 0.001Ωm, L_1 = 10mm, *a* ranging from 0.01 to 4mm with fixed *b* = 10*h* = 5mm, and *h* ranging from 0.1 to 20mm with fixed *b* = 10*a* = 10mm, and a terminal voltage V_0 = 10V was applied. The solid curve in this figure is the same as the green curve (ρ_1/ρ_2 = 1) in Fig. 3.11a.

The theoretical $\bar{R}_c$ in Eq. (3.12) is also spot-checked against MAXWELL 3D code [85] with several combinations of *a*, *h*, and *b*, as shown in Fig. 3.12. Good agreement is noted in general. The discrepancies, e.g., in the leftmost and rightmost data point in Fig. 3.12, are due to the large contrasts in the dimensions (L_1, *b*, *a*, *h*), as well as insufficiently fine meshing of the MAXWELL 3D code, for which the MAXWELL 3D code results are

less accurate.

The vast amount of data collected from the exact calculations allows us to synthesize a simple scaling law for the normalized contact resistance $\overline{R}_c$ in Eq. (3.9) and Fig. 3.11 as, (for $L_2 >> a$ or $L_2 >> h$),

$$\bar{R}_c\left(\frac{a}{h},\frac{\rho_1}{\rho_2}\right)\cong \bar{R}_{c0}\left(\frac{a}{h}\right)+\frac{\Delta\left(\frac{a}{h}\right)}{2}\times\frac{2\rho_1}{\rho_1+\beta\left(\frac{a}{h}\right)\rho_2}, \tag{3.13}$$

$$\bar{R}_{c0}\left(a/h\right)=\bar{R}_c\left(a/h\right)\Big|_{\rho_1/\rho_2\to 0}=\begin{cases}1-2.2968\left(a/h\right)+4.9412\left(a/h\right)^2-6.1773\left(a/h\right)^3\\ +3.811\left(a/h\right)^4-0.8836\left(a/h\right)^5, \quad 0.001\le a/h\le 1;\\ 0.295+0.037\left(h/a\right)+0.0595\left(h/a\right)^2,\ 1<a/h<10,\end{cases} \tag{3.14}$$

$$\Delta\left(a/h\right)=\begin{cases}0.0184\left(a/h\right)^2+0.0073\left(a/h\right)+0.0808, & 0.001\le a/h\le 1;\\ 0.0409x^4-0.1015x^3+0.265x^2-0.0405x+0.1065, & x=\ln(a/h),1<a/h<10,\end{cases}$$
$$\beta\left(a/h\right)=0.0016\left(a/h\right)^2+0.0949\left(a/h\right)+0.6983, \quad 0.001\le a/h<10. \tag{3.15}$$

This scaling law of cylindrical thin film contact resistance, Eq. (3.13), is shown in Fig. 3.13, which compares very well with the exact theory, for the range of $0 < \rho_1/\rho_2 < \infty$ and $0.001 \le a/h < 10$. (We have not found the scaling law for $a/h > 10$ for general values of ρ_1/ρ_2, as explained in the comments following Eq. (3.11).)

While we have not established the scaling laws for $a/h >> 1$ for general values of ρ_1/ρ_2, we did find the scaling laws for $a/h >> 1$ in the two limits $\rho_1/\rho_2 \to \infty$ and $\rho_1/\rho_2 \to 0$:

$$\bar{R}_c \simeq \begin{cases} \dfrac{1}{2\pi}\left(\dfrac{a}{h}\right), & \rho_1/\rho_2 \to \infty; \\ \dfrac{4\ell n2}{\pi^2} = 0.28, & \rho_1/\rho_2 \to 0. \end{cases} \tag{3.15a}$$

These limits are apparent in Fig. 3.11 for $a/h >> 1$. Equation (3.15a) was constructed using similar techniques that we used to derive Eq. (3.3a) for the Cartesian geometry. See also Fig. E1 of Appendix E for the validation of Eq. (3.15a).

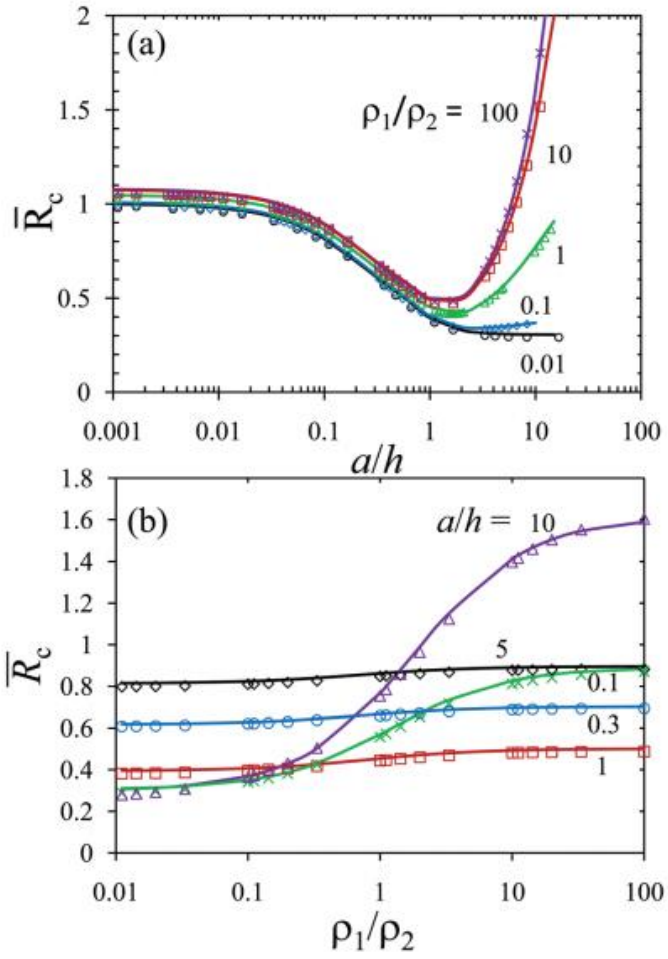

Fig. 3.13 $\bar{R}_c$ for cylindrical thin film structures in Fig. 3.1 and Fig. 3.3, as a function of (a) aspect ratio *a*/*h*, and (b) resistivity ratio ρ_1/ρ_2; symbols for the exact theory [Eq. (E8)], solid lines for the scaling law Eq. (3.13).

Similar to the Cartesian case, the field lines in the thin film region are calculated from Eq. (E1), by numerically solving the field line equation $dz/dr = (\partial\Phi_{\_}/\partial z)/(\partial\Phi_{\_}/\partial r)$. Figure 3.14 shows the field lines in the right half of Region II (Fig. 3.1) for the special case of ρ_1/ρ_2 = 1, with various aspect ratios a/h. It is clear that the field lines are most uniformly distributed over the conduction region when a/h = 1, which is consistent with the smallest normalized contact resistance $\overline{R}_c$ near a/h = 1 for ρ_1/ρ_2 = 1 [Fig. 3.13(a)]. The field lines are horizontally crowded around the corner of the constriction when a/h << 1 [Fig. 3.14(b)], and become vertically crowded around the corner when a/h >>1 [Fig. 3.14(d)], leading to higher contact resistance in both limits, in the same manner as already explained for the Cartesian case. In Fig. 3.15, the field lines are shown for the special case of a/h =1, with various resistivity ratios ρ_1/ρ_2. As ρ_1/ρ_2 increases, Region II becomes more conductive relative to Region I, the interface between Region I and II (i.e. BC in Fig. 3.1) becomes more and more like equipotential, therefore, the field lines (and the current density) at the interface become more uniformly distributed, as shown in Fig. 3.15(c).

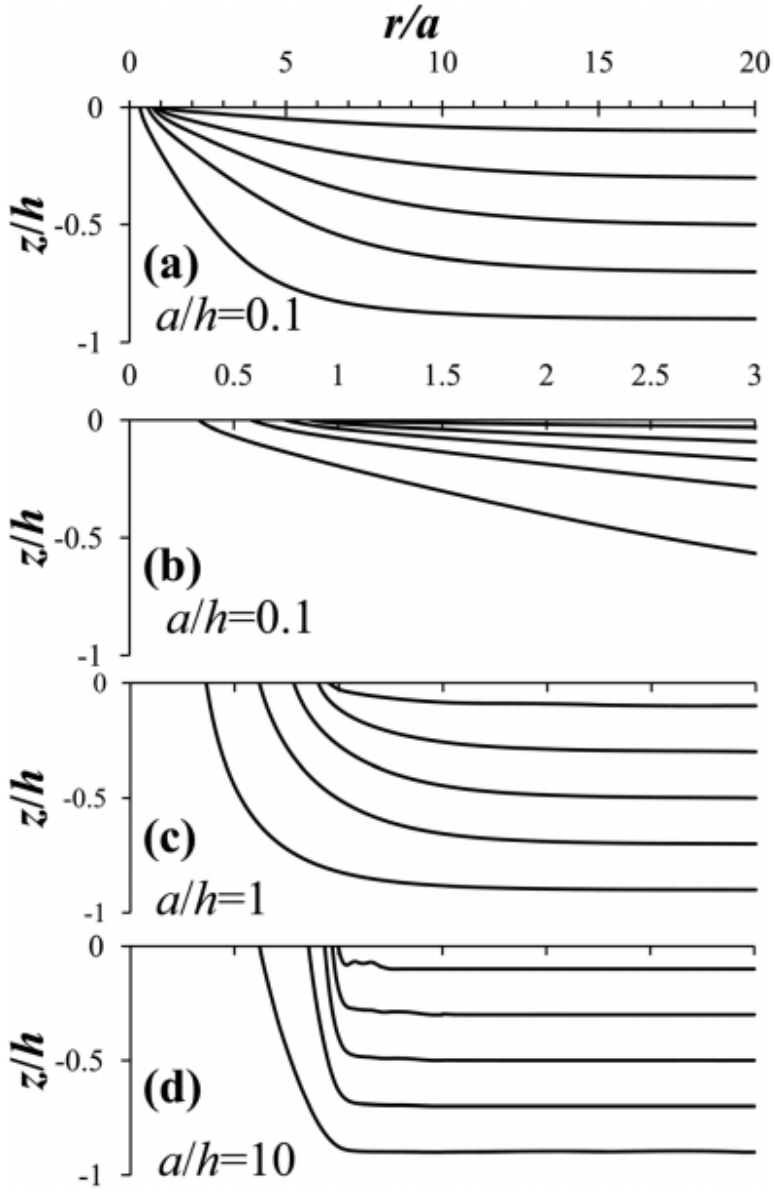

Fig. 3.14 Field lines in the right half of Region II of the cylindrical geometry in Fig. 3.1 for $\rho_1/\rho_2 = 1$ with (a) $a/h = 0.1$, (b) zoom in view of (a) for $0 \leq r/a \leq 3$, (c) $a/h = 1$, and (d) $a/h = 10$.

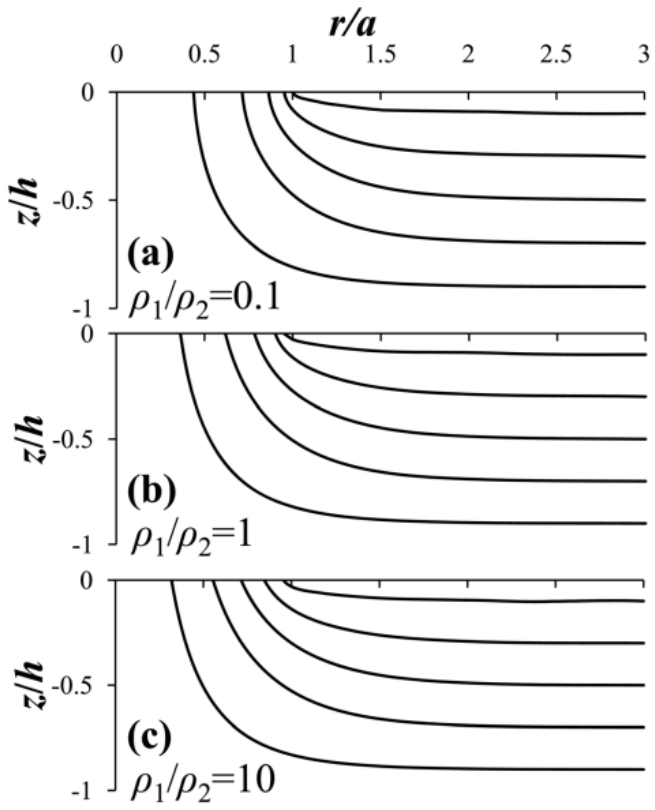

Fig. 3.15 Field lines in the right half of Region II of the cylindrical geometry in Fig. 3.1 for a/h = 1 with (a) ρ_1/ρ_2 = 0.1, (b) ρ_1/ρ_2 = 1, and (c) ρ_1/ρ_2 = 10.

3.4 Thin film spreading resistance as $h \rightarrow 0$ [30]

The $h \rightarrow 0$ limiting case offers substantial insight that lead to interesting generalizations and comparisons to existing experimental method for device characterization [91]; both will be studied in Section 3.5. Here, we first provide an in-depth analysis of an *a*-spot in a thin film contact, shown in Fig. 3.16. Due to symmetry, the *a*-spot area (the constriction interface AB) is an equipotential surface, and all current flow lines are perpendicular to this surface. This is also the situation for the two cases shown in Fig. 3.17, where Fig. 3.17(a) shows an electrode of size *a* being applied directly

to the conducting thin film, and Fig. 3.17(b) shows a post of zero resistivity kept in contact with the thin film with an interface of size a. Thus, the boundary conditions, the potential profile, and therefore the spreading resistance in the thin film region are equivalent in all three geometries shown in Fig. 3.16 and Fig. 3.17, for both Cartesian and cylindrical geometries. Once we know the spreading (or constriction) resistance of any one case, the result will be immediately applicable to the other two cases. Note that Fig. 3.17(b) is a special case of Fig. 3.1, which was treated in detail in Section 3.2 and 3.3.

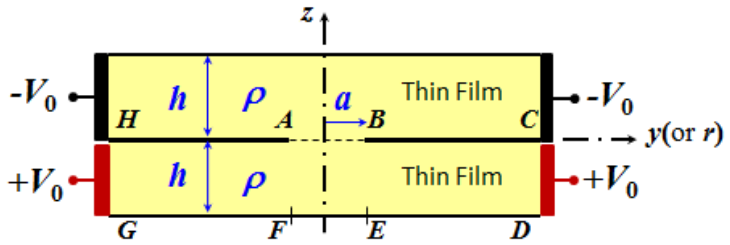

Fig. 3.16 Cylindrical (or Cartesian) electrical contact between two thin films of the same material. The *z*-axis is the axis of rotation for the cylindrical geometry.

We should mention that the spreading resistance for the configuration shown in Fig. 3.17(a) was treated in Refs. [27, 93-97]. In these references, the boundary GD was an equipotential surface (and boundaries GH and CD are electrically insulated) so that the current flow just above GD was *orthogonal* to GD. In contrast, in this chapter, the current flow just above GD is *parallel* to GD, as we impose a constant potential on the boundaries CD and HG [20, 28, 29]. As a result, there is a key difference in the limit $h \to 0$, where the total resistance *vanishes* in Refs. [27, 93-97] as the current path length vanishes, whereas in this chapter, the total resistance becomes *infinite* because the

cross-sectional area of current flow vanishes.

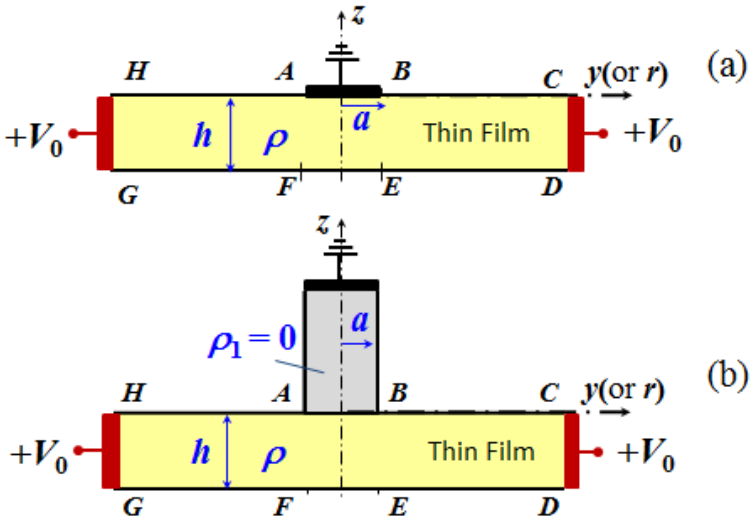

Fig. 3.17 Cylindrical or Cartesian geometries for (a) electrode applied directly on thin film, and (b) region of zero resistivity in contact with thin film. The *z*-axis is the axis of rotation for the cylindrical geometry. For both (a) and (b), the boundary conditions, the potential profile, and therefore the spreading resistance in the thin film are equivalent to that in Fig. 3.16.

3.4.1 Cartesian thin film a-spot

The Cartesian thin film geometry in Fig. 3.17(a) was studied by Hall [16] using conformal mapping calculation. Hall's exact calculation yields the spreading resistance, (cf., Fig. 2 and Eq. (12) of Hall's 1967 paper [16])

$$R_s = \frac{\rho}{4\pi W}\bar{R}_s, \tag{3.16}$$

$$\bar{R}_s = 2\pi\frac{a}{h} - 4\ln\left[\sinh\left(\frac{\pi}{2}\frac{a}{h}\right)\right], \tag{3.17}$$

where W denotes the channel width in the third, ignorable dimension, and the rest of the

symbols have been defined in Fig. 3.16 and Fig. 3.17 [98]. Note that Eq. (3.17) is identical to Eq. (3.3). The normalized thin film spreading resistance, Eq. (3.17), is plotted in Fig. 3.18, which is the same as the lowest curve in Fig. 3.5. The Cartesian thin film geometry in Fig. 3.17(b) has also been calculated by using the series expansion method (cf., Eq. (C8) and Fig. 3.5). In the limit of $\rho_1 \to 0$ in Fig. 3.17 (b) ($\rho_1 = 0.01\rho$ was used in the calculation), Eq. (C8) gives identical results to that of Hall, Eq. (3.17), as shown in Fig. 3.18.

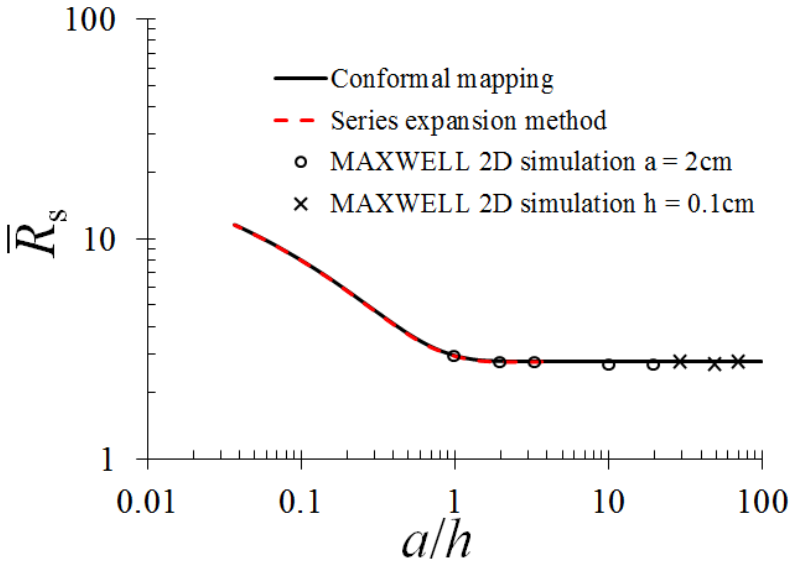

Fig. 3.18 The normalized thin film spreading resistance as a function of *a*/*h*, for the Cartesian structure in Fig. 3.16 and Fig. 3.17. The solid line is for the conformal maping calculations [Eq. (3.17)]. The dashed line, which overlaps with the solid line, is for the series expansion caluclations [cf., Eq. (C8) of Appendix C]. The symbols are for the MAXWELL 2D simulation. Two sets of simulation were performed. The first set (circles) was fixed at a = 2cm, and varying h from 2cm to 0.1cm; the second set (crosses) was fixed at h = 0.1cm, and varying a from 3cm to 7cm.

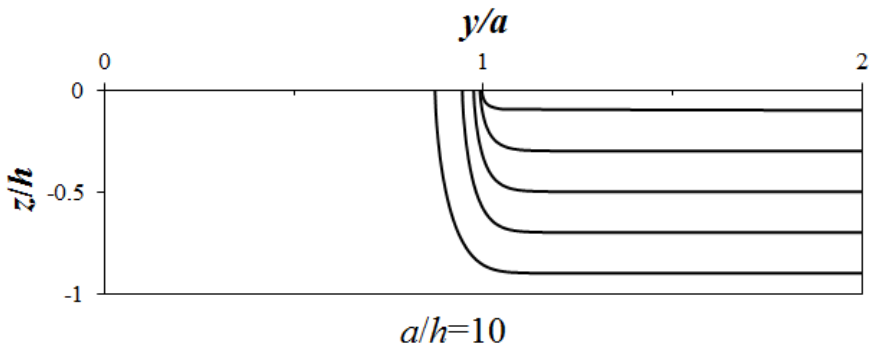

Fig. 3.19 The electric field lines in the right half of the Cartesian thin film in Fig. 3.17, calculated for the case of a/h = 10 and $\rho_1 = 0.01\rho$ [cf. Fig. 3.17(b)]. The crowding of the field lines near the constriction corner could lead to significant local ohmic heating there.

We already proved that [cf. Eq. (3.3a)], in the limit of $a/h \to \infty$, $\overline{R}_s$ converges to the constant minimum value of $4\ell n2 = 2.77$, which is valid for $a/h > 2$, as shown in Fig. 3.18. It is worth noting that the conformal mapping calculation is exact, without any approximation, and is therefore valid for arbitrary values of a and h, even when a and h become arbitrarily small [98]. The field lines in the right half of the Cartesian thin film in Fig. 3.17 are shown in Fig. 3.19. The crowding of the field lines near the constriction corner could lead to significant local ohmic heating there.

To further confirm the *nonzero* limit of $\overline{R}_s = 2.77$ as $h \to 0$ for the Cartesian thin film contact, we performed numerical simulations by using the MAXWELL 2D code [85] for various combinations of parameters on the geometry shown in Fig. 3.17(a). The MAXWELL 2D code results are included in Fig. 3.18 [98]. The finite element method based MAXWELL 2D simulations were performed with great accuracy – the convergence iteration error was controlled to be < 0.002% for each case represented by

the symbols in Fig. 3.18. It is clear that the simulations are in excellent agreement with the analytical calculations, from both conformal mapping and series expansion method.

To probe further into the nonzero limit of $R_s = (4\ln 2)\times(\rho/4\pi W) = 2.77\times(\rho/4\pi W)$ as $h \to 0$, at a finite value of a [Fig. 3.17(a)], let us compute the width a' such that the bulk resistance between $y = a'$ and $y = b$ [98] (and between $y = -a'$ and $y = -b$) is equal to the total resistance R_T as $h \to 0$. Thus, we have, $R_T = \rho(b-a')/2Wh = R_s + R_{bulk} = (4\ell n2)\times(\rho/4\pi W) + \rho(b-a)/2Wh$, yielding

$$a' = a(1-\frac{2\ell n2}{\pi}h/a) = a(1-0.44h/a), \qquad h/a << 1. \tag{3.18}$$

Thus, $a' = 0.956a$ if $h/a = 0.1$, as in Fig. 3.19. That is, the distance between a' and a gives the length scale over which the spreading resistance occurs (Fig. 3.19). Note the possibility of enhanced local heating between a' and a because of the crowding of the field lines there. Such localized enhanced heating has been observed in bulk electrical contacts [12], but its contribution to contact overheating may be greatly magnified in a thin-film contact.

3.4.2 Cylindrical thin film a-spot

The spreading resistance of a thin conducting film for the cylindrical geometry (Fig. 3.16) was analytically calculated by Timsit (cf., Fig. 7 and Eq. (18) of Ref. 20), who approximated the current density distribution through the a-spot of this film with the known current density distribution through the a-spot in a semi-infinite bulk solid [15].

Timsit stated that this approximation is reliable only for $0 < a/h \leq 0.5$ [20] (cf. dashed curve in Fig. 3.20; see also Fig. 3.11). The contact resistance of cylindrical thin film geometry shown in Fig. 3.17(b) was calculated by using the series expansion method in Section 3.3(cf., Eq. (E8) and Fig. 3.11). In the limit of $\rho_1 \rightarrow 0$ in Fig. 3.17(b) ($\rho_1 = 0.01\rho$ was used in the calculation), the series expansion method confirmed Timsit's results for $0 < a/h \leq 0.5$, and at the same time extended his results for a/h up to ten (cf. Fig. 3.11). The results from the exact theory of series expansion were synthesized into a simple, useful polynomial [29, 98] as,

$$R_s = \frac{\rho}{4a}\overline{R}_s, \tag{3.19}$$

$$\overline{R}_s\left(a/h\right) = \begin{cases} 1 - 2.2968\left(a/h\right) + 4.9412\left(a/h\right)^2 - 6.1773\left(a/h\right)^3 \\ +3.811\left(a/h\right)^4 - 0.8836\left(a/h\right)^5, \quad 0.001 \leq a/h \leq 1; \\ 0.295 + 0.037\left(h/a\right) + 0.0595\left(h/a\right)^2, \ 1 < a/h < 10, \end{cases} \tag{3.20}$$

where Eq. (3.20) is Eq. (3.13) with $\rho_1 \rightarrow 0$. The solid curve in Fig. 3.20 plots Eq. (3.20).

For the cylindrical geometry of Fig. 3.16 and Fig. 3.17, accurate calculation from the analytical model of series expansion could only be carried up to $a/h \sim 10$, as seen from Eq. (3.20) and Fig. 3.20. Though limited in range, Fig. 3.20 showed the finite constant value of $\frac{4\ell n2}{\pi^2} = 0.28$ for the normalized thin film spreading resistance as $a/h \rightarrow \infty$, as suggested in Eq. (3.15a). Existence of a similar, nonzero asymptotic limit of $\overline{R}_c = 4\ell n2 = 2.77$ was *proved* for the Cartesian case [Eq. (3.3a)].

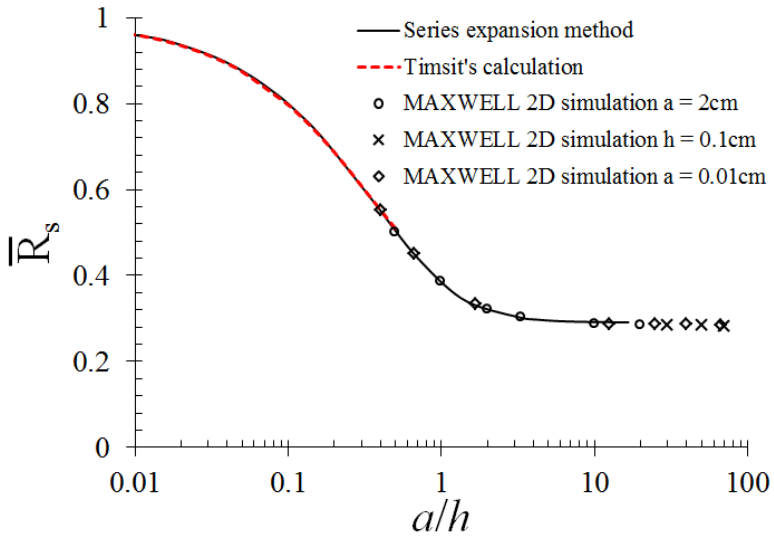

Fig. 3.20 The normalized thin film spreading resistance as a function of *a*/*h*, for the cylindrical structure in Fig. 3.16 and Fig. 3.17. The solid line is for Eq. (3.20), synthesized from the results of series expansion calculations [cf., Eq. (E8)], the dashed line for Tismit's calculations [cf., Eq. (18) of Ref. 20], the symbols for the MAXWELL 2D simulation. Three sets of simulation were performed. The first set was fixed at a = 2cm (circles), and varying h from 2cm to 0.1cm; the second set was fixed at h = 0.1cm (crosses), and varying a from 3cm to 7cm; the third set was fixed at a = 0.01cm (diamonds), and varying h from 0.025cm to 0.00015cm.

To verify the *nonzero* limit of $\overline{R}_s \cong 0.28$ as $h \to 0$ for the cylindrical thin film contact, we performed the MAXWELL 2D simulation [85] for various combinations of parameters on the geometry shown in Fig. 3.17(a). The MAXWELL 2D code results are included in Fig. 3.20 [98]. Similar to the Cartesian case, the simulations were performed with great accuracy – the convergence iteration error was controlled to be < 0.002% for each data point represented by symbols in Fig. 3.20. It is clear from Fig. 3.20 that the simulations are in excellent agreement with the analytical calculations, and again yield the asymptotic constant value of ~ 0.28. The field lines in the right half of the thin film for the cylindrical geometry in Fig. 3.17 are shown in Fig. 3.21. Note the striking

resemblance of field lines in Fig. 3.21 and Fig. 3.19.

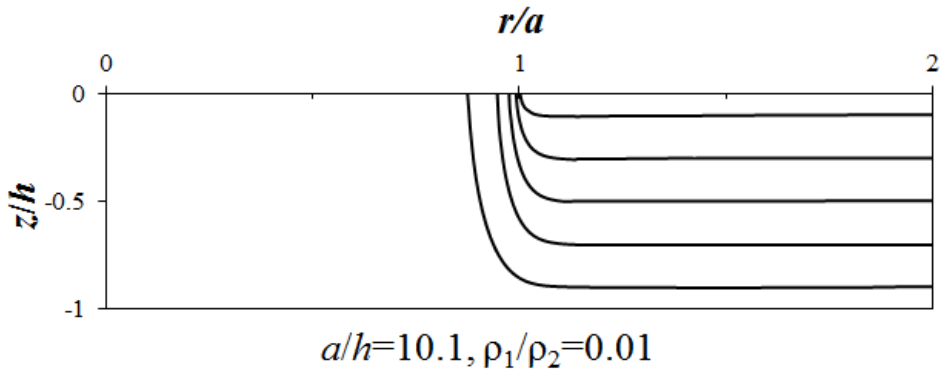

Fig. 3.21 The electric field lines in the right half of the cylindrical thin film in Fig. 3.16 and Fig. 3.17, calculated for the case of a/h = 10.1 and $\rho_1 = 0.01\rho$ [cf. Fig. 3.17(b)]. The field lines shown in this figure is indistinguishable from the field lines shown in Fig. 3.19, the Cartesian case.

To probe further into the nonzero limit of $R_s \cong 0.28\times(\rho/4a)$ as $h \to 0$ at a finite value of a, let us compute the radius a' such that the bulk resistance between $r = a'$ and $r = b$ is equal to the total resistance R_T as $h \to 0$ [Fig. 3.17(a)]. Thus, using the first term in the RHS of Eq. (3.9) for R_{bulk}, we have, $R_T = (\rho/2\pi h)\ell n(b/a') = R_s + R_{bulk} = 0.28\times(\rho/4a) + (\rho/2\pi h)\ell n(b/a)$, yielding†

$$a' = ae^{-0.28\times\frac{\pi}{2}\frac{h}{a}} = ae^{-0.44h/a} \cong a(1-0.44h/a), \qquad h/a << 1 \tag{3.21}$$

which is identical to Eq. (3.18), derived for the Cartesian thin film. Thus, $a' = 0.956a$ if $h/a = 0.1$, as in Fig. 3.21 (and in Fig. 3.19). The distance between a' and a gives the length scale over which the spreading resistance occurs (Fig. 3.21). The nonzero limit of $R_s \cong 0.28\times(\rho/4a)$ as $h \to 0$, at a finite value of a, is equivalent to the resistance of a

† The expression $a' = a\times\exp[-0.28(\pi/2)h/a]$ in Eq. (3.21) was first derived by R. S. Timsit using the MAXWELL 2D data of Fig. 3.20. [Private communication, November 29, 2011]. See also [30].

"residual" circular ring of thickness *h*, and of outer radius *a* and inner radius *a*',

$$R_s = R_{\text{residual circular ring}} = \frac{\rho}{2\pi h}\ell \text{n}\left(\frac{a}{a'}\right) = \frac{\rho}{2\pi h}\ell \text{n}\left(\frac{1}{1-0.44h/a}\right) \cong 0.28\times\frac{\rho}{4a}, \quad h \to 0, \tag{3.22}$$

where Eq. (3.21) and the first term in the RHS of Eq. (3.9) have been used. As seen from Eq. (3.22), as *h* decreases to zero, the resistance of the "residual" circular ring region (over which the spreading resistance occurs) remains a constant, and this might be considered as an interpretation of the *nonzero* limit of the spreading resistance $R_s \cong 0.28\times(\rho/4a)$ as $h \to 0$ for the cylindrical case [30].

A similar argument may be made for the Cartesian case as Eqs. (3.21) and (3.18) are identical. The distance between *a* and *a*' remains to be 0.44*h*, and Eq. (3.22) is modified to read

$$R_s = R_{\text{residual rectangular strips}} = \frac{\rho(a-a')}{2hW} = \frac{\rho\times 0.44h}{2hW} = \frac{\rho}{4\pi W}\times 2.77, \quad h \to 0. \tag{3.23}$$

Once *a* is fixed, in the limit $h \to 0$, the edge "B" in Fig. 3.17(a) looks the same whether it is a circular arc (cylindrical geometry) or a straight line segment pointing out of the paper (Cartesian geometry), as far as the current flow patterns at *B* are concerned. This is why the factor 0.44 appears in both Eqs. (3.18) and (3.21), and Fig. 3.19 and Fig. 3.21 look identical. Since $0.28 = (4\ell n2)/\pi^2$, we establish that the asymptotic value for the cylindrical thin film spreading resistance is $\overline{R}_s = (4\ell n2)/\pi^2 = 2.77/\pi^2 = 0.28$ as $h \to 0$. The ratio between the "hard limits" of $\overline{R}_s$ for the Cartesian and cylindrical thin film is π^2 as $h \to 0$. [cf. Eqs. (3.3a) and (3.15a)]

Finally, even though R_s approaches a finite constant as $h \to 0$, R_s/R_T approaches to zero since $R_{bulk,}$ and therefore, R_T approaches infinity. That is, the spreading resistance contributes to a negligible *fraction* of the total resistance in the limit $h \to 0$. The latter property was also shared in Refs. [27, 93, 94, 95, 96, 97], even though in these references, both the total resistance and the spreading resistance vanish as $h \to 0$.

3.5 Generalizations

The insight obtained in the $h \to 0$ limit allows two important generalizations of the theory: an *a*-spot of arbitrary shape (Section 3.5.1) and high frequency limit (Section 3.5.2). In Section 3.5.3, we comment on the transfer length and include comparison of our model with the transfer length method (TLM) [91] that was used extensively in experimental characterization of thin film semiconductor devices.

3.5.1 Extension to a-spot of arbitrary shape [30]

Since the distance between *a* and *a*' is *always* 0.44*h* as $h \to 0$ [cf., Eqs. (3.18) and (3.21)], and Fig. 3.19 and Fig. 3.21 are identical for both cylindrical and Cartesian *a*-spot shown in Fig. 3.16, the conclusions in Section 3.4.2 could perhaps be extended to an *a*-spot of an arbitrary shape in the $h \to 0$ limit, as shown in Fig. 3.22. Specifically, we propose that the spreading resistance R_s would assume the general form,

$$R_s = \left(\frac{\rho}{L}\right)\frac{2\ell n2}{\pi}, \quad h \to 0, \tag{3.24}$$

where L is the circumference of the a-spot of an arbitrary shape, and R_{bulk} is the bulk resistance of the thin film exterior to this generalized a-spot. For a circular a-spot of radius a, $L = 2\pi a$, and Eq. (3.24) reproduces Eq. (3.22). For an a-spot in the Cartesian geometry, $L = 2W$ (the factor of two to account for both edges A and B in Fig. 3.16), and Eq. (3.24) reproduces Eq. (3.23).

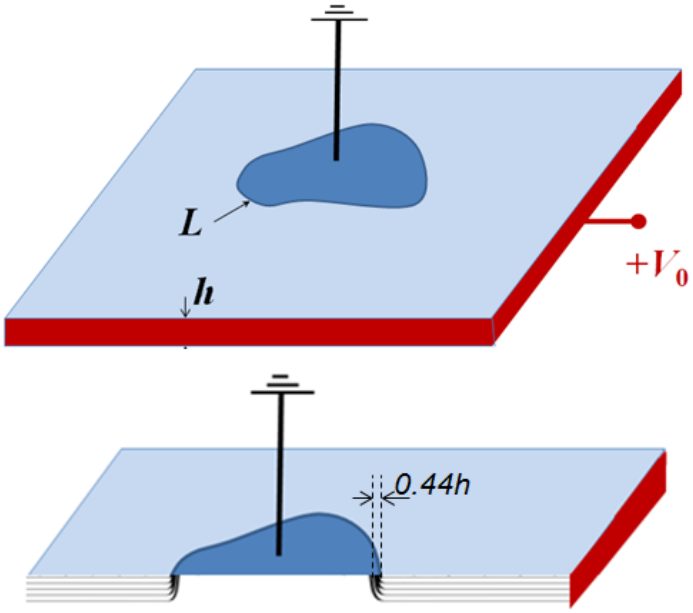

Fig. 3.22 a-spot of an arbitrary shape. Note the current flow lines in the bottom figure are identical to Fig. 3.21 and Fig. 3.19 locally.

3.5.2 Extension to AC case

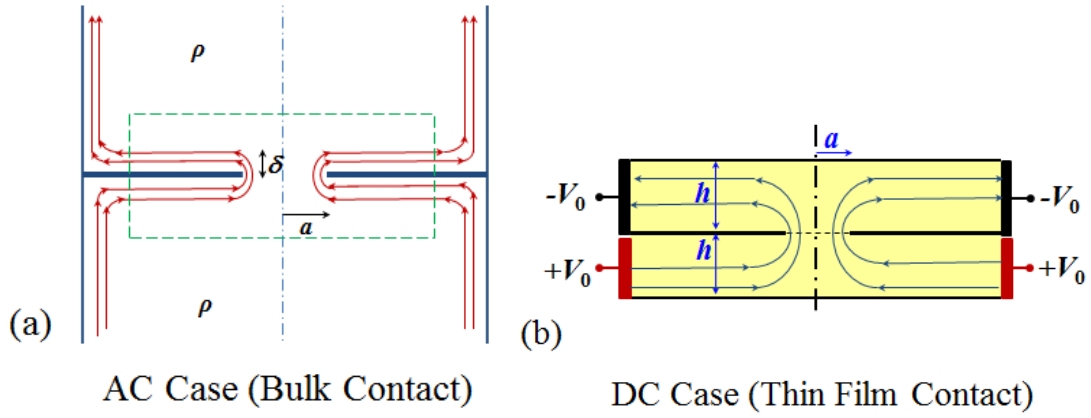

Fig. 3.23 (a) High-frequency AC current in a bulk solid with constriction of size *a* where the current flow is limited to the skin depth δ [20,99], and (b) The DC thin film contact [30] analyzed in this section (Fig. 3.16).

Timsit pointed out that the DC spreading resistance in a thin film is comparable to the spreading resistance for high-frequency AC current in a bulk solid where the current flow is limited to the skin depth [20, 99], if the thickness of the equivalent thin film is identified as the skin depth, δ, at the relevant frequency, i.e., $h = \delta$, as shown in Fig. 3.23(a). Comparing with Fig. 3.23(b), we note the analogy between the region in the dashed box for the AC case and the DC thin film case studied in this thesis. Along this line, we speculate that the same finite limits of $\overline{R}_s = 2.77$ for the Cartesian case and $\overline{R}_s = 0.28$ for the cylindrical case, would apply to the AC case as the skin depth $\delta \to 0$. In fact, Figure 9 of Ref. [20] for the 1GHz curve is about 0.3 of that for the cylindrical DC curve, for all constriction diameters shown in that figure, which is reproduced in Fig.

3.24. If the frequency further increases, we expect the ratio would be ~ 0.28. Likewise, we conjecture that Fig. 10 of [20], which is reproduced in Fig. 3.25, would converge to the final value of ~ 0.28 as $a/\delta \to \infty$. The blue solid curve of Fig. 3.25 is a plot of Eq. (3.20).

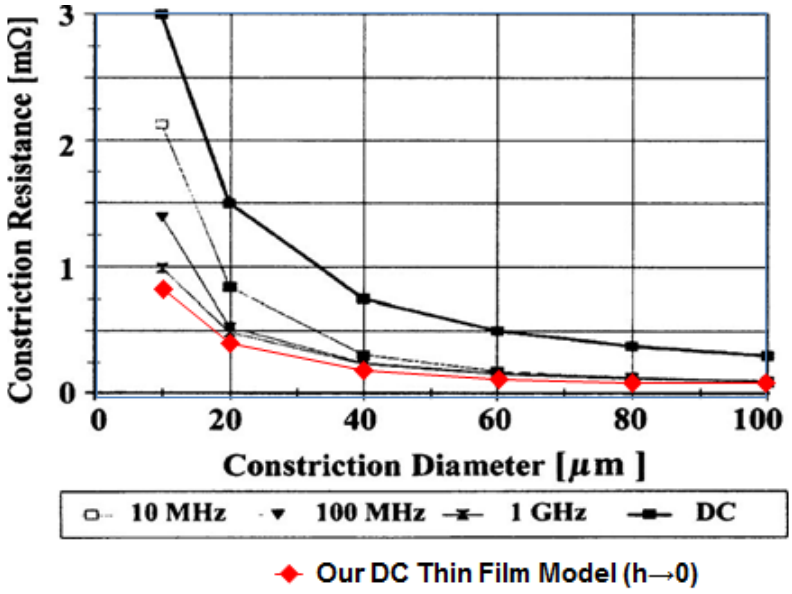

Fig. 3.24 The DC thin film model ($h \to 0$) studied in this thesis may be considered as the limiting case for the high frequency AC bulk contact resistance [20, 99], once the skin depth δ for the AC bulk contact is identified with the thin film thickness h.

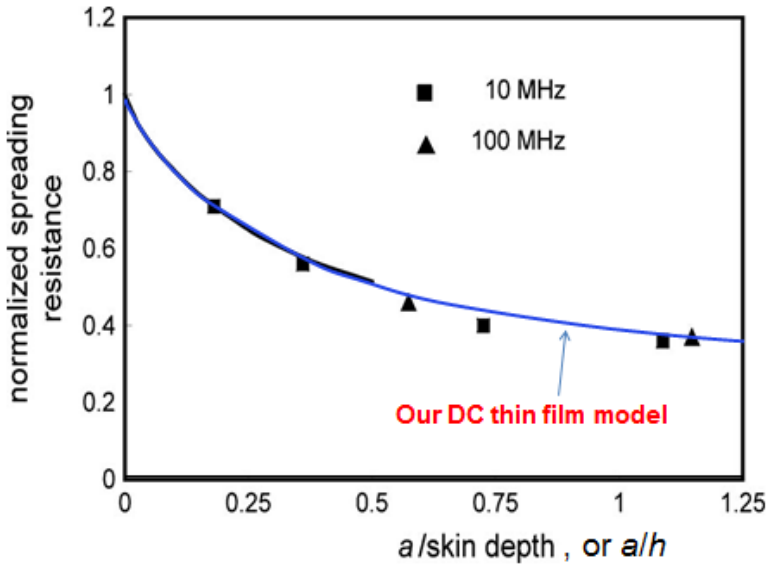

Fig. 3.25 Comparison of the DC thin film model studied in this thesis with the AC bulk contact resistance [20]. As $a/\delta \to \infty$, we expect the curve would converge to a final value of 0.28, as predicted by our DC thin film model [Eq.(3.20) and Fig. 3.20].

3.5.3 Transfer Lengths and Comparison with Experiment Method

In semiconductor device and material characterization, one important parameter about electrical contacts is the transfer length, L_T, which is defined as the length scale over which most of the current from a contact into a semiconductor thin film flows [91, 100]. The simple transmission line model (TLM) is widely employed to characterize the metal-semiconductor contacts [91, 100].

From Eq. (3.18) and Fig. 3.19, one may argue that the transfer length $L_T \sim 0.44h$ for the present Cartesian thin film model, and this transfer length is due only to the fringing fields. In the transmission line model [91], there is another component of transfer length, neglecting the fringing fields, that is approximately given by, $L_{T2} = (r_c/R_{sh})^{1/2}$, where $R_{sh} = \rho/h$ is the sheet resistance (in Ω/square) in the semiconductor thin film under

the contact, and r_c = contact resistivity (in Ωm^2). The resistivity r_c arises from the metal-semiconductor barrier so that in this chapter we would have $r_c = 0$, yielding $L_{T2} = 0$ in the conventional transmission line model [91]. The transmission line model does not include the effect of fringing fields studied in this chapter.

Experimentally, the transfer length method [91] (also denoted as TLM, which should be distinguished from the Transmission Line Model), has been extensively used to characterize the metal-semiconductor contact resistance. A typical transfer length method test structure and a plot of total resistance as a function of contact spacing, d, is shown in Fig. 3.26.

For contact size exceeding $1.5L_T$ in Fig. 3.26, the total resistance between any two contacts (two darkened regions) is found to be [Eq. (3.30) of Ref. 91],

$$R_T = R_{bulk} + 2R_c \approx \frac{R_{sh}}{Z} d + 2\frac{R_{sh} L_T}{Z}, \tag{3.25}$$

where R_{sh} is the sheet resistance (in Ω/square), R_c is the contact resistance, and L_T is the transfer length, and all the other symbols are defined in Fig. 3.26. The total resistance is measured for various contact spacings d_1, d_2, d_3, …, and R_T is plotted as a function of d. Three parameters are extracted from such a plot. The slope R_{sh}/d leads to the sheet resistance. The intercept at $d = 0$ is $R_T = 2R_c$ giving the contact resistance. The intercept at $R_T = 0$ gives $-d = -2L_T$, which in turn is used to calculate the specific contact resistivity.

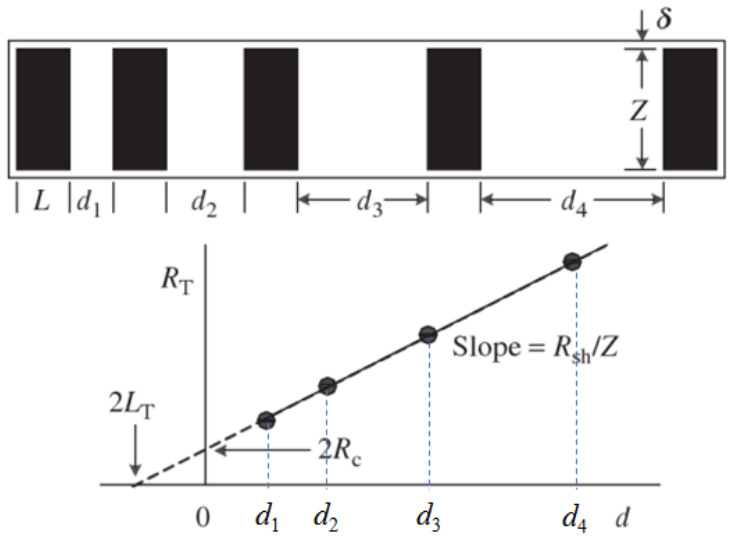

Fig. 3.26 A transfer length method test structure and a plot of total resistance as a function of contact spacing, *d*. [Fig. 3.22 of Ref. 91]

For contact size exceeding $1.5L_T$ in Fig. 3.26, the contact size is usually much larger than the thin film thickness h, thus, the results obtained for the limit $h \to 0$ in Section 3.4.1 remain valid, giving a contact resistance

$$R_c = 2R_s = 2\times\left(\frac{\rho}{4\pi Z}\times 2.77\right), \quad h \to 0, \tag{3.26}$$

where Z is the contact width in Fig. 3.26 (=W in Eq. (3.23)), and the factor 2 counts for the fact that only half of the contact under test is active, (i.e. equivalent to half of the geometry in Fig. 3.17 (a)). Putting Eq. (3.26) into Eq. (3.25) and using $R_{sh} = \rho/h$, we have

$$L_T = \frac{2.77}{2\pi}h \cong 0.44h, \quad h \to 0, \tag{3.27}$$

which gives the same result as that from our observation, stated in the beginning of the second paragraph of this subsection. This analysis implies that there are *intrinsic errors* in extracting the specific contact resistivity from the transfer length measured from the

transfer length method. The errors are due to the effect of fringing fields studied in this chapter.

3.6 Concluding remarks

This chapter presents accurate analytic models which allow ready evaluation of the contact resistance or constriction resistance of thin film contacts with dissimilar materials over a large range of parameter space. We show the large distortions of the field lines as a result of a small film thickness, implying strong local heating. The models assume arbitrary aspect ratios, and arbitrary resistivity ratios in the different regions for both Cartesian and cylindrical geometries. From the large parameter space surveyed, it is found that, at a given resistivity ratio, the thin film contact resistance primarily depends only on the ratio of constriction size (a) to the film thickness (h), as long as either $L_2 >> a$ or $L_2 >> h$. In the latter cases, the electrostatic fringe field is restricted to the constriction corner only, and becomes insensitive to the location of terminals for the thin film region.

The effects of dissimilar materials are summarized as follows. If the constriction size (a) is small compared to the film thickness (h), the thin film contact resistance is insensitive to the resistivity ratio. However, if $a/h > 1$, the contact resistance varies significantly with the resistivity ratio. Typically the minimum contact resistance is realized with $a/h \sim 1$, for both Cartesian and cylindrical cases. Various limiting cases are studied and validated with known results. Accurate analytical scaling laws are presented.

We also found that the normalized thin film spreading resistance converges to the finite values, 2.77 for Cartesian and 0.28 for cylindrical case in the limit $h \to 0$. An interpretation of these asymptotic limits is given. We conjecture that the same finite limits of normalized thin film spreading resistance would apply to the *a*-spot between bulk solids in the AC case as the skin depth $\delta \to 0$, if the thickness of the equivalent thin film is identified as the skin depth at the relevant frequency, i.e., $h = \delta$. Extension to a general *a*-spot geometry is attempted. We estimate that the transfer length $L_T \sim 0.44h$ for the present Cartesian thin film model, in contrast to the result $L_T = 0$ from the conventional transmission line model [91]. The transmission line model does not include the effect of fringing fields studied in this chapter.

Finally, one may adapt the results for the DC case in this chapter to the steady state heat flow in thermally insulated thin film structures with dissimilar thermal properties. This may be done by replacing the electrical conductivity ($1/\rho_j$) with the thermal conductivity (κ_j), j = 1, 2, in the different regions, assuming that the κ_j's are independent of temperature.

CHAPTER 4

SURFACE ROUGHNESS INDUCED ENHANCED RF ABSORPTION AND FIELD ENHANCEMENTS

4.1 Introduction

Surface roughness may exert a profound effect in the performance of radio-frequency (RF) cavities or slow wave structures [53-65], for example, in communication systems [54-56], particle accelerators [57-59, 65-69], and material characterization at microwave frequencies [70,71], etc. Surface roughness may cause enhanced power absorption in these devices [62-65, 72-74]. It may lead to excessive local electric field enhancement that could trigger RF breakdown [56, 74-76]. In a superconducting cavity, surface roughness may also cause local magnetic field enhancement that leads to abrupt quenching [53, 57, 58], i.e., rapid loss of superconductivity.

Surface roughness may assume many forms. Small foreign objects might be attached to the cavity surface, and these impurities might have very different electrical properties from those of the presumably pristine metallic surface. Their presence is

known to cause localized damage [10, 62, 66, 67]. The metallic surface itself might not be perfectly smooth, in which case the roughness consists of the same material as the surface, i.e., no foreign materials are involved. Grain boundaries also make the surface microscopically rough [73, 101, 101]. Regardless of the origin of the roughness, of general interest is the additional RF power that would be absorbed due to the surface roughness, and the local enhancement in the RF electric field and in the RF magnetic field due to the change of the local geometry.

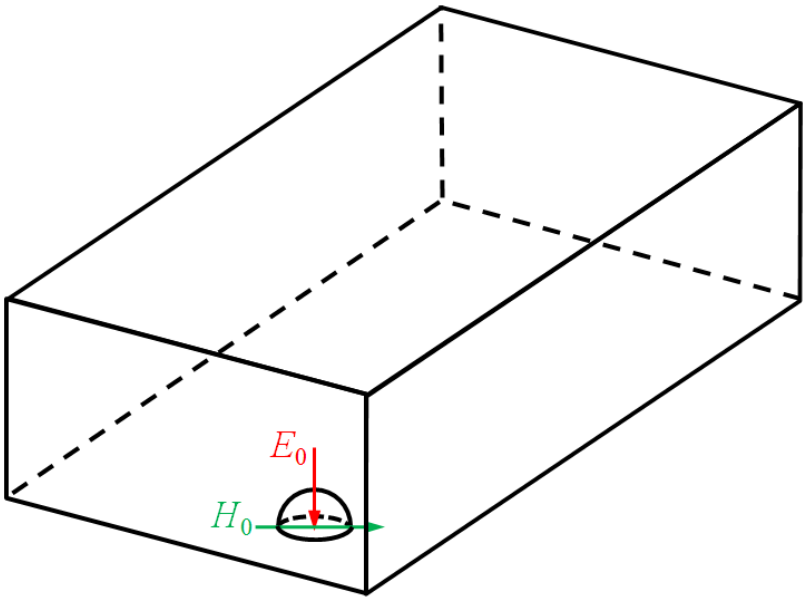

Fig. 4.1 A small hemispherical bump on a conducting surface whose local RF electric field is E_0 and local RF magnetic field H_0 in the absence of the bump.

In this chapter, we provide an accurate assessment of the additional heating, as well as the local RF electric field and RF magnetic field enhancements due to a small, local surface roughness [11]. The crucial assumption is that this small roughness is

hemispherical in shape, whose radius, a, is much less than λ ($a/\lambda << 1$), where λ is the RF wavelength exterior to the protrusion. To isolate the effects of this roughness, we assume that it is setting on a perfectly conducting surface so that in the absence of this roughness, the RF electric field there, $\mathbf{E_0}$, is orthogonal to the surface; whereas the RF magnetic field there, $\mathbf{H_0}$, is tangential to the surface (Fig. 4.1). The relative magnitudes and the relative phases between $\mathbf{E_0}$ and $\mathbf{H_0}$ may be arbitrary so that this local roughness may be located anywhere on the surface of a conducting cavity or of a conducting waveguide. Another crucial assumption is that the hemispherical protrusion has a constant (complex) permittivity, $\varepsilon_1 = \varepsilon_{r1} - j\sigma/\omega$, where σ is the electrical conductivity at the RF frequency ω, and a constant (real) permeability, μ_1. While ε_{r1}, σ, and μ_1 are real constants, all assumed to be known, their values may be arbitrary. Thus, this roughness may represent a foreign object, or it may be made of the same material as the conducting surface. The ratio δ/a may take on an arbitrary value ranging from zero to infinity, where $\delta = (2/\omega\mu_0\sigma)^{1/2}$ is the skin depth associated with protrusion material, with $\delta \to \infty$ corresponding to an insulating protrusion and $\delta = 0$ corresponding to a perfectly conducting protrusion.

In Section 4.2, we transform the irregular geometry of a "hemispherical protrusion on a surface" (Fig. 4.1) into an equivalent, but highly symmetrical problem of a "spherical particulate in a spherical cavity" (Fig. 4.3 below) under the assumption that the radius a of the protrusion is much smaller than the wavelength (and also much smaller than the local radius of curvature of the surface if the cavity wall is not a flat surface).

The perturbation by the small spherical particulate on the eigenfrequency of the spherical cavity then gives the RF power absorbed by the protrusion, as treated in Section 4.3. The enhancement factors of the RF fields, as a result of the protrusion, are presented in Section 4.4. They are obtained from the perturbation on the eigenfunctions of the spherical cavity by the spherical particulate. Both RF electric field and RF magnetic field enhancement factors reduce to the established results in the appropriate limits. Section 4.4 also presents spot checks of the field enhancement factors against the Maxwell 3-D code [85] results, adding plausibility of our approach. Concluding remarks are given in Section 4.5.

Since the perturbations on the eigenmodes on the spherical cavity, by a small spherical particulate, were treated in detail by Bosman *et al*. [10, 102] and by Tang *et al*. [103], we shall only quote their results when needed. Furthermore, Refs. [102] and [103] focused mainly on the RF heating of an isolated, freely suspended particulate; this paper extends their results to include the field enhancement factors in the RF electric field and RF magnetic field, and the resultant RF heating, for the important case where a small hemispherical particulate is attached to a perfect conductor.

4.2 The model

Despite the irregular geometry shown Fig. 4.1, and the possibly strong coupling between the RF magnetic field and the RF electric field through the hemispherical

protrusion, the problems of RF heating and of RF field enhancement at the protrusion can actually be solved *analytically* in the asymptotic limit $a/\lambda << 1$, without any restriction on the skin depth, δ. Our argument follows. In the *immediate neighborhood* of the protrusion (Fig. 4.1), the RF electromagnetic field, represented as ($\mathbf{E_0}$, $\mathbf{H_0}$) when the protrusion is absent, may be considered as a linear combination of two modes: ($\mathbf{E_0}$, $\mathbf{0}$) and ($\mathbf{0}$, $\mathbf{H_0}$), each oscillating at the same frequency ω (Fig. 4.2). Because of the respective domination of the RF electric field and the RF magnetic field, we designate the ($\mathbf{E_0}$, $\mathbf{0}$) mode as the TE mode, and the ($\mathbf{0}$, $\mathbf{H_0}$) as the TM mode. This mode designation, together with the corresponding ones in Fig. 4.3, follows Ref. [103]. As we shall see, it also applies to incident TEM plane wave in an open system with protrusions.

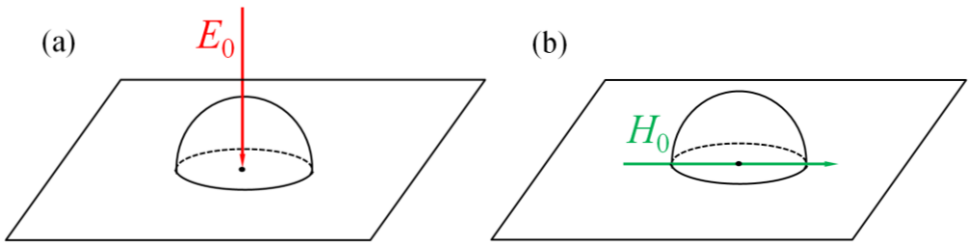

Fig. 4.2 Decomposition of the local electromagnetic field ($\mathbf{E_0}$, $\mathbf{H_0}$) into (a) the TE mode ($\mathbf{E_0}$, $\mathbf{0}$), and (b) the TM mode ($\mathbf{0}$, $\mathbf{H_0}$).

For the action of ($\mathbf{E_0}$, $\mathbf{0}$) on a small hemispherical protrusion [Fig. 4.2(a)], we now consider an auxiliary problem [Fig. 4.3(a)]. Figure 4.3(a) shows a perfectly conducting spherical cavity of radius b, whose natural frequency for the fundamental TE mode is ω when this cavity is empty (i.e., by setting $b = 2.7437c/\omega$), and whose vacuum eigenmode at the center of cavity is ($\mathbf{E_0}$, $\mathbf{0}$). We now insert a spherical particulate of radius a and of

the same permittivity $\varepsilon_1 = \varepsilon_{r1} - j\sigma/\omega$, and the same permeability μ_1 at the center of this spherical cavity [Fig. 4.3(a)]. The high degree of spherical symmetry allows us to analytically calculate the perturbation on the eigenmode and the perturbation on the eigenfrequency by this spherical particulate [102, 103].

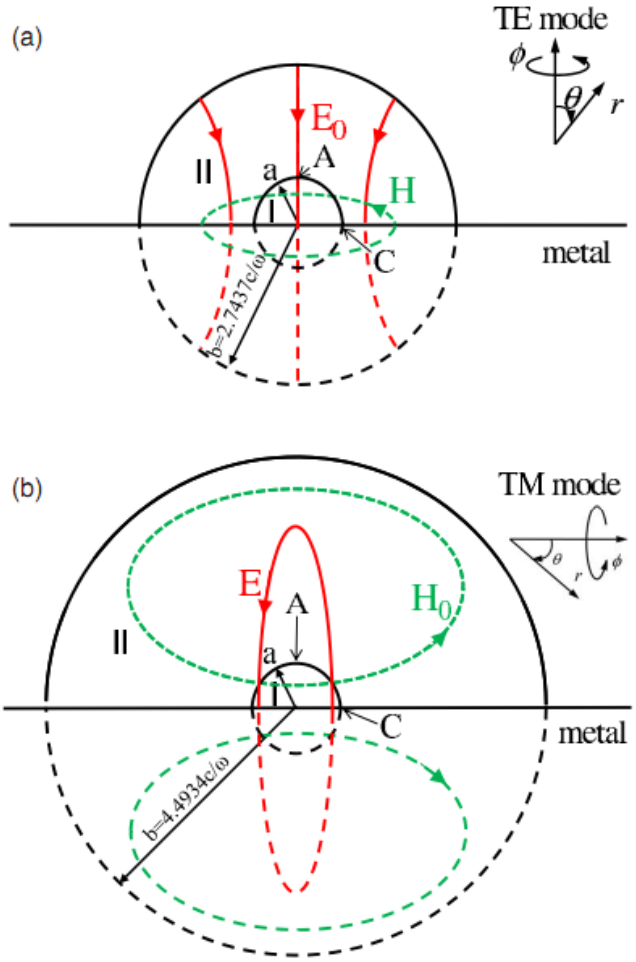

Fig. 4.3 Transformation of the "protrusion on surface" problem into a spherical eigenmode problem for (a) the TE_{110} mode and (b) the TM_{110} mode. The mode index (110) refers to variations in *r*, θ, and φ. Note that, by symmetry, the mode patterns in (a) or (b) are unchanged with or without a perfect conductor inserted in the horizontal mid-plane.

The perturbation on the TE eigenmode gives the RF electric field enhancement

factor, and the damping rate of the TE eigenmode gives the RF power dissipated in the lossy particulate [102, 103]. These are also precisely the RF electric field enhancement for the small hemispherical protrusion on the flat plate [Fig. 4.2(a)] and the RF electric field energy that the (lossy) protrusion dissipated. This follows from symmetry of the fields: the RF electric field and the (vanishingly small) RF magnetic field in the spherical cavity, including the spherical particulate, are unchanged if we insert a horizontal, perfectly conducting plate that cuts the spherical cavity and spherical particulate in half [Fig. 4.3(a)]. In the immediate vicinity of the protrusion, the geometry, and RF field configuration also, between Fig. 4.2(a) and Fig. 4.3(a) are then equivalent in the asymptotic limit $a/\lambda << 1$. Since the perturbed TE eigenmode have been solved using the full set of the Maxwell equations for Fig. 4.3(a), with the inclusion of the particulate, the calculation of the RF electromagnetic field for the TE mode is intrinsically self-consistent [102, 103].

Similarly, for the action of ($\mathbf{0}$, $\mathbf{H_0}$) on the hemispherical protrusion [Fig. 4.2(b)], we also consider the auxiliary problem [Fig. 4.3(b)], that of a perfectly conducting spherical cavity, whose natural frequency for the fundamental TM mode is also ω when the cavity is empty (i.e., by setting the cavity radius $b = 4.4934c/\omega$), and whose vacuum eigenmode at the center of cavity is ($\mathbf{0}$, $\mathbf{H_0}$). We insert the same spherical particulate, of radius a and of the same permittivity $\varepsilon_1 = \varepsilon_{r1} - j\sigma/\omega$, and the same permeability μ_1 at the center of this spherical cavity [Fig. 4.3(b)]. The perturbation on the TM eigenmode gives the RF magnetic field enhancement factor, and the damping rate of the TM eigenmode gives the

RF power dissipated for the lossy particulate [102, 103]. These are also precisely the RF magnetic field enhancement for the small hemispherical protrusion on the flat plate and the RF magnetic field energy that the (lossy) protrusion dissipated. This follows from symmetry of the fields: the RF magnetic field and the (vanishingly small) RF electric field in the spherical cavity, including the spherical particulate, are unchanged if we insert a horizontal, perfectly conducting plate that cuts the spherical cavity and spherical particulate in half [Fig. 4.3(b)]. In the immediate vicinity of the protrusion, the geometry, and RF field configuration also, between Fig. 4.2(b) and Fig. 4.3(b) are then equivalent in the asymptotic limit $a/\lambda << 1$. Since the perturbed TM eigenmode has been solved using the full set of the Maxwell equations, with the inclusion of the particulate, the calculation of the RF electromagnetic field for the TM mode is intrinsically self-consistent.

4.3 RF power absorption

The perturbation due to a small particulate located at the center of a perfectly conducting spherical cavity is studied by Bosman *et al.*[102] and Tang *et al.*[103]. The particulate has radius a and the cavity has radius b. Hereafter, we follow Tang *et al.* [103] to use subscripts 1 and 2 to denote the values in region I ($r < a$) and region II ($a < r < b$) (Fig. 4.3). In these two regions, the permittivity is, respectively, $\varepsilon_1 = \varepsilon_{r1} - j\sigma/\omega$, and ε_2; and the permeability is, respectively, μ_1 and μ_2, where ε_{r1}, σ, ε_2, μ_1 and μ_2 are all real and they may assume arbitrary values. Even though in this chapter, we will set $\varepsilon_2 = \varepsilon_0$ and μ_2

= μ_0 the formulas will be written for general values of ε_2, and μ_2 to conform with the notation of [103]. In the absence of this particulate, the cavity admits the fundamental TE_{110} mode, which has a maximum RF electric field, and a null RF magnetic field, at the center [Fig. 4.3(a)], as well as the TM_{110} mode, which has a maximum RF magnetic field, and a null RF electric field, at the center [Fig. 4.3(b)]. In the empty cavity, both the TE mode and TM mode have an infinite quality factor Q since the cavity wall is lossless. The eigenfrequencies ω_E and ω_M (both equal to ω) for the TE_{110} and TM_{110} modes are given by $\eta_E = 2.74371$ and $\eta_M = 4.4934$, respectively, with $\eta_{E,M} = \omega_{E,M} b(\varepsilon_2 \mu_2)^{1/2} = 2\pi b/\lambda$ [104]. When a small, lossy particulate is introduced at the center of the cavity, the modes would be slightly damped, the eigenmode frequency becomes complex, and the quality factor Q becomes finite. The change of Q in the TE (TM) mode gives the power dissipation due to this lossy particulate by the RF electric (magnetic) field. The change in the eigenfrequencies, $\delta\omega$, which is complex in general, due to the particulate reads,

$$\frac{\delta\omega}{\omega_E} = \frac{\delta\eta}{\eta_E} \approx \frac{Y'(\eta_E)}{\eta_E J''(\eta_E)} \left[\frac{J(\xi_{2E})}{Y(\xi_{2E})}\right] \left[\frac{Z_1 A(\xi_{1E}) - A(\xi_{2E})}{Z_1 A(\xi_{1E}) - B(\xi_{2E})}\right], \qquad \text{(TE mode)} \qquad (4.1)$$

$$\frac{\delta\omega}{\omega_M} = \frac{\delta\eta}{\eta_M} \approx \frac{y(\eta_M)}{\eta_M j'(\eta_M)} \left[\frac{J'(\xi_{2M})}{Y'(\xi_{2M})}\right] \left[\frac{Z_1 / A(\xi_{1M}) - 1/A(\xi_{2M})}{Z_1 / A(\xi_{1M}) - 1/B(\xi_{2M})}\right], \quad \text{(TM mode)} \qquad (4.2)$$

for the TE and TM modes respectively [cf. Eqs. (15) and (28) of Ref. 103], where

$$j(\xi) = \frac{\sin\xi}{\xi^2} - \frac{\cos\xi}{\xi}, \qquad (4.3)$$

$$y(\xi) = -\frac{\cos\xi}{\xi^2} - \frac{\sin\xi}{\xi}, \qquad (4.4)$$

$$J(\xi) = \xi j(\xi), \;\; Y(\xi) = \xi y(\xi), \qquad (4.5)$$

$$A(\xi)=\frac{J'(\xi)}{J(\xi)},\quad B(\xi)=\frac{Y'(\xi)}{Y(\xi)}, \tag{4.6}$$

$$Z_1=\frac{\sqrt{\mu_1/\mu_2}}{\sqrt{\varepsilon_1/\varepsilon_2}}, \tag{4.7}$$

and the prime denotes the derivative with respect to the argument. In the arguments, ξ_{2E} = $\eta_E(a/b)$ and ξ_{2M} = $\eta_M(a/b)$ are both real, $\xi_{1E}=\omega_E(\varepsilon_1\mu_1)^{1/2}a$, $\xi_{1M}=\omega_M(\varepsilon_1\mu_1)^{1/2}a$, in which μ_1 (permeability of region I) is real, $\varepsilon_1=\varepsilon_{1r}-j\sigma/\omega$ (permittivity of region I) is complex. Once more, Eqs. (4.1) and (4.2) are valid as long as a/λ << 1, regardless of the values of ε_{r1},σ, ε_2, μ_1 and μ_2 .

The real parts of Eqs. (4.1) and (4.2) give the detune of the eigenmode frequency and the imaginary parts give the damping rate $\gamma_{E,M}$, which is related to the average power loss P and the quality factor Q through the relationship (Ref. [104], p. 258),

$$P=2\gamma U=\omega U/Q, \tag{4.8}$$

where U is the average electromagnetic energy stored in the eigenmode of the empty cavity. The power dissipation for the TE and TM modes for Fig. 4.2, denoted by P_E and P_M respectively, then reads

$$P_E=\alpha_E\omega_E\left(\frac{1}{2}\varepsilon_2E_0^2\right)V_a\ , \tag{4.9a}$$

$$\alpha_E=0.04131\left(\frac{\lambda}{a}\right)^3\frac{\gamma_E}{\omega_E}, \tag{4.9b}$$

$$P_M = \alpha_H \omega_M \left(\frac{1}{2} \mu_2 H_0^2 \right) V_a , \tag{4.10a}$$

$$\alpha_H = 0.07767 \left(\frac{\lambda}{a} \right)^3 \frac{\gamma_M}{\omega_M}, \tag{4.10b}$$

where E_0 (H_0) is the peak value of the RF electric (magnetic) field of the TE (TM) mode at the center of the cavity in the absence of the spherical particulate (Fig. 4.3), whose half volume is $V_a = (2\pi/3)a^3$, and α_E (α_H) is known as the particulate polarizability [105-107] for the TE (TM) mode [cf. Eqs. (20) and (32) of Ref. 103].

The asymptotic formulas for α_E in Eq. (4.9b) and α_H in (4.10b) may be expressed in terms of the skin depth $\delta = (2/\omega\mu_2\sigma)^{1/2}$ [cf. Eqs. (36) and (37) of Ref. 103],

$$\alpha_E \cong 9\pi^2 \left(\frac{a\delta}{\lambda^2} \right) \sqrt{\frac{\mu_1}{\mu_2}}, \quad \sqrt{\frac{\mu_2}{\mu_1}} \frac{\delta}{a} << 1; \tag{4.11a}$$

$$\alpha_E \cong 18\pi^2 \left(\delta / \lambda \right)^2, \quad 1 << \sqrt{\frac{\mu_2}{\mu_1}} \frac{\delta}{a} << \frac{1}{\pi\sqrt{2}} \sqrt{\frac{\varepsilon_2}{\varepsilon_{1r}}} \sqrt{\frac{\mu_2}{\mu_1}} \left(\frac{\lambda}{a} \right); \tag{4.11b}$$

$$\alpha_E \cong \frac{\left(\lambda / \delta \right)^2}{2\pi^2} \left(\frac{3}{2 + \varepsilon_{1r} / \varepsilon_2} \right)^2, \quad 1 << \frac{1}{\pi\sqrt{2}} \sqrt{\frac{\varepsilon_2}{\varepsilon_{1r}}} \sqrt{\frac{\mu_2}{\mu_1}} \left(\frac{\lambda}{a} \right) << \sqrt{\frac{\mu_2}{\mu_1}} \frac{\delta}{a}; \tag{4.11c}$$

$$\alpha_H \cong \frac{9}{4} \frac{\delta}{a} \sqrt{\frac{\mu_1}{\mu_2}}, \quad \sqrt{\frac{\mu_2}{\mu_1}} \frac{\delta}{a} << 1; \tag{4.12a}$$

$$\alpha_H \cong \frac{1}{5} \left(\frac{a}{\delta} \right)^2 \left(\frac{\mu_1}{\mu_2} \right)^2 \left(\frac{3}{2 + \mu_1 / \mu_2} \right)^2, \quad \sqrt{\frac{\mu_2}{\mu_1}} \frac{\delta}{a} >> 1. \tag{4.12b}$$

Tang *et al*. [103] shows that the asymptotic formulas, Eqs. (4.11) and (4.12), give an excellent qualitative representation of the exact forms, Eqs. (4.9b) and (4.10b). Figure 4.4(a) shows the asymptotes of α_E as a function of δ/a for different values of λ/a, for the special case $\mu_1 = \mu_2 = \mu_0$, and $\varepsilon_{1r} = \varepsilon_2 = \varepsilon_0$. Note that for a given λ/a, there are two break

points for α_E. The first break point at a lower value of δ/a corresponds to $a \sim \delta$, and the second break point at a higher value of δ/a corresponds to $\sigma E \sim \omega\varepsilon_0 E$, i.e. the conduction current is on the order of displacement current, as shown clearly in Fig. 4.4(a). From the interception of the asymptotic expansions (4.11b) and (4.11c), i.e. the second break point, one estimates that the maximum value of α_E is of order 3, occuring at a value of δ/a = 0.13 (λ/a), as shown in Fig. 4.4(a). Figure 4.4(b) shows the asymptotes of α_H as a function of δ/a for the same special case $\mu_1 = \mu_2 = \mu_0$, and $\varepsilon_{1r} = \varepsilon_2 = \varepsilon_0$. Note from Eqs. (4.12a) and (4.12b) that these asymptotes are independent of λ/a (for $\lambda/a >> 1$). In contrast to α_E, there is only one break point, corresponds to $a \sim \delta$, as shown clearly in Fig. 4.4(b). The maximum value of α_H is about 1.0, occuring at a value of δ/a = 0.446 approximately, as shown in Fig. 4.4(b). Taking the ratio of Eq. (4.11a) and (4.12a), one obtains $\alpha_H / \alpha_E = (\lambda/2\pi a)^2 >> 1$ for a good conducting particulate ($\delta/a << 1$), as is also evident in Fig. 4.4. Thus, heating by the RF magnetic field dominates over the heating by the RF electric field when $\delta/a < 1$ [62, 102, 103, 108].

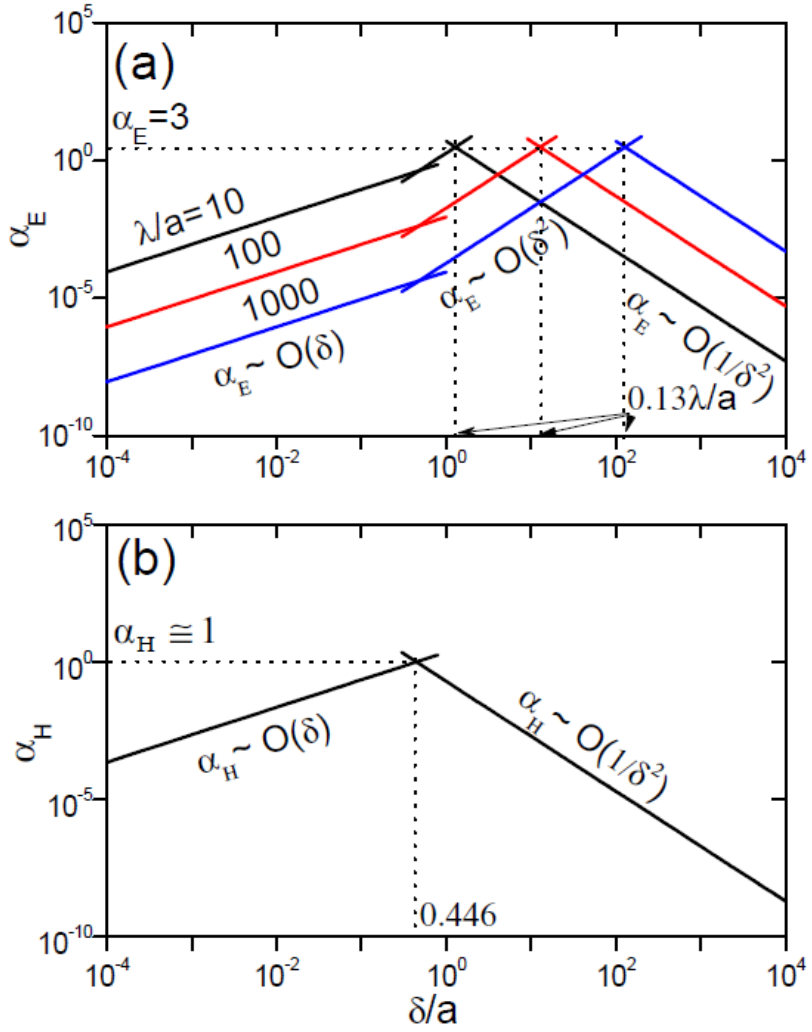

Fig. 4.4 The asymptotes for (a) α_E and (b) α_H as a function of δ/a for $\mu_1/\mu_2 = 1$, $\varepsilon_{1r}/\varepsilon_2 = 1$ and various values of λ/a. These asymptotes yield approximate maximum values of $\alpha_E = 3$ and $\alpha_H = 1.0$. Note that the scaling law for α_H is independent of λ/a.

We should emphasize that, physically, "heating by the RF magnetic field" is actually the *ohmic heating* due to the RF *electric* field that is *induced* within the particulate/protrusion by the external RF magnetic field component (via Faraday's Law), and this is the physical basis of derivation of the magnetic polarizability for nonmagnetic materials by Landau and Lifshitz [107]. Using Eqs. (4.11) and (4.12), Eqs. (4.9) and (4.10)

yield [11],

$$P_E = \begin{cases} 9\pi^2 \dfrac{a\delta}{\lambda^2}\omega U_E V_a, & \dfrac{\delta}{a} << 1, \\ 18\pi^2 \left(\dfrac{\delta}{\lambda}\right)^2 \omega U_E V_a, & 1 << \dfrac{\delta}{a} << \dfrac{\lambda}{a}, \\ \dfrac{1}{2\pi^2}\left(\dfrac{\lambda}{\delta}\right)^2 \omega U_E V_a, & 1 << \dfrac{\lambda}{a} << \dfrac{\delta}{a}, \end{cases} \tag{4.13}$$

$$P_M = \begin{cases} \dfrac{9}{4}\left(\dfrac{\delta}{a}\right)\omega U_H V_a, & \dfrac{\delta}{a} << 1, \\ \dfrac{1}{5}\left(\dfrac{a}{\delta}\right)^2 \omega U_H V_a, & \dfrac{\delta}{a} >> 1, \end{cases} \tag{4.14}$$

where $U_E = (1/2)\varepsilon_0 E_0^2$ and $U_H = (1/2)\mu_0 H_0^2$ for the special case $\mu_1 = \mu_2 = \mu_0$, and $\varepsilon_{1r} = \varepsilon_2 = \varepsilon_0$.

Landau and Lifshitz [p. 303 of Ref. 107] derived both regions, $\delta/a << 1$ and $\delta/a >> 1$, for the P_M in Eq. (4.14); but only the $\delta/a >> \lambda/a >> 1$ regime for P_E in Eq. (4.13). This thesis then provides an extension of Landau and Lifshitz on the electric polarizability α_E, that is, for the entire range of $0 < \delta/a < \infty$.

To quantify the additional heating due to surface roughness relative to the intrinsic ohmic loss in the flat surface, let us now assume that the flat surface is slightly lossy, characterized by its skin depth δ_s. To get an idea on the order of magnitude, let us consider a planar, TEM wave that propagates on the flat surface whose electric and magnetic field amplitude satisfies $E_0 = (\mu_0/\varepsilon_0)^{1/2} H_0$ (Fig. 4.2). Over an area of $1m^2$ on this surface, the ohmic power loss on this flat surface is readily shown to be $P_{flat} = \pi(\delta_s/\lambda)S$, where $S = (1/2)E_0 H_0 = (1/2)E_0^2(\varepsilon_0/\mu_0)^{1/2}$ is the Poynting flux [cf. Eq. (5) on p. 157 of Ref.

104]. Over this unit surface area, let there be N hemispherical protrusions of radius a, so that the fraction of the surface area that is bumpy is $f_{bump} = N\pi a^2$. These protrusions may be considered independent if their average separation is much larger than a [103]. If each protrusion consumes an additional RF power ($P_E + P_M$), where P_E and P_M are given by Eqs. 4.9(a) and 4.10(a), then we obtain

$$R = \frac{P_{protusions}}{P_{flat}} = \frac{N(P_E + P_M)}{\pi(\delta_s / \lambda)(E_0^2 / 2)\sqrt{\varepsilon_0 / \mu_0}}, \tag{4.15}$$

which is the ratio of the additional RF power dissipated by the surface roughness to the intrinsic ohmic loss on the pristine flat surface. Three cases are next examined to illustrate its order of magnitude.

(A) If the hemispherical protrusions are made of the same conducting materials as the flat surface, we set $\delta = \delta_s$ in Eq. (4.14a) and ignore P_E in comparison with P_M (assuming $\delta < a$) to obtain,

$$R = 3 f_{bump}, \tag{4.16}$$

where $f_{bump} = N\pi a^2$ is the fraction of the surface area covered by roughness. Thus, for a nominally flat superconducting surface, where f_{bump} is expected to be very small, the additional ohmic heating on the rough surface as measured by R (in the absence of foreign contaminants) is unlikely to be the reason for any loss of superconductivity. On the other hand, on an ordinary conductor, if its surface exhibits excessive RF power loss, the likely culprit would be foreign objects or grain boundaries that introduce significant additional surface resistance.

(B) If the protrusions are made of foreign objects, the maximum amount of their ohmmic loss through the RF electric field may be estimated by inserting the approximate maximum value of $\alpha_E = 3$ into Eq. (4.9a); see Fig. 4.4(a). Equation (4.15) then gives, upon ignoring the P_M term,

$$R = R_{\max}(TE) = \left(\frac{4a}{\delta_s}\right) f_{bump}. \tag{4.17}$$

(C) Likewise, if the protrusions are made of foreign objects, the maximum amount of their ohmmic loss through the RF magnetic field may be estimated by inserting the approximate maximum value of $\alpha_H = 1.0$ into Eq. (4.10a); see Fig. 4.4(b). Equation (4.15) then gives, upon ignoring the P_E term,

$$R = R_{\max}(TM) = \left(\frac{1.33a}{\delta_s}\right) f_{bump}. \tag{4.18}$$

Equation (4.15) may provide a useful estimate on the additional loss due to surface features that are difficult to simulate directly in a numerical code. If ohmic loss is a serious issue, as expected in a submillimeter traveling wave tube because of its low gain [54], additional loss due to surface roughness poses a very serious threat. Equation (4.15), together with experimental measurements of the geometric surface features, may provide a characterization of such additional loss, and the latter may then be included in a more realistic design.

4.4 RF field enhancements

The modifications of the eigenfunctions by the spherical particulate in Fig. 4.3(a) and Fig. 4.3(b) give the enhancements in the RF electric field and in the RF magnetic field for the hemispherical protrusions in Fig. 4.2(a) and Fig. 4.2(b), respectively. We treat these two cases separately below.

4.4.1 RF Electric Field Enhancement

The local RF electric field at the location of the protrusion in Fig. 4.3(a) may be obtained from the r-component and θ-component of electric field in region II for the TE mode. They read [cf. Eq. (9) of Ref. 103]

$$E_r = \frac{2B\cos\theta}{j\omega\varepsilon_2 r}\left[Y'(\eta)\, j(k_2 r) - J'(\eta) y(k_2 r)\right], \tag{4.19}$$

$$E_\theta = \frac{B\sin\theta}{j\omega\varepsilon_2 r}\left[Y'(\eta) J'(k_2 r) - J'(\eta) Y'(k_2 r)\right], \tag{4.20}$$

where B is an arbitrary constant, $j(\xi), y(\xi), J(\xi)$, and $\mathrm{Y}(\xi)$ are defined in Eqs. (4.3) - (4.5), $k_2 = \omega(\varepsilon_2\mu_2)^{1/2}$, $\eta = k_2 b$, and the prime denotes the derivative with respect to the argument. For these fields to give a constant RF electric field E_0, at the center of the cavity in the absence of the particulate, we find the constant B to be related to E_0 by

$$E_0 = B\left(-j\frac{2}{3}Y'(\eta_E)\right)\sqrt{\frac{\mu_2}{\varepsilon_2}}, \tag{4.21}$$

where $\eta_E = 2\pi b/\lambda = 2.74371$.

The introduction of a small protrusion modifies the eigenvalue by a small amount, $\omega = \omega_E + \delta\omega$, $\eta = \eta_E + \delta\eta$, and $\xi_2 = \xi_{2E} + \delta\xi_2$ where $\xi_{2E} = 2\pi a/\lambda = \eta_E(a/b)$. It can be easily shown that $\delta\omega/\omega_E = \delta\eta/\eta_E = \delta\xi_2/\xi_{2E}$, given by Eq. (4.1). By evaluating Eqs. (4.19) and (4.20) at point *A*, the apex, and at point *C*, the base, respectively [Fig. 4.3(a)], and expanding about the unperturbed values η_E, ω_E and ξ_E, we obtain the amplitude of the electric field at points A and C in the limit $a/\lambda << 1$,

$$E_A = \beta_{EA} E_0, \tag{4.22a}$$

$$\beta_{EA} = \left| 1 + \frac{\delta\omega}{\omega_E} F_A \right|, \tag{4.22b}$$

$$F_A = -1 + \eta_E \frac{Y''(\eta_E)}{Y'(\eta_E)} + \xi_{2E} \frac{j'(\xi_{2E})}{j(\xi_{2E})} - \eta_E \frac{J''(\eta_E) y(\xi_{2E})}{Y'(\eta_E)\, j(\xi_{2E})}, \tag{4.22c}$$

$$E_C = \beta_{EC} E_0, \tag{4.23a}$$

$$\beta_{EC} = \left| 1 + \frac{\delta\omega}{\omega_E} F_C \right|, \tag{4.23b}$$

$$F_C = -1 + \eta_E \frac{Y''(\eta_E)}{Y'(\eta_E)} + \xi_{2E} \frac{J''(\xi_{2E})}{J'(\xi_{2E})} - \eta_E \frac{J''(\eta_E) Y'(\xi_{2E})}{Y'(\eta_E) J'(\xi_{2E})}, \tag{4.23c}$$

where β_{EA} and β_{EC} are the electric field enhancement factor at points *A* and *C* due to the presence of the hemispherical protrusion at the flat surface, respectively, and $\delta\omega/\omega_E$ is given by Eq. (4.1).

Figure 4.5 shows β_{EA} and β_{EC} as a function of δ/a, setting $\mu_1/\mu_2 = 1$, $\varepsilon_{1r}/\varepsilon_2 = 1$ and $\lambda/a = 100$. As the skin depth becomes much smaller than the radius of the bump, $\delta/a \sim 0$, the bump is nearly perfect conducting, the field enhancement factor

at apex is around 3, which agrees well with previous studies [109, 110]. At the base point *C* [Fig. 4.3(a)], the electric field is forced to become normal to both the hemispherical surface and the flat surface, which are perpendicular to each other [Fig. 4.3(a)], thus the electric field vanishes and the electric field enhancement factor approaches zero. On the other hand, as skin depth assumes a very large value, the bump is almost dielectric, with the same permeability and permittivity as vacuum, $\mu_1 / \mu_2 = 1, \varepsilon / \varepsilon_2 \cong \varepsilon_{1r} / \varepsilon_2 = 1$, the RF electric field is not perturbed and the field enhancement factor at both points *A* and *C* converges to the value of 1, as expected, and shown also in Fig. 4.5.

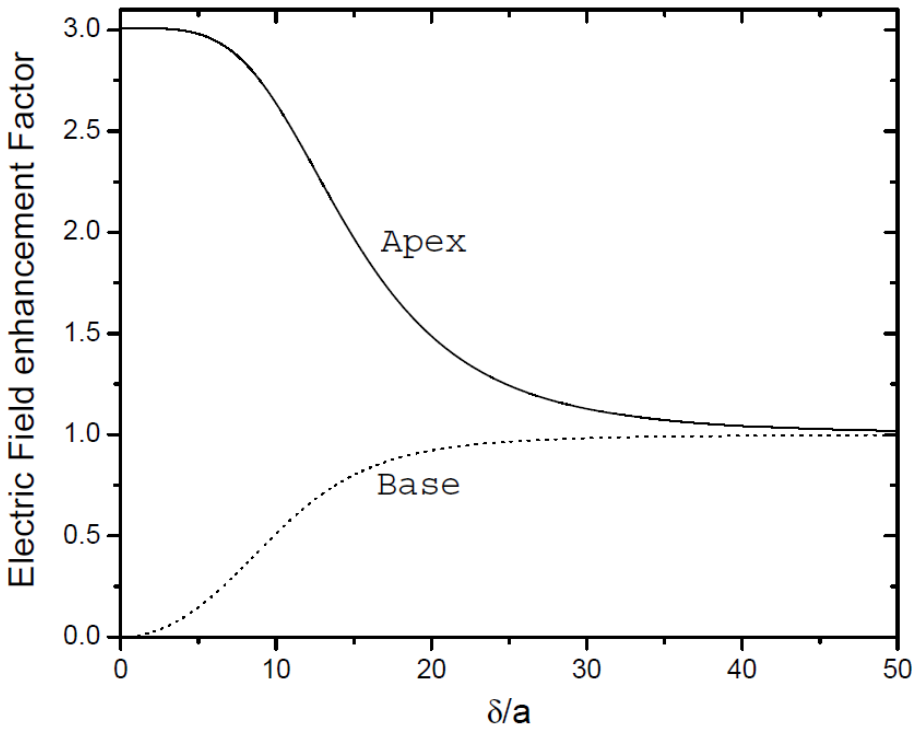

Fig. 4.5 The electric field enhancement factor on the hemispherical protrusion at the apex (β_{EA}, solid curve) and at the base (β_{EC}, dotted curve) as a function of δ/a, setting $\mu_1/\mu_2 = 1$, $\varepsilon_{1r}/\varepsilon_2 = 1$ and $\lambda/a = 100$.

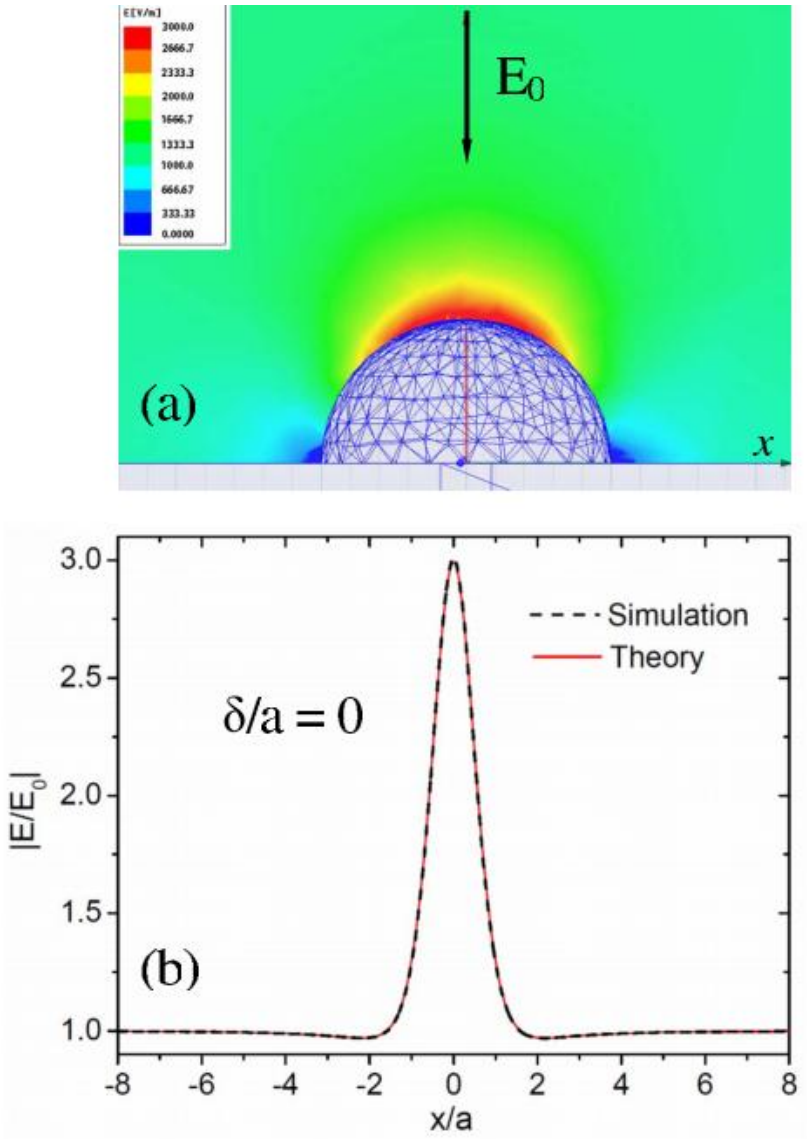

Fig. 4.6 Maxwell 3D results of (a) electric field distribution around the hemispherical bump, (b) magnitude of electric field along a horizontal line 0.5 cm (=bump radius) above the flat surface (dashed line), which agrees extremely well with the analytical calculation (solid line). E_0 is the electric field far away from the bump.

A 3D finite element code Maxwell 3D [85] was used to verify the field enhancement factor calculated analytically as well as the field distribution. The hemispherical protrusion was situated on a flat, perfectly conducting surface, as shown in Fig. 4.6. The electric field is strongest at the apex and weakest at the base. In Fig. 4.6(a), by reading

the color bar, the electric field at the apex is roughly 3 times of the background value, which is confirmed in Fig. 4.6(b), where the magnitude of electric field, $(E_r^2 + E_\theta^2)^{1/2}$, is plotted along a horizontal line at a distance of one protrusion radius above the flat surface, showing a field enhancement factor of 3 clearly. As shown in Fig. 4.6(b), the analytical calculation from Eqs. (4.19) and (4.20) gives identical results as the simulation. Note that the field enhancement profile is independent of the radius of the protrusion.

4.4.2 RF magnetic field enhancement

The local magnetic field at the location of the bump on a flat surface can be similarly calculated using the model of Fig. 4.3(b). The θ-component and r-component of the RF magnetic field in region II of Fig. 4.3(b) are [cf. Eq. (25) of Ref. 103]

$$H_\theta = \frac{D\sin\theta}{j\omega\mu_2 r}\left[y(\eta)J'(k_2 r) - j(\eta)Y'(k_2 r)\right], \tag{4.24}$$

$$H_r = \frac{2D\cos\theta}{j\omega\mu_2 r}\left[y(\eta)j(k_2 r) - j(\eta)y(k_2 r)\right], \tag{4.25}$$

respectively, where D is an arbitrary constant, $j(\xi), y(\xi), J(\xi)$, and $\mathrm{Y}(\xi)$ are defined in Eqs. (4.3) - (4.5), $k_2 = \omega(\varepsilon_2\mu_2)^{1/2}$, $\eta = k_2 b$, and the prime denotes the derivative with respect to the argument. For these fields to give a constant RF magnetic field H_0, at the center of the cavity in the absence of the particulate, the constant D is related to H_0 by

$$H_0 = D\left(-j\frac{2}{3}y(\eta_M)\right)\sqrt{\frac{\varepsilon_2}{\mu_2}}, \tag{4.26}$$

where $\eta_M = 2\pi b/\lambda = 4.4934$.

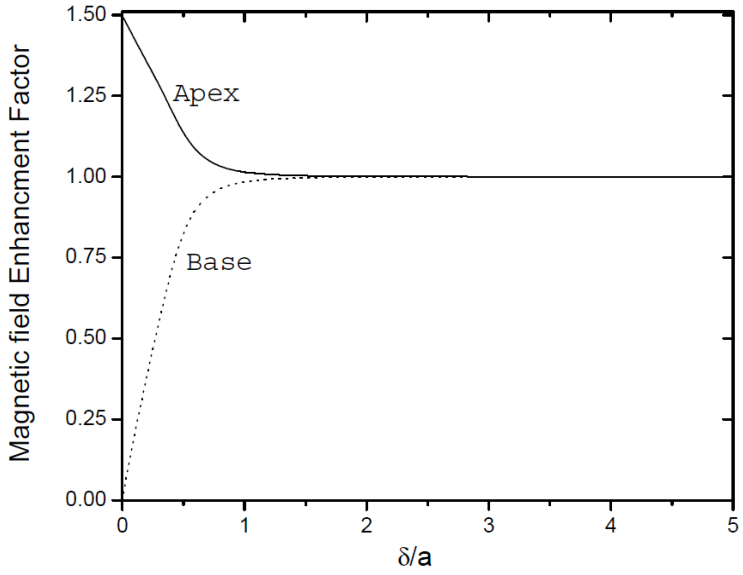

Fig. 4.7 The magnetic field enhancement factor on the hemispherical protrusion at the apex point A (β_{MA}, solid curve) and at the base point C (β_{MC}, dotted curve) as a function of δ/a, setting $\mu_1/\mu_2 = 1$, $\varepsilon_{1r}/\varepsilon_2 = 1$ and $\lambda/a = 100$.

The introduction of a small protrusion modifies the eigenvalue η_M by a small amount. Analogous to Eqs. (4.22) and (4.23), we obtain the amplitude of the RF magnetic field at points *A* and *C* of Fig. 4.3b in the limit $a/\lambda << 1$,

$$H_A = \beta_{MA} H_0, \tag{4.27a}$$

$$\beta_{MA} = \left| 1 + \frac{\delta\omega}{\omega_M} G_A \right|, \tag{4.27b}$$

$$G_A = -1 + \eta_M \frac{y'(\eta_M)}{y(\eta_M)} + \xi_{2M} \frac{J''(\xi_{2M})}{J'(\xi_{2M})} - \eta_M \frac{j'(\eta_M) Y'(\xi_{2M})}{y(\eta_M) J'(\xi_{2M})}, \tag{4.27c}$$

$$H_C = \beta_{MC} H_0, \tag{4.28a}$$

$$\beta_{MC} = \left| 1 + \frac{\delta\omega}{\omega_M} G_C \right|, \tag{4.28b}$$

$$G_C = -1 + \eta_M \frac{y'(\eta_M)}{y(\eta_M)} + \xi_{2M} \frac{j'(\xi_{2M})}{j(\xi_{2M})} - \eta_M \frac{j'(\eta_M) y(\xi_{2M})}{y(\eta_M) j(\xi_{2M})}, \tag{4.28c}$$

where β_{MA} and β_{MC} are the magnetic field enhancement factor at points *A* and *C* due to the presence of the hemispherical protrusion at the flat surface, respectively, $\xi_{2M} = 2\pi a/\lambda = \eta_M (a/b)$, and $\delta\omega/\omega_M$ is given by Eq. (4.2).

Figure 4.7 shows β_{MA} and β_{MC} as a function of δ/a, setting $\mu_1/\mu_2 = 1$, $\varepsilon_{1r}/\varepsilon_2 = 1$ and $\lambda/a = 100$. As the skin depth becomes much smaller than the radius of the bump, $\delta/a \sim 0$, the bump is nearly perfect conducting, the magnetic field enhancement factor at apex is 1.5, which confirms the result obtained by Shemelin and Padamsee, who simulated the magnetic field enhancement at bumps on the surface of a pill-box cavity using the code SLANS2 [53]. Note that this magnetic field enhancement factor at the apex of a hemispherical bump on a flat surface is the same as that of an isolated perfectly conducting sphere inserted in a uniform magnetic field [111]. Note from Fig. 4.7 that the maximum magnetic field enhancement factor is given by materials with zero skin depth, i.e., a superconductor, in which case the local high magnetic field could exceed the critical magnetic field for superconductivity, even though the RF magnetic field is below this critical value for a pristine, flat surface. Thus surface roughness could lead to abrupt loss of superconductivity [53, 66, 67]. Note further that this magnetic field enhancement factor is independent of the size of the hemispherical protrusion. Thus, it is extremely important to create ultra-smooth, polished surfaces to retain superconductivity in the presence of large RF magnetic fields, and this is consistent with the current challenge in superconducting cavity fabrication [53, 57, 61]. At the base point *C* [Fig. 4.3(b)], the magnetic field normal to the bump surface vanishes and the

field enhancement factor becomes zero. When the skin depth becomes comparable to the bump radius, the magnetic field enhancement factor at both points *A* and *C* becomes nearly unity (Fig. 4.7).

The Maxwell 3D code [85] was used again to verify the magnetic field enhancement factor calculated analytically as well as the field distribution due to the hemispherical protrusion situated on a perfectly conducting surface, as shown in Fig. 4.8. The magnetic field is strongest along the great circle whose plane is perpendicular to the applied magnetic field, according to color bar in Fig. 4.8(a). The magnetic field at the apex is roughly 1.5 times of the background value. The magnitude of the magnetic field, $(H_r^2 + H_\theta^2)^{1/2}$, is plotted along two horizontal lines at a distance of one bump radius above the flat surface, one line (Line 1) in the plane parallel to and the other line (Line 2) perpendicular to the applied magnetic field, as shown in Fig. 4.8 (b) and (c), respectively. Both plots clearly show a magnetic field enhancement of 1.5. The simulation results agreed extremely well with our analytically calculated results from Eqs. (4.24) and (4.25), as shown by the solid lines in Fig. 4.8 (b) and (c). The field enhancement profile is independent of the size of the protrusion.

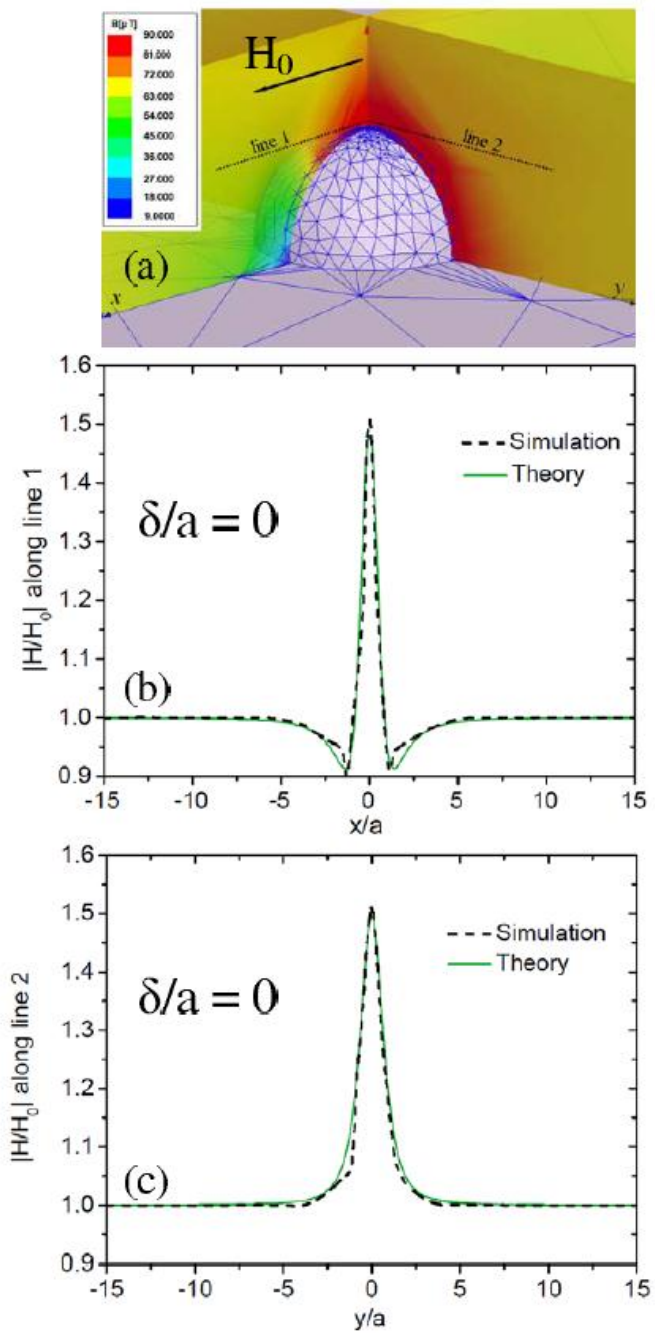

Fig. 4.8 Maxwell 3D results. (a) Magnetic field distribution around the hemispherical bump in the plane parallel and perpendicular to the applied field. Plot of the magnitude of magnetic field (dashed lines) along Line 1 (b), and along Line 2 (c), both are horizontal lines 1.0 cm (=one bump radius) above the flat surface. Also shown are the analytical calculations (solid lines). H_0 is the magnetic field far away from the bump.

4.5 Concluding remarks

This chapter gives a self-consistent, accurate evaluation of the modification of the electromagnetic field due to a hemispherical protrusion setting on a locally flat conducting surface. Two major assumptions were made: (a) the size of the protrusion is small compared with the wavelength of the radiation, and with the local radius of curvature if the surface is curved, and (b) the complex permittivity and permeability of the protrusion are constant. The latter constants may assume arbitrary values, however. The local RF electric and RF magnetic fields, $\mathbf{E_0}$ and $\mathbf{B_0}$ in the absence of the protrusion, may have arbitrary magnitudes and phases between them. The ohmic absorption by the protrusion is calculated, and compared with the intrinsic ohmic absorption of an otherwise flat surface. Our study suggests that if excessive ohmic loss on a nominally flat metallic surface occurs, it is most likely due to foreign objects or grain boundaries that greatly increase the surface resistance. It could also be caused by pits or dimples which have much larger field enhancement factors. (Enhanced loss on pits or dimples is much more difficult to treat, and is beyond the scope of this thesis.)

The RF electric field enhancement and RF magnetic field enhancement due to the hemispherical protrusion is also calculated. These field enhancement factors do not depend on the size of the protrusion, and they are modest (maximum value of 3 for RF electric field enhancement and 1.5 for RF magnetic field enhancement). While these are only modest enhancements and are simply the classical, static value expected on a

conducting protrusion, (due to the assumed smallness of the bump compared with the wavelength), the magnetic field enhancement due to surface roughness remains a major concern in the design of superconducting cavities. Once more, other surface defects, such as dimples and pits on surface [53], could induce significant RF electric and magnetic field enhancements, in contrast to the hemispherical protrusions considered here.

It is interesting to note that in all of our calculations of the perturbed electromagnetic fields, we assume a small protrusion. Yet the above-quoted finite values of field enhancement factors remain as long as the protrusion exists, regardless of its size. That is, a regular perturbation technique yields a finite but different result in the limit of the vanishingly small expansion parameter (a/λ). The approach of decomposition into separate TE and TM modes, and the perturbation techniques in the smallness of the protrusion radius, apparently are valid, as our results agree with numerical codes, and with the known results in the appropriate limit in this purely classical (non-quantum mechanical) analysis.

Since the amplitudes and the phases of $\mathbf{E_0}$ and $\mathbf{B_0}$ of the local electromagnetic field are arbitrary, this local electromagnetic field may be due to an incident wave at arbitrary incident angle and arbitrary polarization. As we have self-consistently, and accurately calculated the (nontrivial) modification of $\mathbf{E_0}$ and $\mathbf{B_0}$ by a local hemispherical protrusion, we have essentially paved the way to calculate the scattered radiation of an arbitrary incident wave due to such a protrusion, subject only to the two relatively weak assumptions stated in the first paragraph of this section.

Finally, what we have calculated here includes the complete RF field solutions at a triple point, defined as the interface between dielectric, metal and vacuum [8]. The maximum field enhancement factors are given by that of a perfect conductor, in the limit of a static field (electric or magnetic). Thus, if we are only interested in the maximum field enhancement factors for a complex protrusion geometry, we may simply use electrostatic and magnetostatic field solvers for that geometry [53, 74, 109-111]. However, the RF heating caused by the protrusion is considerably more difficult to assess.

CHAPTER 5

CONCLUSION AND SUGGESTED FUTURE WORK

This thesis addresses several issues on the effects of surface roughness. They include contact resistance of both bulk contacts and thin film contacts, surface roughness induced enhanced power absorption, and electrical field and magnetic field enhancements. These are important issues. They appear in a multitude of disciplines in science and engineering.

5.1 On Bulk Contact Resistance

Simple, accurate, analytical scaling laws have been developed for the contact resistance with dissimilar materials of bulk contacts. Both Cartesian and cylindrical geometries are analyzed. The scaling laws are synthesized based on vast amount of data, obtained from exact calculations of the series expansion method. They have been validated in various limits, including experiments. The model is a substantial generalization of Holm's *a*-spot theory, with a finite contact region, and with arbitrary values of dimensions and resistivities of the contact members. On an asperity (small protrusion) that joint the two current channels, we find the decomposition of the asperity resistance into bulk and interface resistance is valid in general. If the asperity is highly

resistive, then its bulk resistance dominates over its interface resistance. We also find that this interface depends mainly on the electrical resistivity of the two current channels that are jointed by the asperity, and is otherwise insensitive to the resistivity in the asperity itself. Interestingly, we also discover a close connection between the high frequency, bulk contact resistance and the DC contact resistance in thin film (Fig. 3.23).

Future work on the bulk contact resistance study may include a statistical treatment for contacting rough surfaces, by using our scaling laws as the building block for the contact resistance of a single asperity. A statistical theory of finding the resistance of a cluster of micro-contacts may be derived to compare with resistance measurements of real contacting rough surfaces. Our model is based on the assumption that the contact members are semi-infinite in length. Thus, an important generalization of our theory is to consider the effects of the finite length of the contact members. One may also evaluate ohmic heating at the bulk contacts based on the newly calculated potential (and therefore current flow) profile, though caution is needed to account for the temperature dependence of electrical resistivity, thermal conductivity, dimensions, and heat loss mechanisms. The RF heating at these contacts should be studied, together with the capacitive and inductive effects of the asperities. Including semiconductors as contact members in our contact resistance model may also be explored in the future. With the recent advances in nanotechnology, electrical contacts may be formed in micro- or nano-scale. The behavior of such miniature electrical contacts may be significantly different from the classical contacts as studied in this thesis, due to quantum effects and long mean-free path effects,

for instance. One may also adapt the results of contact resistance to the steady state heat flow in thermally insulated structures with dissimilar thermal properties.

5.2 On Thin Film Contact Resistance

Accurate analytic models and scaling laws are also developed for the contact resistance (constriction resistance) of thin film contacts with dissimilar materials over a huge parameter space. The models assume arbitrary aspect ratios, and arbitrary resistivity ratios in the different regions for both Cartesian and cylindrical geometries. We quantify the large distortions of the field lines as a result of film thickness. We found that, at a given resistivity ratio, the thin film contact resistance primarily depends only on the ratio of constriction size (a) to the film thickness (h). In the latter cases, the electrostatic fringe field is restricted to the constriction corner only, and becomes insensitive to the location of terminals for the thin film region. The effect of dissimilar materials is also analyzed. Typically the minimum contact resistance is realized with $a/h \sim 1$, for both Cartesian and cylindrical cases. Various limiting cases are studied and validated with known results. This work may offer useful insights into the design and fabrication of thin film devices and components.

We found that the normalized thin film spreading resistance converges to the finite values, 2.77 for Cartesian and 0.28 for cylindrical case in the limit $h \to 0$. We conjecture that the same finite limits of normalized thin film spreading resistance would apply to the

a-spot between bulk solids in the AC case as the skin depth $\delta \to 0$, if the thickness of the equivalent thin film is identified as the skin depth at the relevant frequency, i.e., $h = \delta$. This is an interesting link between the AC bulk contact resistance and the DC thin film contact resistance. Extension of the thin film contact model to a general *a*-spot geometry is made. Our DC thin film model is also compared with the widely used transmission line model and the experimental transfer length method for semiconductor device characterization [91].

Future work on the thin film contact resistance study may include evaluating local ohmic heating due to current crowding at thin-film contacts. The local intense current crowding near the constriction corner would lead to excessive ohmic heating there, which typically will increase the local electrical resistivity and decrease the local thermal conductivity, which in turn would induce more ohmic heating, and eventually lead to circuit failure, a form of electro-thermal instability. Also, the non-uniform distribution of heat dissipation could introduce net stress at the contact interface and cause the migration of atoms there. These important issues need to be studied in the future. Our thin film model may also be extended to allow arbitrary voltages at the three terminals shown in Fig. 3.1.

For the thin film contact studied in this thesis, the current is always assumed to flow parallel to the bottom boundary of thin film region (Fig. 3.1), i.e. a “horizontal” contact. The work may be naturally extended to study the “vertical” contact, where the current flows normally to the thin film bottom boundary, that is, the thin film bottom boundary is

considered as an equipotential. Future work may include experimental validation of the scaling laws for the contact resistance with dissimilar materials. Inclusion of our model for the fringing field effects into the widely used transmission line model is also of great interest.

5.3 On RF Heating and Field Enhancement

The thesis presented a self-consistent, accurate evaluation of the modification of the electromagnetic field due to a hemispherical protrusion setting on a locally flat conducting surface. It is assumed that the size of the protrusion is small compared with the wavelength of the radiation. The protrusion itself may assume arbitrary values of ε, μ, and σ. The local RF electric and RF magnetic fields in the absence of the protrusion may have arbitrary magnitudes and phases between them. The ohmic absorption by the protrusion is calculated, and compared with the intrinsic ohmic absorption of an otherwise flat surface. We conclude that if excessive ohmic loss on a nominally flat metallic surface occurs, it is most likely due to foreign objects, or grain boundaries, or pits or dimples that greatly increase the surface resistance. Grain boundaries, pits and dimples are not studied in this thesis.

The RF electric field enhancement and RF magnetic field enhancement due to the hemispherical protrusion are also calculated. These field enhancement factors do not depend on the size of the protrusion, and they are modest (maximum value of 3 for RF

electric field enhancement and 1.5 for RF magnetic field enhancement). While these are only modest enhancements and are simply the classical, static value expected on a conducting protrusion, this magnetic field enhancement due to surface roughness remains a major concern in the design of superconducting cavities.

Future work may use our scaling laws to estimate the effective resistivity of practical rough surface. This can be done by a statistical treatment, where the surface roughness is mimicked by a distribution of hemispherical bumps of different sizes and materials properties. If the power absorption of a hot spot on a superconducting surface is experimentally determined, our model can be used to evaluate the material properties of this spot, and therefore help determining the possible origin of its formation. The surface resistivity vs surface roughness in existing experimental scalings (Fig. 1.8) remains to be explained. Our analysis may also be extended to other useful geometries, such as cylindrical rod protrusion, or elliptical protrusions. Pits and dimples on surface, which usually give a much higher electric and magnetic field enhancement than protrusions, needs to be assessed in the future. In this thesis, we assume the protrusion is small compared to the wavelength, $a << \lambda$. Future work may explore the situation when the protrusion size is on the order of wavelength, $a \sim \lambda$, a regime important for optoelectronics. Since the amplitudes and the phases of electric and magnetic components of the local electromagnetic field are arbitrary, this electromagnetic field may be due to an incident wave at arbitrary incident angle and arbitrary polarization. Our study essentially paved the way to calculate the scattered radiation of an arbitrary incident wave

from a small protrusion with arbitrary ε, μ, σ.

Appendix A

The contact resistance of a constricted cylindrical channel

Referring to Fig. 2.4, Regions I and II are semi-infinite in the axial z-direction, with the interface at $z = 0$. For the cylindrical case, the Laplace's equation yields,

$$\begin{aligned}\Phi_+(r,z) &= A_0 + \sum_{n=1}^{\infty} A_n J_0(\alpha_n r) e^{-\alpha_n z} - E_{+\infty} z, \qquad z > 0, r \in (0,a);\\ \Phi_-(r,z) &= \sum_{n=1}^{\infty} B_n J_0(\beta_n r) e^{+\beta_n z} - E_{-\infty} z, \qquad z < 0, r \in (0,b),\end{aligned} \tag{A1}$$

where Φ_+ and Φ_- are the electrical potential in the semi-infinite cylindrical channel I and II respectively, $E_{+\infty}$ and $E_{-\infty}$ are the uniform electric fields far from $z = 0$, $J_0(x)$ is the zeroth order Bessel function of the first kind, α_n and β_n satisfy $\alpha_n a = \beta_n b = X_n$, where X_n is the nth positive zero of $J_1(x) = -dJ_0(x)/dx$, and A_n and B_n are the coefficients that need to be solved. Without loss of generality, we set the coefficient B_0 to zero in Eq. (A1) for convenience. Current conservation requires that $a^2 E_{+\infty} / \rho_1 = b^2 E_{-\infty} / \rho_2$.

At the interface $z = 0$, continuity of electrical potential and current density leads to the following boundary conditions,

$$\Phi_+ = \Phi_-, \qquad z = 0, r \in (0,a), \tag{A2a}$$

$$\frac{1}{\rho_1}\frac{\partial \Phi_+}{\partial z} = \frac{1}{\rho_2}\frac{\partial \Phi_-}{\partial z}, \qquad z = 0, \ \ r \in (0,a), \tag{A2b}$$

$$\frac{\partial \Phi_-}{\partial z} = 0, \qquad z = 0, \;\; \mathrm{r} \in (a,b)\,, \tag{A2c}$$

From Eqs. (A1) and (A2a), A_n is related to B_n as,

$$A_0 = 2\sum_{n=1}^{\infty} B_n \frac{J_1\left(X_n a/b\right)}{X_n a/b}, \tag{A3a}$$

$$A_n = \sum_{m=1}^{\infty} B_m g_{mn}, \;\; g_{mn} = \frac{2}{a^2 J_0^2\left(X_n\right)} \int_0^a r J_0\left(\alpha_n r\right) J_0\left(\beta_m r\right) dr, \quad n \geq 1. \tag{A3b}$$

A change of integration variable shows that g_{mn} depends only on b/a, m, and n.

Combining Eqs. (A2b), (A2c), and (A3b), we obtain

$$B_n + \frac{a}{b}\frac{\rho_2}{\rho_1}\frac{1}{X_n J_0^2\left(X_n\right)} \sum_{m=1}^{\infty} \gamma_{mn} B_m = \frac{\rho_2}{\rho_1}\frac{2J_1\left(X_n a/b\right)}{X_n^2 J_0^2\left(X_n\right)}, \; n = 1, 2, 3..., \tag{A4}$$

where

$$\gamma_{mn} = \gamma_{nm} = \sum_{l=0}^{\infty} g_{ml} g_{nl} X_l J_0^2\left(X_l\right), \tag{A5}$$

and g_{ml} and g_{nl} is in the form of the last part in Eq. (A3b). In writing Eq. (A4), we have set $aE_{+\infty} = -1$ for simplicity. It is easy to show that Eq. (A5) can be written as

$$\gamma_{nm} = \gamma_{mn} = \sum_{l=1}^{\infty} \frac{4x^2 X_m X_n X_l J_1\left(X_m x\right) J_1\left(X_n x\right)}{(X_l^2 - X_m^2 x^2)(X_l^2 - X_n^2 x^2)}, \;\; x = a/b\,, \tag{A6}$$

which indicates that $\gamma_{nm} = \gamma_{mn} \propto 1/X_n \propto 1/n$ as $n \to \infty$. From Eq. (A4), $B_n \propto 1/X_n^{\,2} \propto 1/n^2$ as $n \to \infty$. Therefore, the infinite matrix equation, (A4), can be inverted directly to solve for B_n with convergence guaranteed.

The total resistance between an arbitrary point (z = L_1) in Region I and an arbitrary point (z = -L_2) in Region II (Fig. 2.4), both far from the interface, is R = (Φ_{L2}-Φ_{L1})/I, where $I = \left|\pi a^2 E_{+\infty}/\rho_1\right| = \pi a/\rho_1$ is the total current in the conducting

channel. The contact resistance R_c, which is the difference between the total resistance R and bulk resistance $R_u = \rho_1 L_1/\pi a^2 + \rho_2 L_2/\pi b^2$, is found from Eq. (A1) and (A3a),

$$R_c = \frac{|A_0|}{I} = \frac{\rho_2}{4a}\bar{R}_c, \qquad \bar{R}_c = \bar{R}_c\left(\frac{b}{a}, \frac{\rho_1}{\rho_2}\right) = \frac{8}{\pi}\frac{\rho_1}{\rho_2}\left|\sum_{n=1}^{\infty} B_n \frac{J_1(X_n a/b)}{X_n a/b}\right|, \tag{A7}$$

which is the *exact* expression for the contact resistance at the interface of two semi-infinite cylindrical channels of dissimilar materials (Fig. 2.4). It appears in Eq. (2.1) of the main text. Given the resistivity ratio ρ_1/ρ_2 and aspect ratio b/a, the coefficients B_n are solved numerically from Eq. (A4) by using either the infinite matrix method, or the explicit iterative method, which will be discussed next. $\bar{R}_c$ is then obtained from Eq. (A7).

To solve for the coefficient B_n more efficiently, an explicit iterative method is available for $\rho_2/\rho_1 < 1$. From Eq. (A4), to the lowest order in ρ_2/ρ_1, we have

$$B_n^{(1)} \cong \frac{\rho_2}{\rho_1}\frac{2J_1(X_n a/b)}{X_n^2 J_0^2(X_n)},\ n \geq 1. \tag{A8}$$

To the next order,

$$B_n^{(2)} \cong \frac{\rho_2}{\rho_1}\frac{2J_1(X_n a/b)}{X_n^2 J_0^2(X_n)} - \frac{a}{b}\frac{\rho_2}{\rho_1}\frac{1}{X_n J_0^2(X_n)}\sum_{m=1}^{\infty}\gamma_{mn}B_m^{(1)},\ n \geq 1. \tag{A9}$$

To the kth order, the solution becomes,

$$B_n^{(k)} \cong \frac{\rho_2}{\rho_1}\frac{2J_1(X_n a/b)}{X_n^2 J_0^2(X_n)} - \frac{a}{b}\frac{\rho_2}{\rho_1}\frac{1}{X_n J_0^2(X_n)}\sum_{m=1}^{\infty}\gamma_{mn}B_m^{(k-1)},\ n \geq 1,\ k \geq 2, \tag{A10}$$

which is the Taylor expansion of B_n in increasing power of ρ_2/ρ_1. This iterative scheme is explicit. It gives identical numerical solutions as the infinite matrix method for $\rho_2/\rho_1 < 1$, but converges faster. It converges very rapidly for $\rho_2/\rho_1 << 1$, in which case Eq. (A8) is

an excellent approximation and Eq. (A7) gives,

$$\overline{R}_c\left(\frac{b}{a},\frac{\rho_1}{\rho_2}\right)\cong\frac{16}{\pi}\sum_{n=1}^{\infty}\frac{J_1^2(X_n a/b)}{X_n a/b}\frac{1}{X_n^2 J_0^2(X_n)},\quad \rho_1/\rho_2 >> 1. \tag{A11}$$

Equation (A11) can be further simplified if $a/b << 1$,

$$\overline{R}_c\left(\frac{b}{a},\frac{\rho_1}{\rho_2}\right)\cong 8\sum_{n=1}^{\infty}\frac{J_1^2(X_n a/b)}{X_n^2 a/b},\quad \rho_1/\rho_2 >> 1,\ a/b << 1, \tag{A12}$$

since the first few terms in the infinite sum of Eq. (A11) hardly contribute, and the remaining terms may be approximated by using the well-known asymptotic formula of $J_0(X_n)$ for large X_n. Note that to within an error of less than 0.22 percent,

$$X_n \cong (n + ¼)\pi, \qquad n > 3. \tag{A13}$$

Thus, in the limit $a/b \to 0$, we obtain from Eq. (A12),

$$\overline{R}_c\left(\frac{b}{a},\frac{\rho_1}{\rho_2}\right)\cong 8\int_1^{\infty} dn\,\frac{J_1^2(X_n a/b)}{X_n^2 a/b}\cong\frac{8}{\pi}\int_0^{\infty} d\xi\,\frac{J_1^2(\xi)}{\xi^2}=\frac{32}{3\pi^2};\quad \rho_1/\rho_2 >> 1,\ a/b\to 0, \tag{A14}$$

where we have used Eq. (A13) to write the second integral, which is evaluated exactly in Whittaker and Watson [112].

In the opposite limit, $\rho_1/\rho_2 \to 0$, $\overline{R}_c$ approaches the value for the *a*-spot analyzed by Holm [12] and Rosenfeld and Timsit [15] for the symmetrical case $\rho_2 = \rho_3$ and $b = c$, as discussed in Section 2.3 Case B, and also shown in Fig. 2.5(b). As $a/b \to 0$, the exact theory of symmetrical *a*-spot gives $\overline{R}_c = 1$. Thus, the maximum range of variation of $\overline{R}_c$ for different ρ_1/ρ_2 is $\Delta = 32/3\pi^2 - 1 = 0.08076$, as displayed in Eq. (2.2) of the main text, and in Fig. 2.5.

Appendix B

The contact resistance of a constricted Cartesian channel

Referring to Fig. 2.4, Regions I and II are semi-infinite in the axial z-direction, with the interface at z = 0. For the two-dimensional Cartesian channel, the y-axis is orthogonal to the z-axis in the plane of the paper. The Laplace's equation yields,

$$\begin{aligned}\Phi_{+}(y,z) &= \sum_{n=0}^{\infty} A_n \cos\left(\frac{n\pi y}{a}\right) e^{-\frac{n\pi z}{a}} - E_{+\infty} z, \qquad z>0, y\in(0,a),\\ \Phi_{-}(y,z) &= \sum_{n=1}^{\infty} B_n \cos\left(\frac{n\pi y}{b}\right) e^{+\frac{n\pi z}{b}} - E_{-\infty} z, \qquad z<0, y\in(0,b),\end{aligned} \tag{B1}$$

where Φ_+ and Φ_- are the electrical potential in the semi-infinite cylindrical channel I and II respectively, $E_{+\infty}$ and $E_{-\infty}$ are the uniform electric fields far from z = 0, and A_n and B_n are the coefficients that need to be solved. For convenience, the coefficient B_0 is set to zero in Eq. (B1). Current conservation requires that $aE_{+\infty}/\rho_1 = bE_{-\infty}/\rho_2$.

At the interface z = 0, continuity of electrical potential and current density leads to the following boundary conditions,

$$\Phi_{+} = \Phi_{-}, \qquad z=0, y\in(0,a), \tag{B2a}$$

$$\frac{1}{\rho_1}\frac{\partial\Phi_{+}}{\partial z} = \frac{1}{\rho_2}\frac{\partial\Phi_{-}}{\partial z}, \qquad z=0,\ \ y\in(0,a), \tag{B2b}$$

$$\frac{\partial\Phi_{-}}{\partial z} = 0, \qquad z=0,\ \ y\in(a,b), \tag{B2c}$$

From Eqs. (B1) and (B2a), A_n is related to B_n as,

$$A_0 = \sum_{n=1}^{\infty} B_n \frac{\sin(n\pi a/b)}{n\pi a/b}, \tag{B3a}$$

$$A_n = \sum_{m=1}^{\infty} B_m g_{mn}, \quad g_{mn} = \frac{2}{a}\int_0^a \cos\left(\frac{n\pi y}{a}\right)\cos\left(\frac{m\pi y}{b}\right)dy, \quad n \geq 1. \tag{B3b}$$

A change of integration variable shows that g_{mn} depends only on b/a, m, and n.

Combining Eqs. (B2b), (B2c), and (B3b), we obtain

$$B_n + \frac{1}{n}\frac{\rho_2}{\rho_1}\sum_{m=1}^{\infty}\gamma_{nm}B_m = \frac{2}{n\pi}\frac{\rho_2}{\rho_1}\frac{\sin(n\pi a/b)}{n\pi a/b}, \qquad n = 1, 2, 3..., \tag{B4}$$

where

$$\gamma_{nm} = \gamma_{mn} = \sum_{l=0}^{\infty} l g_{nl} g_{ml}, \tag{B5}$$

and g_{ml} and g_{nl} is in the form of last part in Eq. (B3b). In writing Eq. (B4), we have set $aE_{+\infty} = -1$ for simplicity. It is easy to show that Eq. (B5) can be written as

$$\gamma_{nm} = \gamma_{mn} = \sum_{l=1}^{\infty} \frac{4mnlx^2 \sin(n\pi x)\sin(m\pi x)}{\pi^2(l^2 - n^2x^2)(l^2 - m^2x^2)}, \quad x = a/b, \tag{B6}$$

which indicates that $\gamma_{nm} = \gamma_{mn} \propto 1/n$ as $n \to \infty$. From Eq. (B4), $B_n \propto 1/n^2$ as $n \to \infty$. Therefore, the infinite matrix equation, (B4), can be inverted directly to solve for B_n with convergence guaranteed.

The total resistance between an arbitrary point (z = L_1) in Region I and an arbitrary point (z = -L_2) in Region II (Fig. 2.4), both far from the interface, is R = (Φ_{L2}-Φ_{L1})/I, where $I = |2aW(E_{+\infty}/\rho_1)| = 2W/\rho_1$ is the total current in the conducting channel, where W is the channel width in the third, ignorable dimension. The contact

resistance R_c, which is the difference between the total resistance R and bulk resistance $R_u = \rho_1 L_1 / 2aW + \rho_2 L_2 / 2bW$, is found from Eq. (B1) and (B3a),

$$R_c = \frac{|A_0|}{I} = \frac{\rho_2}{4\pi W}\overline{R}_c, \qquad \overline{R}_c = \overline{R}_c\left(\frac{b}{a}, \frac{\rho_1}{\rho_2}\right) = 2\pi \frac{\rho_1}{\rho_2}\left|\sum_{n=1}^{\infty} B_n \frac{\sin(n\pi a/b)}{n\pi a/b}\right|, \quad \text{(B7)}$$

which is the *exact* expression for the contact resistance at the interface of two semi-infinite Cartesian channels of dissimilar materials. It appears in Eq. (2.4) of the main text. Given the resistivity ratio ρ_1/ρ_2 and aspect ratio b/a, the coefficients B_n are solved numerically from Eq. (B4) by using either the infinite matrix method, or the explicit iterative method, which will be discussed next. $\overline{R}_c$ is then obtained from Eq. (B7).

To solve for the coefficient B_n more efficiently, an explicit iterative method is available for $\rho_2/\rho_1 < 1$. From Eq. (B4), to the lowest order in ρ_2/ρ_1, we have

$$B_n^{(1)} \cong \frac{2}{n\pi}\frac{\rho_2}{\rho_1}\frac{\sin(n\pi a/b)}{n\pi a/b}, \quad n \geq 1. \quad \text{(B8)}$$

To the next order,

$$B_n^{(2)} \cong \frac{2}{n\pi}\frac{\rho_2}{\rho_1}\frac{\sin(n\pi a/b)}{n\pi a/b} - \frac{1}{n}\frac{\rho_2}{\rho_1}\sum_{l=1}^{\infty}\gamma_{nl}B_l^{(1)}, \quad n \geq 1. \quad \text{(B9)}$$

To the kth order, the solution becomes,

$$B_n^{(k)} \cong \frac{2}{n\pi}\frac{\rho_2}{\rho_1}\frac{\sin(n\pi a/b)}{n\pi a/b} - \frac{1}{n}\frac{\rho_2}{\rho_1}\sum_{l=1}^{\infty}\gamma_{nl}B_l^{(k-1)}, \quad n \geq 1,\ k \geq 2, \quad \text{(B10)}$$

which is the Taylor expansion of B_n in increasing power of ρ_2/ρ_1. This iterative scheme is explicit. It gives identical numerical solutions as the infinite matrix method for $\rho_2/\rho_1 < 1$, but converges faster. It converges very rapidly for $\rho_2/\rho_1 << 1$, in which case Eq. (B8) is an

excellent approximation and Eq. (B7) gives,

$$\overline{R}_c\left(\frac{b}{a},\frac{\rho_1}{\rho_2}\right)=4\sum_{n=1}^{\infty}\frac{1}{n}\frac{\sin^2(n\pi a/b)}{(n\pi a/b)^2},\quad \rho_1/\rho_2 >> 1. \tag{B11}$$

In the opposite limit, $\rho_1/\rho_2\to\infty$, $\overline{R}_c$ approaches the a-spot value for the Cartesian channel that is analyzed in Ref. [23] for the symmetrical case $\rho_2 = \rho_3$ and $b = c$. This is discussed in Section 2.3 Case B, and also shown in Fig. 2.6 (b). Thus, the maximum range of variation of $\overline{R}_c$ for different ρ_1/ρ_2 is the difference between Eq. (B11) and $\overline{R}_{c0}(x)\big|_{LTZ}$ that is given by Eq. (2.6) of the main text. This difference is approximately the constant 0.4548 for $b/a >> 1$, as shown in Eq. (2.5) of the main text, and in Fig. 2.6.

Appendix C

The contact resistance of Cartesian thin film

Referring to Fig. 3.1, we assume that $L_1 >> a$, so that the current flow is uniform at the end *GH*, far from the joint region. For the two dimensional Cartesian channel, the y-axis and z-axis are in the plane of the paper. The solutions of Laplace's equation are,

$$\Phi_+(y,z) = A_0 + \sum_{n=1}^{\infty} A_n \cos\left(\frac{n\pi y}{a}\right) e^{-\frac{n\pi z}{a}} - E_{+\infty} z, \qquad z > 0, |y| \in (0,a),$$

$$\Phi_-(y,z) = V_0 + \sum_{n=1}^{\infty} \left[B_n \sinh\left(\frac{(n-1/2)\pi z}{b}\right) + C_n \cosh\left(\frac{(n-1/2)\pi z}{b}\right)\right] \cos\left(\frac{(n-1/2)\pi y}{b}\right), \quad \text{(C1)}$$

$$z < 0, |y| \in (0,b),$$

where Φ_+ and Φ_- are the electrical potential in the region *BCHG* and *BCEF* respectively, $E_{+\infty}$ is the uniform electric fields at the end *GH*, V_0 is the electrical potential at the ends *E* and *F* ($y = \pm b$), and A_n and B_n are the coefficients that need to be solved.

Since the current flows parallel to the thin film boundary *EF*, we have

$$\frac{\partial \Phi_-}{\partial z} = 0, \qquad z = -h, |y| \in (0,b), \quad \text{(C2)}$$

which leads to

$$C_n = B_n \coth\left(\frac{(n-1/2)\pi h}{b}\right). \quad \text{(C3)}$$

At the interface $z = 0$, from the continuity of electrical potential and current density, we have the following boundary conditions,

$$\Phi_+ = \Phi_-, \qquad z = 0, |y| \in (0, a), \tag{C4a}$$

$$\frac{1}{\rho_1}\frac{\partial \Phi_+}{\partial z} = \frac{1}{\rho_2}\frac{\partial \Phi_-}{\partial z}, \qquad z = 0, \quad |y| \in (0, a), \tag{C4b}$$

$$\frac{\partial \Phi_-}{\partial z} = 0, \qquad z = 0, \ |y| \in (a, b). \tag{C4c}$$

From Eqs. (C4a) and (C1), the coefficient A_n is expressed in terms of B_n,

$$A_0 = \sum_{n=1}^{\infty} B_n \coth\left(\frac{(n-1/2)\pi h}{b}\right)\frac{\sin\left[(n-1/2)\pi a/b\right]}{(n-1/2)\pi a/b} + V_0 , \tag{C5a}$$

$$A_n = \sum_{m=1}^{\infty} B_m \coth\left(\frac{(m-1/2)\pi h}{b}\right) g_{mn}, \ \ g_{mn} = \frac{2}{a}\int_0^a \cos\left(\frac{n\pi y}{a}\right)\cos\left(\frac{(m-1/2)\pi y}{b}\right)dy, \quad n \geq 1 \tag{C5b}$$

Combining Eqs. (C3), (C4b), (C4c) and (C5b), we obtain

$$B_n + \frac{1}{n-1/2}\frac{\rho_2}{\rho_1}\sum_{m=1}^{\infty}\gamma_{nm}B_m \coth\left(\frac{(m-1/2)\pi h}{b}\right) = \frac{2}{(n-1/2)\pi}\frac{\rho_2}{\rho_1}\frac{\sin\left((n-1/2)\pi a/b\right)}{(n-1/2)\pi a/b}, \quad n = 1, 2, 3... \tag{C6}$$

where

$$\gamma_{nm} = \gamma_{mn} = \sum_{l=0}^{\infty} l g_{nl} g_{ml} , \tag{C7}$$

and g_{nl} and g_{ml} is in the form of the last part in Eq. (C5b). Note that in deriving Eq. (C6), we have set $aE_{+\infty} = -1$ for simplicity. It can be shown from Eq. (C6) that, $B_n \propto 1/n^2$ as $n \to \infty$ (c.f. Appendix B above). Thus, by writing Eq. (C6) in an infinite matrix format, B_n can be solved directly with guaranteed convergence.

The total resistance from *EF* to *GH* is $R = (\Phi_F - \Phi_G)/I = V_0/I$, where

$I = \left|2aW(E_{+\infty}/\rho_1)\right| = 2W/\rho_1$ is the total current in the conducting channel, and W is the channel width in the third, ignorable dimension that is perpendicular to the paper. The contact resistance, R_c, is the difference between the total resistance R and the bulk resistance (exterior to $ABCD$) $R_u = \rho_1 L_1/2aW + \rho_2 L_2/2hW$. From Eq. (C1) and (C5a), we find,

$$\begin{aligned} R_c &= \frac{|A_0 - V_0|}{I} - \frac{\rho_2 L_2}{2hW} = \frac{\rho_2}{4\pi W}\bar{R}_c, \\ \bar{R}_c &= \bar{R}_c\left(\frac{a}{b}, \frac{a}{h}, \frac{\rho_1}{\rho_2}\right) \\ &= 2\pi\frac{\rho_1}{\rho_2}\sum_{n=1}^{\infty} B_n \coth\left((n-1/2)\pi h/b\right)\frac{\sin\left((n-1/2)\pi a/b\right)}{(n-1/2)\pi a/b} - \frac{2\pi(b-a)}{h} \end{aligned}, \qquad \text{(C8)}$$

which is the *exact* expression for the contact resistance of Cartesian thin film of dissimilar materials (Fig. 3.1) for arbitrary values of a, b ($b > a$), h, and ρ_1/ρ_2. It appears in Eq. (3.1) of the main text. Given the resistivity ratio ρ_1/ρ_2 and aspect ratios a/h and a/b, the coefficient B_n is solved numerically from Eq. (C6), $\bar{R}_c$ is then obtained from Eq. (C8).

In the limit of $\rho_1/\rho_2 \to \infty$, Eq. (C6) may be simplified to,

$$B_n = \frac{2}{(n-1/2)\pi}\frac{\rho_2}{\rho_1}\frac{\sin\left((n-1/2)\pi a/b\right)}{(n-1/2)\pi a/b}, \qquad n = 1, 2, 3... \qquad \text{(C9)}$$

Thus, from Eq. (C8), $\bar{R}_c$ is found as,

$$\bar{R}_c\left(\frac{a}{b}, \frac{a}{h}\right) = 4\sum_{n=1}^{\infty}\frac{\coth\left((n-1/2)\pi h/b\right)}{n-1/2}\frac{\sin^2\left((n-1/2)\pi a/b\right)}{\left((n-1/2)\pi a/b\right)^2} - 2\pi(b-a)/h, \quad \rho_1/\rho_2 \to \infty \qquad \text{(C10)}$$

which appears as Eq. (3.2) in the main text.

As $h/b \to 0$, Eq. (C10) may be further simplified as

$$\overline{R}_c\left(\frac{a}{b},\frac{a}{h}\right)=\sum_{n=1}^{\infty}\frac{4b/h}{\pi\left(n-1/2\right)^2}\frac{\sin^2\left((n-1/2)\pi a/b\right)}{\left((n-1/2)\pi a/b\right)^2}-\frac{2\pi(b-a)}{h},\quad h/b\to 0,\ \rho_1/\rho_2\to\infty \tag{C11}$$

Figure (C1) plots Eq. (C11), Eq. (C10), and the exact theory of Eq. (C8), in which ρ_1/ρ_2 = 100. We shall show that Eq. (C11) may be simplified to read

$$\overline{R}_c\left(\frac{a}{b},\frac{a}{h}\right)=\frac{2\pi}{3}\left(\frac{a}{h}\right),\quad h/a\to 0,\ \rho_1/\rho_2\to\infty, \tag{C12}$$

for *all* $a/b \le 1$. Equation (C12) is also plotted in Fig. (C1). Note that Eq. (C12) is independent of a/b, a result that cannot be anticipated mathematically from the equivalent expression (C11), even though it is anticipated on physical grounds. We shall now prove that (C12) and (C11) are equivalent.

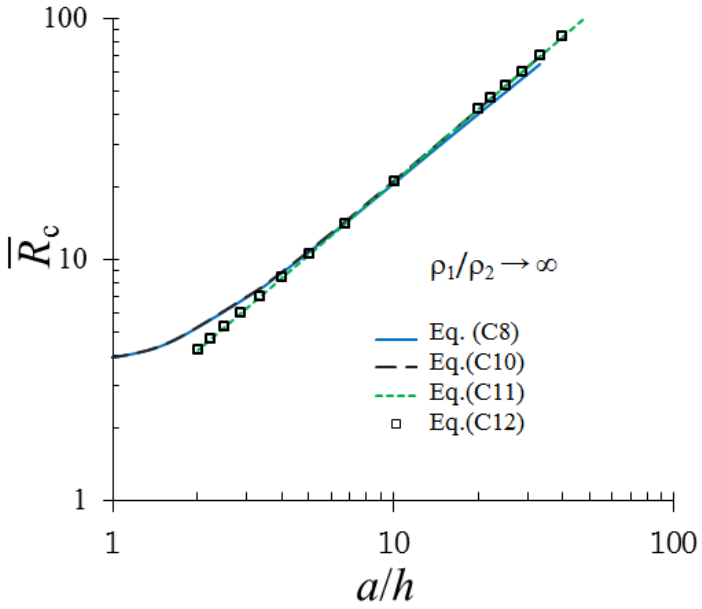

Fig. C1 Comparison of the exact theory Eq. (C8) with ρ_1/ρ_2 = 100 (solid line) and the asymptotic formulas, Eq. (C10), Eq. (C11), and Eq. (C12).

We first write Eq. (C11) as,

$$\begin{aligned}
&\overline{R}_c\left(\frac{a}{b},\frac{a}{h}\right)=2\pi\frac{b}{h}f(x)-\frac{2\pi(b-a)}{h},\quad h/b\to 0,\ \rho_1/\rho_2\to\infty;\\
&f(x)=\sum_{n=1}^{\infty}\frac{2}{\pi^2\left(n-1/2\right)^2}\frac{\sin^2\left[(n-1/2)x\right]}{\left[(n-1/2)x\right]^2},\qquad x\equiv\pi a/b<\pi,
\end{aligned}\tag{C13}$$

where $f(x)$ may be written as

$$\begin{aligned}
&f(x)=\sum_{n=1}^{\infty}\frac{1-\cos\left[(2n-1)x\right]}{\pi^2\left(n-1/2\right)^4x^2}=\frac{16}{\pi^2x^2}\left[k(0)-k(x)\right];\\
&k(x)=\sum_{n=1}^{\infty}\frac{\cos\left[(2n-1)x\right]}{\left(2n-1\right)^4}.
\end{aligned}\tag{C14}$$

Differentiating $k(x)$ we get,

$$\frac{dk(x)}{dx}=-\sum_{n=1}^{\infty}\frac{\sin\left[(2n-1)x\right]}{\left(2n-1\right)^3}=-\left(\frac{\sin x}{1^3}+\frac{\sin 3x}{3^3}+\frac{\sin 5x}{5^3}+\ldots\right).\tag{C15}$$

From Problem 38 (and 34a) of Chapter 5 of Hildebrand [p. 252 of Ref. 92], we know that

$$x(\pi-x)=\frac{8}{\pi}\left(\frac{\sin x}{1^3}+\frac{\sin 3x}{3^3}+\frac{\sin 5x}{5^3}+\ldots\right),\qquad 0<x<\pi\,.\tag{C16}$$

Inserting Eq. (C16) into Eq. (C15), we have

$$\frac{dk(x)}{dx}=-\frac{\pi}{8}x(\pi-x),\qquad 0<x<\pi\,,\tag{C17}$$

which is easily integrated,

$$k(x)=-\frac{\pi^2}{16}x^2+\frac{\pi}{24}x^3+k(0),\qquad 0<x<\pi\,.\tag{C18}$$

Insert (C18) into the first equation of Eq. (C14) to obtain,

$$f(x)=1-\frac{2}{3\pi}x,\qquad 0<x<\pi\,.\tag{C19}$$

Inserting Eq. (C19) into the first equation of Eq. (C13), we obtain Eq. (C12).

Appendix D

Conformal mapping for Cartesian thin film contact with uniform resistivity

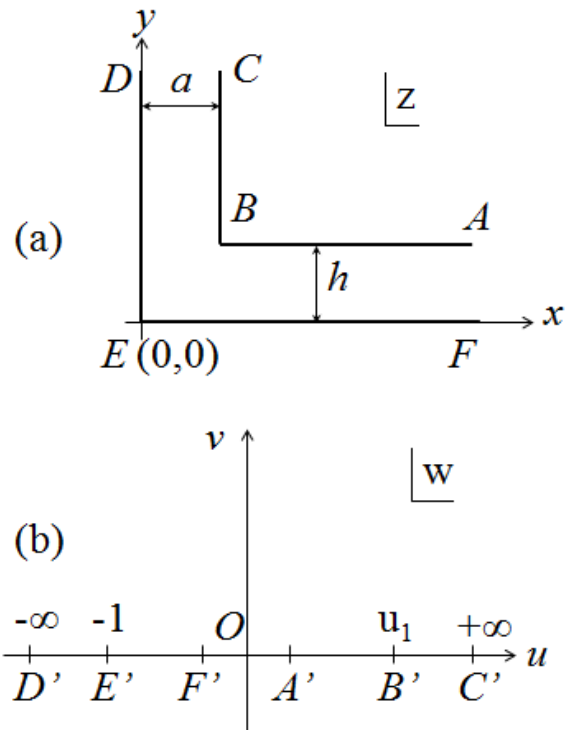

Fig. D1 (a) The half thin film geometry in the z ≡ (x, y) plane, (b) its map onto the w ≡ [u,v] plane.

Due to symmetry, we consider only the right half of the Cartesian thin film geometry with uniform resistivity (Fig. 3.1 with $\rho_1 = \rho_2$). We represent in the *x*-*y* plane the top boundary ABC, the midplane DE ($x = 0$), and the bottom boundary EF, as shown in Fig.

D1(a). The top channel has half width *a*, and the bottom channel has width *h*. The two boundaries, ABC and DEF are streamlines. We solve the current flow of this Cartesian geometry by conformal mapping between the complex z- and w-planes where $z = x+iy = (x, y)$ and $w = u+iv = [u, v]$. Following Refs. [9] and [23], we denote this mapping as $(x, y) \leftrightarrow [u, v]$ henceforth [Fig. D1 (b)]. Specifically, the maps of ABCDEF in Fig. D1 are, sequentially, $(\infty, h) \leftrightarrow [0^+, 0]$, $(a, h) \leftrightarrow [u_1, 0]$, $(a, \infty) \leftrightarrow [\infty, 0]$, $(0, \infty) \leftrightarrow [-\infty, 0]$, $(0, 0) \leftrightarrow [-1, 0]$, and $(\infty, 0) \leftrightarrow [0^-, 0]$. In the maps *A'* and *F'*, 0^+ and 0^- denote values slightly greater and less than zero, respectively. This map is governed by the Schwarz–Christoffel transformation [92]

$$z(w) = K\int_{-1}^{w} dw f(w) + (0 + i0), \tag{D1a}$$

$$f(w) = \frac{1}{w}\sqrt{\frac{w-u_1}{w+1}}, \tag{D1b}$$

In Eq. (D1), the constants u_1 is real and positive, and *K* is another constant to be determined below. Branch cuts [not shown in Fig. D1(b)] extending downward from the two branch points, w = -1 and u_1, render $f(w)$ single valued in the upper half w-plane. Evaluating z(w) at the points *F* and *A*, and subtracting, we obtain,

$$ih = K\int_{0^-}^{0^+} \frac{dw}{w}\sqrt{\frac{w-u_1}{w+1}} = K\pi\sqrt{u_1}, \tag{D2}$$

Evaluating z(w) at point *B*, we obtain

$$a + ih = K\int_{-1}^{u_1} \frac{dw}{w}\sqrt{\frac{w-u_1}{w+1}} = K\pi\left(-i + \sqrt{u_1}\right) = \frac{h}{\sqrt{u_1}} + ih, \tag{D3}$$

where we have used Eq. (D2). From Eq. (D3) we have,

$$\frac{a}{h}=\frac{1}{\sqrt{u_1}}, \qquad K=\frac{ia}{\pi}. \tag{D4}$$

The complex electrostatic potential is $\Phi(w)=K(iE_0)\ln(w)=\phi+i\psi$. It represents a source at the origin of the *w*-plane which produces a constant electric field (iE_0) far away from the constriction corner along the *y*-axis in the *z*-plane [Fig. D1(a)]. To see this, the components E_x and E_y of the electrostatic field in the (*x*, *y*) plane may be expressed as [92]

$$E_x-iE_y=-\frac{d\Phi}{dz}=\frac{d\Phi/dw}{dz/dw}=-iE_0\sqrt{\frac{w+1}{w-u_1}}, \tag{D5}$$

where we have used Eq. (D1) for *dz*/*dw*. Equation (D5) clearly shows a constant electric field $-iE_0$ (= E_C) at $w = \infty$ and $-E_0/\sqrt{u_1}$ (= E_A) at $w = 0$, e.g., at the location *C*(*C'*) and *A*(*A'*) in Fig. D1. Due to the continuity of current, $I = E_A hW/\rho = E_C aW/\rho$, where *W* is the third ignorable dimension, we have $a/h=1/\sqrt{u_1}$, which is Eq. (D4) obtained directly from the mapping function, Eq. (D1).

We shall next derive the total resistance (therefore, the contact resistance) for the thin film constriction shown in Fig. D1(a). For the time being, let us consider points *A* and *C* to be finite in the *z*-plane [Fig. D1(a)], with the respective maps for *A*: $z_A = (x_A , h) \leftrightarrow (u_A, 0)$, and for *C*: $z_C = (a, y_C) \leftrightarrow (u_C, 0)$. The voltage drop from *A* to *C* is $V= K(iE_0)\ln(u_A/u_C)$ from the complex potential Φ. The total resistance between *A* and *C* is then $R = V/I = |[K(iE_0)\ln(u_A/u_C)]/ [-iE_0 aW/\rho]| = (\rho/\pi W)\ln(u_A/u_C)$. We may next express this total resistance as $R = R_{u1} + R_{u2} + R_c$, where R_{u1} is the resistance between *B* and *C*, R_{u2} is the resistance between *A* and *B*, and R_c is the remainder that is solely due to the constriction

of the channel. From this definition, $R_{u1} = |\rho(z_C\text{-}z_B)/aW|$, and $R_{u2} = |\rho(z_A\text{-}z_B)/aW|$ where z_A, z_B and z_C are given in terms of the integral in Eq. (D1), evaluated respectively, at w = $[u_A, 0]$, w = $[u_B, 0]$, and at w = $[u_C, 0]$. Upon taking the limit $u_C \to +\infty$, and $u_A \to 0^+$, we obtain the real integral for the contact resistance $R_c = R - (R_{u1} + R_{u2})$ as

$$R_c = \frac{\rho}{4\pi W}\bar{R}_c, \qquad \bar{R}_c = 4\left\{\int_0^{u_1}\frac{dw}{w}\left[1-\frac{1}{\sqrt{u_1}}\sqrt{\frac{u_1-w}{w+1}}\right]+\int_{u_1}^{\infty}\frac{dw}{w}\left[1-\sqrt{\frac{w-u_1}{w+1}}\right]\right\}, \qquad \text{(D6)}$$

which may be simplified upon carrying out the integrals,

$$\bar{R}_c\left(\frac{a}{h}\right) = 8\ln\left[\frac{1}{4}\left(\frac{a}{h}+\frac{h}{a}\right)\right]+8\left(\frac{h}{a}\right)\tan^{-1}\left(\frac{a}{h}\right)+8\left(\frac{a}{h}\right)\tan^{-1}\left(\frac{h}{a}\right). \qquad \text{(D7)}$$

For the Cartesian geometry shown in Fig. 3.1, the total resistance (therefore the contact resistance) is half of that shown in Fig. D1. Thus, the contact resistance for the geometry in Fig. 3.1 is half of the value in Eq. (D7),

$$\bar{R}_c\left(\frac{a}{h}\right) = 4\ln\left[\frac{1}{4}\left(\frac{a}{h}+\frac{h}{a}\right)\right]+4\left(\frac{h}{a}\right)\tan^{-1}\left(\frac{a}{h}\right)+4\left(\frac{a}{h}\right)\tan^{-1}\left(\frac{h}{a}\right), \qquad \text{(D8)}$$

which is Eq. (3.4) of the main text.

Appendix E

The contact resistance of thin film to rod geometry

Referring to Fig. 3.1, similar to the Cartesian case, we also assume that $L_1 >> a$, so that the current flow is uniform at the end *GH*, far from the joint region. The solutions of Laplace's equation in the cylindrical geometry are [20, 25, 29],

$$\begin{aligned}
&\Phi_+(r,z) = A_0 + \sum_{n=1}^{\infty} A_n J_0\left(\alpha_n r\right) e^{-\alpha_n z} - E_{+\infty} z, \qquad z > 0, r \in (0,a); \\
&\Phi_-(r,z) = V_0 + \sum_{n=1}^{\infty} \left[B_n \sinh\left(\frac{\lambda_n z}{b}\right) + C_n \cosh\left(\frac{\lambda_n z}{b}\right) \right] J_0\left(\frac{\lambda_n r}{b}\right), \qquad z < 0, r \in (0,b),
\end{aligned} \tag{E1}$$

where Φ_+ and Φ_- are the electrical potential in the region *BCHG* and *BCEF* respectively, $E_{+\infty}$ is the uniform electric fields at the end *GH*, V_0 is the electrical potential at the thin film rim *E* and *F* ($r = b$), $J_0(x)$ is the zeroth order of the Bessel function of first kind, α_n and λ_n satisfy $J_1(\alpha_n a) = J_0(\lambda_n) = 0$, and A_n and B_n are the coefficients that need to be solved.

Since the current flows parallel to the thin film boundary *EF*, we have

$$\frac{\partial \Phi_-}{\partial z} = 0, \qquad z = -h, r \in (0,b), \tag{E2}$$

which leads to

$$C_n = B_n \coth\left(\frac{\lambda_n h}{b}\right). \tag{E3}$$

At the interface $z = 0$, from the continuity of electrical potential and current density, we have the following boundary conditions,

$$\Phi_+ = \Phi_-, \qquad z = 0, r \in (0, a), \tag{E4a}$$

$$\frac{1}{\rho_1}\frac{\partial \Phi_+}{\partial z} = \frac{1}{\rho_2}\frac{\partial \Phi_-}{\partial z}, \qquad z = 0, \;\; r \in (0, a), \tag{E4b}$$

$$\frac{\partial \Phi_-}{\partial z} = 0, \qquad z = 0, \; r \in (a, b). \tag{E4c}$$

From Eqs. (E1) and (E4a), the coefficient A_n is expressed in terms of B_n,

$$A_0 = \sum_{n=1}^{\infty} B_n \coth\left(\frac{\lambda_n h}{b}\right)\frac{2J_1(\lambda_n a/b)}{\lambda_n a/b} + V_0, \tag{E5a}$$

$$A_n = \sum_{m=1}^{\infty} B_m \coth\left(\frac{\lambda_m h}{b}\right) g_{mn}, \;\; g_{mn} = \frac{2}{a^2 J_0^2(\alpha_n a)}\int_0^a r dr J_0(\alpha_n r) J_0\left(\frac{\lambda_m r}{b}\right), \quad n \geq 1. \tag{E5b}$$

Combining Eqs. (E3), (E4b), (E4c) and (E5b), we obtain

$$B_n + \frac{\rho_2}{\rho_1}\frac{a}{b}\frac{1}{\lambda_n J_1^2(\lambda_n)}\sum_{m=1}^{\infty}\gamma_{nm} B_m \coth\left(\frac{\lambda_m h}{b}\right) = \frac{\rho_2}{\rho_1}\frac{2J_1(\lambda_n a/b)}{\lambda_n^2 J_1^2(\lambda_n)}, \qquad n = 1, 2, 3..., \tag{E6}$$

where

$$\gamma_{nm} = \gamma_{mn} = \sum_{l=1}^{\infty} g_{nl} g_{ml} \alpha_l a J_0^2(\alpha_l a), \tag{E7}$$

and g_{nl} and g_{ml} is in the form of the last part in Eq. (E5b). Note that in deriving Eq. (E6), we have set $aE_{+\infty} = -1$ for simplicity. It can be shown from Eq. (E6) that, $B_n \propto 1/\lambda_n^2 \propto 1/n^2$ as $n \to \infty$ (c.f. Appendix A). Thus, by writing Eq. (E6) in an infinite matrix format, B_n can be solved directly with guaranteed convergence.

The total resistance from *EF* to *GH* is $R = (\Phi_F - \Phi_G)/I = V_0/I$, where $I = \left|\pi a^2 (E_{+\infty}/\rho_1)\right| = \pi a/\rho_1$ is the total current in the conducting channel. The contact

resistance, R_c, is the difference between the total resistance R and bulk resistance (exterior to $ABCD$) $R_u = \rho_1 L_1 / \pi a^2 + (\rho_2 / 2\pi h)\ln(b/a)$. From Eq. (E1) and (E5a), we find,

$$R_c = \frac{|A_0 - V_0|}{I} - \frac{\rho_2}{2\pi h}\ln\left(\frac{b}{a}\right) = \frac{\rho_2}{4a}\bar{R}_c,$$

$$\bar{R}_c\left(\frac{a}{b}, \frac{a}{h}, \frac{\rho_1}{\rho_2}\right) = \frac{8}{\pi}\frac{\rho_1}{\rho_2}\sum_{n=1}^{\infty} B_n \coth\left(\lambda_n h/b\right)\frac{J_1\left(\lambda_n a/b\right)}{\lambda_n a/b} - \frac{2a}{\pi h}\ln\left(\frac{b}{a}\right), \tag{E8}$$

which is the *exact* expression for the contact resistance between a thin film and a coaxial rod of dissimilar materials (Fig. 3.1) for arbitrary values of a, b ($b > a$), h, and ρ_1/ρ_2. It appears in Eq. (3.9) of the main text. Given the resistivity ratio ρ_1/ρ_2 and aspect ratios a/h and a/b, the coefficient B_n is solved numerically from Eq. (E6), $\bar{R}_c$ is then obtained from Eq. (E8).

In the limit of $\rho_1/\rho_2 \to \infty$, Eq. (E6) may be simplified,

$$B_n = \frac{\rho_2}{\rho_1}\frac{2J_1\left(\lambda_n a/b\right)}{\lambda_n^2 J_1^2\left(\lambda_n\right)}, \qquad n = 1, 2, 3... \tag{E9}$$

Thus, from Eq. (E8), $\bar{R}_c$ is found as,

$$\bar{R}_c\left(\frac{a}{b}, \frac{a}{h}\right) \cong \frac{16}{\pi}\sum_{n=1}^{\infty}\frac{J_1^2(\lambda_n a/b)}{\lambda_n a/b}\frac{\coth(\lambda_n h/b)}{\lambda_n^2 J_1^2(\lambda_n)} - \frac{2a}{\pi h}\ln(b/a), \quad \rho_1/\rho_2 \to \infty, \tag{E10}$$

which appears as Eq. (3.10) in the main text.

As $h/b \to 0$, Eq. (E10) may be further simplified to read

$$\bar{R}_c\left(\frac{a}{b}, \frac{a}{h}\right) \cong \frac{16}{\pi}\sum_{n=1}^{\infty}\frac{J_1^2(\lambda_n a/b)}{\lambda_n a/b}\frac{1}{\lambda_n h/b}\frac{1}{\lambda_n^2 J_1^2(\lambda_n)} - \frac{2a}{\pi h}\ln(b/a), \quad h/b \to 0, \rho_1/\rho_2 \to \infty. \tag{E11}$$

Figure (E1) plots Eq. (E11), Eq. (E10), and the exact theory Eq. (E8) in which $\rho_1/\rho_2 = 100$. If $b >> h$ or $b >> a$, the exact theory, Eq. (E8) becomes independent of b [cf. Fig. 3.10].

We propose that, Eq. (E11) is equivalent to

$$\overline{R}_c\left(\frac{a}{b},\frac{a}{h}\right)=\frac{1}{2\pi}\frac{a}{h},\quad h/a\to 0,\rho_1/\rho_2\ \to\infty, \tag{E12}$$

for *all* $b/a \geq 1$. Equation (E12) may be readily compared with Eq. (C12) which is proved in Appendix C. The equivalence of Eqs. (E11) and (E12) is evident in Fig. (E1).

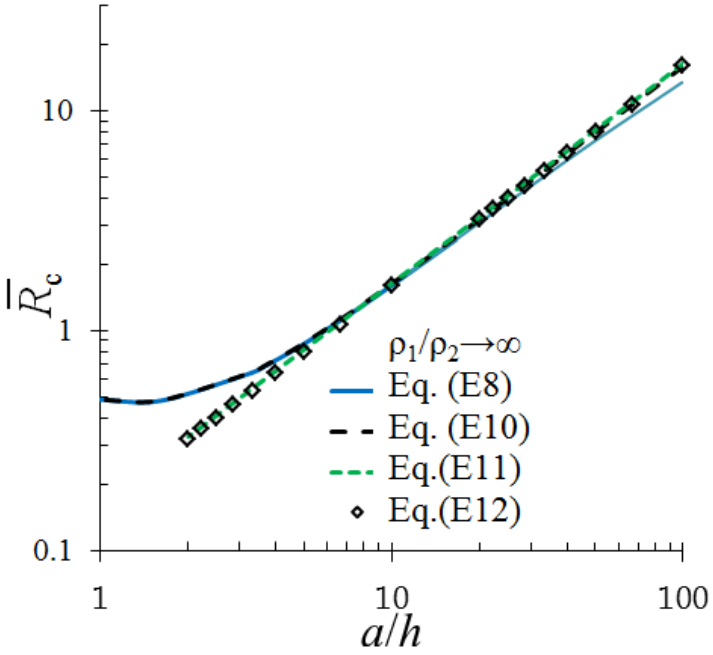

Fig. E1 Comparison of the exact theory Eq. (E8) with $\rho_1/\rho_2 = 100$, and the asymptotic formulas, Eq. (E10), Eq. (E11) and Eq. (E12).

References

1. E. P. Degarmo, J. T. Black, R. A. Kohser, *Materials and Processes in Manufacturing* (Wiley, 9th ed., 2003).

2. M. R. Gomez, J. C. Zier, R. M. Gilgenbach, D. M. French, W. Tang, and Y. Y. Lau, "Effect of soft metal gasket contacts on contact resistance, energy deposition, and plasma expansion profile in a wire array Z pinch", *Rev. Sci. Inst.* **79**, 093512 (2008).

3. W. Tang, "Theoretical analysis of some contemporary issues on wire-array z-pinch", Ph.D. thesis, University of Michigan, 2009.

4. J. Zier, M. R. Gomez, D. M. French, R. M. Gilgenbach, Y. Y. Lau, W. Tang, M. E. Cuneo, T. A. Mehlhorn, M. D. Johnston, M. G. Mazarakis, "Wire-tension effects of plasma dynamics in a two-wire Z-pinch," *IEEE Trans. Plasma Science* **36**, 1284-1285 (2008); D. A. Chalenski, B. R. Kusse, and J. B. Greenly, "Soldered contact and current risetime effects on negative polarity wire array Z pinches", *Phys. Plasmas* **16**, 082707 (2009).

5. R. M. Gilgenbach, Y. Y. Lau, H. McDowell, K. L. Cartwright, and T. A. Spencer, "Crossed-Field Devices", in *Modern Microwave and Millimeter Wave Power Electronics*, Chap. 6, edited by R.J. Barker, N.C. Luhmann, J.H. Booske, and G.S. Nusinovich, IEEE Press, Piscataway, NJ 2004; B. Hoff, "Magnetic Priming of a Relativistic Magnetron", Ph. D. thesis, University of Michigan, 2009; D. M. French, "Investigation of Novel Configurations for High Power Microwave Generation", Ph. D. thesis, University of Michigan, 2011.

6. N. M. Jordan, "Laser fabrication of high-k dielectrics for high current cathodes", Ph. D. thesis, University of Michigan, 2008.

7. V. Latham, *High Voltage Vacuum Insulation* (Academic Press, London, UK, 1995).

8. N. M. Jordan, Y. Y. Lau, D. M. French, R. M. Gilgenbach, and P. Pengvanich, "Electric field and electron orbits near a triple point", *J. Appl. Phys.* **102**, 033301 (2007); N. Jordan, R. M. Gilgenbach, B. W. Hoff, and Y. Y. Lau, "Metal-oxide-junction, triple point cathodes in a relativistic magnetron", *Rev. Sci. Instrum*. **79**, 064705 (2008).

9. R. Miller, Y. Y. Lau, and J. H. Booske, "Electric field distribution on knife-edge field emitters", *Appl. Phys. Lett.* **91**, 074105 (2007).

10. H. L. Bosman, "Investigation of failure mechanisms in high-power microwave transmission windows", Ph.D. thesis, University of Michigan, 2004.

11. P. Zhang, Y. Y. Lau, and R. M. Gilgenbach, "Analysis of radio-frequency absorption and electric and magnetic field enhancements due to surface roughness", *J. Appl. Phys.* **105**, 114908 (2009).

12. R. Holm, *Electric Contact* (Springer-Verlag, Berlin, ed. 4, 1967).

13. P. G. Slade, *Electrical contacts – principles and applications* (Dekker, New York, 1999).

14. J. A. Greenwood, "Constriction resistance and the real area of contact", *Brit. J. Appl. Phys.* **17**, 1621 (1966).

15. A. M. Rosenfeld, and R. S. Timsit, "The potential distribution in a constricted cylinder: An exact solution", *Quart. Appl. Math*. **39,** 405 (1981); R. S. Timsit, "Electrical contact resistance: properties of stationary interfaces", *IEEE Trans. Compon. Packag. Technol*. **22**, 85 (1999).

16. P. M. Hall, "Resistance calculations for thin film patterns", *Thin Solid Films* **1**, 277 (1967).

17. P. M. Hall, "Resistance calculations for thin film rectangles", *Thin Solid Films* **300**, 256 (1997).

18. Y. H. Jang, and J. R. Barber, "Effect of contact statistics on electrical contact resistance", *J. Appl. Phys.* **94**, 7215 (2003).

19. M, Nakamura, "Constriction resistance of conducting spots by the boundary element method", *IEEE Trans. Compon., Hybrids, Manuf. Technol.* **16**, 339 (1993).

20. R. Timsit, "Constriction resistance of thin-film contacts," *IEEE Trans. Compon. Packag. Technol.*, **33**, 636 (2010).

21. M. B. Read, J. H. Lang, A. H. Slocum, and R. Martens, "Contact resistance in flat thin films", *Proc. of the 55th IEEE Holm Conf. on Electrical Contacts*, pp. 303 - 309 (2009).

22. G. Norberg, S. Dejanovic, and H. Hesselbom, "Contact resistance of thin metal film contacts", *IEEE Trans. Compon. Packag. Technol*. **29**, 371 (2006).

23. Y. Y. Lau, and W. Tang, "A higher dimensional theory of electrical contact resistance", *J. Appl. Phys.* **105**, 124902 (2009).

24. M. R. Gomez, D. M. French, W. Tang, P. Zhang, Y. Y. Lau, and R. M. Gilgenbach, "Experimental validation of a higher dimensional theory of electrical contact resistance", *Appl. Phys. Lett*. **95**, 072103 (2009).

25. P. Zhang and Y. Y. Lau, "Scaling laws for electrical contact resistance with dissimilar materials", *J. Appl. Phys.* **108**, 044914 (2010). There is a typo in this paper. In Eq. (6) of this paper, the term $-2.2281(a/b)^2$ in $g(b/a)$ should read $-1.2281(a/b)^2$.

26. P. Zhang, Y. Y. Lau, W. Tang, M. R. Gomez, D. M. French, J. C. Zier, and R. M. Gilgenbach, "Contact resistance with dissimilar materials: bulk contacts and thin film contacts", *Proc. of the 57th IEEE Holm Conf. on Electrical Contacts*, paper no. 2.2, pp. 31 – 36, 2011.

27. M. W. Denhoff, "An accurate calculation of spreading resistance", *J. Phys. D: Appl. Phys.* **39**, 1761 (2006).

28. P. Zhang, Y. Y. Lau and R. M. Gilgenbach, "Minimization of thin film contact resistance", *Appl. Phys. Lett.* **97**, 204103 (2010).

29. P. Zhang, Y. Y. Lau, and R. M. Gilgenbach, "Thin film contact resistance with dissimilar materials", *J. Appl. Phys.* **109**, 124910 (2011).

30. P. Zhang, Y. Y. Lau, and R. S. Timsit, "On the Spreading Resistance of Thin-Film Contacts", *IEEE Trans. Electron Devices* **59**, 1936 (2012).

31. P. U. Duselis, J. A. Vaughan, and B. R. Kusse, "Factors affecting energy deposition and expansion in single wire low current experiments," *Phys. Plasmas* **11**, 4025 (2004).

32. T. W. L. Sanford, R. C. Mock, J. F. Seaman, M. R. Lopez, R. G. Watt, G. C. Idzorek, and D. L. Peterson, "Wire fixturing in high wire-number z pinches critical for high radiation power and reproducibility," *Phys. Plasmas* **12**, 122701 (2005).

33. J. Zier, "Ablation dynamics and instabilities of metallic plasmas generated using mega-ampere-scale current drivers", Ph.D. thesis, University of Michigan, 2011.

34. M. R. Gomez, "Experimental Examination of Plasma Formation and Current Loss in Post-Hole Convolutes", Ph.D. thesis, University of Michigan, 2011.

35. M. E. Cuneo, R. A. Vesey, J. L. Porter, G. A. Chandler, D. L. Fehl, T. L. Gilliland, D. L. Hanson, J. S. McGurn, P. G. Reynolds, L. E. Ruggles, H. Seamen, R. B. Spielman, K. W. Struve, W. A. Stygar, W. W. Simpson, J. A. Torres, D. F. Wenger, J. H. Hammer, P. W. Rambo, D. L. Peterson, and G. C. Idzorek, "Development and characterization of a Z-pinch-driven hohlraum high-yield inertial confinement fusion target concept Development and characterization of a Z-pinch-driven hohlraum high-yield inertial confinement fusion target concept", *Phys. Plasmas* **8**, 2257 (2001).

36. A. Ahnood, K. Ghaffarzadeh, A. Nathan, P. Servati, F. Li, M. R. Esmaeili-Rad, and A. Sazonov, "Non-ohmic contact resistance and field-effect mobility in nanocrystalline silicon thin film transistors", *Appl. Phys. Lett.* **93**, 163503 (2008).

37. H. Klauk, G. Schmid, W. Radlik, W. Weber, L. Zhou, C. D. Sheraw, J. A. Nichols, and T. N. Jackson, "Contact resistance in organic thin film transistors", *Solid-State Electronics* **47**, 297 (2003).

38. G. H. Gelinck, T. C. T. Geuns, and D. M. de Leeuw, "High-performance all-polymer integrated circuits", *Appl. Phys. Lett.* **77**, 1487 (2000).

39. W. J. Greig, *Integrated Circuit Packaging, Assembly and Interconnections*, (Springer, New York, 2007).

40. J. L. Carbonero, G. Morin, and B. Cabon, "Comparison between beryllium-copper and tungsten high frequency air coplanar probes", *IEEE Trans. Microwave Theory Tech.* **43**, 2786 (1995).

41. R. H. Baughman, A. A. Zakhidov, and W. A. de Heer, “Carbon nanotubes - the route toward applications”, *Science* **297**, 787 (2002).

42. D. Shiffler, T. K. Statum, T. W. Hussey, O. Zhou, and P. Mardahl, in *Modern Microwave and Millimeter Wave Power Electronics*, R. J. Barker, N. C. Luhmann, J. H. Booske, G. S. Nusinovich, Eds. (IEEE Press, Piscataway, NJ, 2005), chap. 13, p. 691.

43. V. Vlahos, J. H. Booske, and D. Morgan, “Ab initio study of the effects of thin CsI coatings on the work function of graphite cathodes”, *Appl. Phys. Lett*. **91**, 144102 (2007).

44. W. Wu, S. Krishnan, T. Yamada, X. Sun, P. Wilhite, R. Wu, K. Li, and C. Y. Yang, “Contact resistance in carbon nanostructure via interconnects”, *Appl. Phys. Lett*. **94**, 163113 (2009).

45. Z. Yao, C. L. Kane, and C. Dekker, “High-Field Electrical Transport in Single-Wall Carbon Nanotubes”, *Phys. Rev. Lett*. **84**, 2941 (2000).

46. D. Mann, A. Javey, J. Kong, Q. Wang, and H. Dai, “Ballistic Transport in Metallic Nanotubes with Reliable Pd Ohmic Contacts”, *Nano Lett.* **3**, 1541 (2003).

47. International Technology Roadmap for Semiconductors - Interconnect, available at http://www.itrs.net/Links/2007ITRS/2007_Chapters/2007_Interconnect.pdf

48. J. Oberhammer, “Novel RF MEMS switch and packaging concepts,” Ph.D. dissertation, Roy. Inst. Technol., Stockholm, Sweden, 2004.

49. D. Hyman and M. Mehregany, “Contact physics of gold microcontacts for MEMS switches,” *IEEE Trans. Compon. Packag. Technol.* **22**, 357–364 (1999).

50. Y. H. Song, D. H. Choi, H. H. Yang, and J. B. Yoon, “An extremely low contact-resistance MEMS relay using meshed drain structure and soft insulating layer”, *J. Microelectromech. Syst.* **20**, 204 (2011).

51. P. Bruzzone, B. Stepanov, R. Dettwiler, and F. Staehli, “Results of Contact Resistance Distribution in NbTi and Nb3Sn ITER Conductor Termination”, IEEE Trans. Appl. Superconductivity **17**, 1378 (2007).

52. A. Nijhuis, Y. Ilyin, W. Abbas, B. ten Haken, and H. H. J. ten Kate, "Change of interstrand contact resistance and coupling loss in various prototype ITER NbTi conductors with transverse loading in the Twente Cryogenic Cable Press up to 40,000 cycles", *Cryogenics* **44**, 319 (2004).

53. V. Shemelin and H. Padamsee, "Magnetic field enhancement at pits and pumps on the surface of superconducting cavities," SRF 080903-04, TESLA 2008.

54. J. H. Booske, "Plasma physics and related challenges of millimeter- wave-to-terahertz and high power microwave generation", *Phys. Plasmas* **15**, 055502 (2008).

55. VI. V. Bobkov, J.-M. Noterdaeme, and R. Wilhelm, "Properties of field emission from high voltage RF antenna", *Surf. Coat. Technol.* **200**, 822 (2005).

56. J. B. O. Caughman, C. Castano-Giraldo, M. Aghazarian, F, W. Baity, D. A. Rasmussen, and D. N. Ruzic, "Study of RF Breakdown Mechanisms Relevant to an ICH Antenna Environment", *AIP Conf. Proc.* **933**, 195 (2007).

57. Y. Iwashita and Y. Tajima, "Development of high resolution camera for observations of superconducting cavities", *Rev. ST Accel. Beams* **11**, 093501 (2008).

58. Y. Iwashita and T. Higo, "Evaluation of magnetic field enhancement along a boundary", TUP95, Proc. LINAC 2004.

59. M.Petelin, J. Hirshfield, Y. Y. Danilov, S. Kuzikov, V. Pavelyev, D. Schegolkov, and A. Yunakovsky, "Components for Quasi-Optically-Fed Linear Accelerators", *AIP Conf. Proc.* **807**, 408 (2006).

60. G. P. Scheitrum, in *Modern Microwave and Millimeter-Wave Power Electronics*, Eds.: R. J. Barker, J. H. Booske, N. C. Luhmann Jr. and G. S. Nusinovich, (IEEE Press, Piscataway, New Jersey, 2005), Ch. 7, p.343.

61. H. Pandit, D. Shi, N. H. Babu, X. Chaud, D. A. Cardwell, P. He, D. Isfort, R. Tournier, D. Mast, and A. M. Ferendeci, "High T_c superconductor re-entrant cavity filter structures", *Physica C* **425**, 44 (2005).

62. V. A. Dolgashev and S. G. Tantawi, "Effect of RF Parameters on Breakdown Limits in High-Vacuum X-Band Structures", *AIP Conf. Proc.* **691**,151 (2003).

63. D. P. Pritzkau, R. H. Siemann, "Experimental study of rf pulsed heating on oxygen free electronic copper", *Phys. Rev. ST Accel. Beams* **5**, 112002 (2002).

64. D. P. Pritzkau, *RF Pulse Heating*, Ph.D. thesis, Stanford University, 2001, SLAC-0577.

65. W. Wuensch, "CLIC 30 GHz Accelerating Structure Development", *AIP Conf. Proc.* **647**, 506 (2002).

66. H. Padamsee, "The science and technology of superconducting cavities for accelerators", *Supercond. Sci. Technol*. **14**, R28 (2001).

67. H. Padamsee, J. Knobloch, T. Hays, *RF Superconductivity for Accelerators* (John Wiley & Sons, 1998).

68. E. W. Collings, M. D. Sumption and T. Tajima, "Magnesium diboride superconducting RF resonant cavities for high energy particle acceleration", *Supercond. Sci. Technol*. **17**, S595 (2004).

69. J. J. Song, S. Bajikar, Y. W. Kang, R. L. Kustom, D. C. Mancini, A. Nassiri, and B. Lai, "LIGA fabrication of mm-wave accelerating cavity structures at the advanced photon source (APS)", Proc. IEEE PAC97 (Vancouver, 1997), p.461.

70. M. J. Lancaster, *Passive Microwave Device Applications of High-Temperature Superconductors* (Cambridge University Press, Cambridge, 1997).

71. Z. Zhai, C. Kusko, N. Hakim, and S. Sridhar, "Precision microwave dielectric and magnetic susceptibility measurements of correlated electronic materials using superconducting cavities", *Rev. Sci. Instrum.* **71**, 3151 (2000).

72. L. K. Ang, Y. Y. Lau, R. M. Gilgenbach, and H. L. Spindler, "Analysis of laser absorption on a rough metal surface", *Appl. Phys. Lett.* **70**, 6 (1997).

73. T. Sun, B. Yao, A. P. Warren, K. Barmak, M. F. Toney, R. E. Peale, and K. R. Coffey, "Dominant role of grain boundary scattering in the resistivity of nanometric Cu films", *Phys. Rev. B* **79**, 041402(R) (2009).

74. K. L. Jensen, Y. Y. Lau, D. W. Feldman, and P. G. O'Shea, "Electron emission contributions to dark current and its relation to microscopic field enhancement and heating in accelerator structures", *Phys. Rev. ST Accel. Beams* **11**, 081001 (2008).

75. P. Wilson, “Formation of Taylor cones on a molten metal surface followed by ion injection into the vacuum”, The US High Gradient Research Collaboration Workshop, Menlo Park, CA (2007).

76. A. S. Gilmour, *Microwave Tubes* (Artech House Publishers, Dedham, MA, 1986).

77. A.T. Wu, S. Jin, X.Y Lu, R.A. Rimmer, J. Mammosser, and K. Zhao, “Fastest electropolishing technique on niobium for particle accelerators”, MOPC119 Proceedings of IPAC2011, San Sebastián, Spain.

78. X. Gu, L. Tsang, and H. Braunisch, “Modeling effects of random rough interface on power absorption between dielectric and conductive medium in 3-D problem”, *IEEE Trans. Microw. Theory Tech.* **55**, 511(2007).

79. G. Brist, S. Hall, S. Clouser, T. Liang, “Non-classical conductor losses due to copper foil roughness and treatment”, S19-2, ECWC 10 Conference at IPC Printed Circuits Expo, SMEMA Council APEX and Designers Summit 05.

80. H. Tanaka and F. Okada, “Precise measurements of dissipation factor in microwave printed circuit boards,” *IEEE Trans. Instrum. Meas.* **38**, 509-514 (1989).

81. S. P. Morgan, “Effect of surface roughness on eddy current losses at microwave frequencies,” *J. Appl. Phys.* **20**, 352–362 (1949).

82. A. F. Horn III, J. W. Reynolds, P. A. LaFrance, J. C. Rautio, “Effect of conductor profile on the insertion loss, phase constant, and dispersion in thin high frequency transmission lines”, DesignCon 2010, Santa Clara, CA (2010).

83. M. V. Lukic, and D. S. Filipovic, “Modeling of 3-D Surface Roughness Effects with Application to μ-Coaxial Lines”, *IEEE Trans. Microw. Theory Tech.* **55**, 518 (2007).

84. S. Groiss, I. Bardi, O. Biro, K. Preis and K.R. Richter, “Parameters of Lossy Cavity Resonators Calculated by the Finite Element Method”, *IEEE Trans. Magnetics* **32**, 894 (1996).

85. See, http://www.ansoft.com, for both HFSS and MAXWELL codes. For the electrostatic problem in this thesis, MAXWELL 2-D uses automatic meshing and finite element analysis to solve the Laplace equation.

86. Microwave Engineers Handbook, Vol. Two (Artech House, 1971) p.186.

87. C. L. Holloway and E. F. Kuester, "Power loss associated with conducting and superconducting rough interfaces," *IEEE Trans. Microw. Theory Tech.* **48**, 1601-1610 (2000).

88. A. Matsushima and K. Nakata, "Power loss and local surface impedance associated with conducting rough interfaces," *Elect. Commun. Jpn.* **89**, 1-10 (2006).

89. M. A. Biot, "Some new aspects of the reflection of electromagnetic waves on a rough surface, *J. Appl. Phys.* **28**, 1455-1463 (1957).

90. J. R. Wait, "Guiding of electromagnetic waves by uniformly rough surfaces", *part I, IRE Trans. Antennas. Propagat.* **7**, S154–S162 (1959).

91. D. K. Schroder, Semiconductor Material and Device Characterization, 2nd ed. (John Wiley & Sons, Inc., New York, 1998), pp. 156–157.

92. F. B. Hilderbrand, *Advanced Calculus for Applications* (Prentice-Hall, Englewood, Cliffs, NJ, 1962), p. 574.

93. S. Kristiansson, F. Ingvarson, and K. O. Jeppson, "Compact Spreading Resistance Model for Rectangular Contacts on Uniform and Epitaxial Substrates", *IEEE Trans. on Electron Devices*, **54**, 2531 (2007).

94. A. Nussbaum, "Capacitance and spreading resistance of a stripe line", *Solid-State Electronics*, **38**, 1253-1256 (1995).

95. M. S. Leong, S. C. Choo and L. S. Tan, "The role of source boundary condition in spreading resistance calculations", *Solid-State Electronics*, **21**, 933-941 (1978).

96. R. H. Cox and H. Strack, "Ohmic contacts for GaAs devices", *Solid-State Electronics*, **10**, 1213-1218 (1967).

97. B. Gelmont and M. Shur, "Spreading resistance of a round ohmic contact", *Solid-State Electronics*, **36**, 143-146 (1993).

98. The *r* (or *y*) coordinates of the boundary points C and H is *b* (not shown in Fig. 3.16 and Fig. 3.17). We assume that *b* >> *a* or *b* >> *h*, in which case all formulas in Section 3.4 are valid. See Sections 3.2 and 3.3 for detailed explanation. In all MAXWELL 2D simulations shown in Figs. 3.18 and 3.20, we fixed *b* = 8.8 cm.

99. J. D. Lavers and R. Timsit, "Constriction resistance at high signal frequencies", *IEEE Trans. Compon. Packag. Technol.*, **25**, 446 (2002).

100. H. H. Berger, "Models for contacts to planar devices", *Solid-State Electronics*, **15**, 145 (1972).

101. A. A. Neuber, L. Laurent, Y. Y. Lau, and H. Krompholz, in *High-Power Microwave Sources and Technologies*, Eds.: R. J. Barker and E. Schamiloglu, (IEEE Press, New York, 2001), Ch. 10, p.325.

102. J. Knobloch, R.L. Geng, M. Liepe, and H. Padamsee, "High-fieldQ slope in superconducting cavities due to magnetic field enhancement at grain boundaries", SRF 1999, (Santa Fe, NM, 1999).

103. H. Bosman, W. Tang, Y. Y. Lau and R. M. Gilgenbach, "Heating of a particulate by radio-frequency electric and magnetic fields", *Appl. Phys. Lett.* **85**, 3319 (2004).

104. W. Tang, H. Bosman, Y. Y. Lau and R. M. Gilgenbach, "The Ohmic heating of particulates in a lossless medium", *J. Appl. Phys.* 97, 114915 (2005).

105. S. Ramo, J. R. Whinnery, and T. Van Duzer, *fields and waves in communications electronics* (Wiley, New York, 1994), p. 508.

106. G. L. Carr, S. Perkowitz, and D. B. Tanner, in *Infrared and MM Waves*, edited by K. J. Button (Academic, New York, 1985), Vol. 13, p. 171.

107. R. E. Collin, *Field Theory of Guided Waves* (2nd Edition, IEEE Press, New York, 1990).

108. L. D. Landau and E. M. Lifshitz, *Electrodynamics of Continuous Media*, (Pergamon Press, New York, 1984), p. 322.

109. J. Cheng, R. Roy, and D. Agrawal, "Experimental proof of major role of magnetic field losses in microwave heating of metal and metallic composites", *J. Mater. Sci. Lett.* **20**, 1561 (2001).

110. J. H. Jeans, *the mathematical theory of electricity and magnetism* (4th Edition, Cambridge University Press, Cambridge, 1920), p. 194.

111. R. G. Forbes, C. J. Edgcombe, and U. Valdre', "Some comments on models for field enhancement", *Ultramicroscopy* **95**, 57 (2003).

112. A. C. Rose-Innes and E. H. Rhoderick, *Introduction to Superconductivity* (Pergamon Press, Glasgow, Scotland, 1969), p. 68.

113. E. T. Whittaker and C. N. Watson, *A Course of Modern Analysis*, p. 282, and p. 385, (4th Edition, Cambridge U. Press, 1927).